# Governing Thermodynamic Structure of Tropical East Pacific and African Easterly Waves and their Representation in CMIP6 Models

By

Rosa M. Vargas Martes

A dissertation submitted in partial fulfillment of
the requirements for the degree of

Doctor of Philosophy
(Atmospheric and Oceanic Sciences)

at the
UNIVERSITY OF WISCONSIN-MADISON
2024

Date of final oral examination: 11/25/2024

The dissertation is approved by the following members of the Final Oral Committee:

Ángel F. Adames Corraliza, Associate Professor, Atmospheric and Oceanic Sciences (AOS)
Larissa E. Back, Professor, AOS
Stephanie Henderson, Assistant Professor, AOS
Angela Rowe, Assistant Professor, AOS
Alex O. Gonzalez, Assistant Scientist, Woods Hole Oceanographic Institution

# Dissertation Declaration and Approval

I, Rosa M. Vargas Martes, declare that this Dissertation titled '**Governing Thermodynamic Structure of Tropical East Pacific and African Easterly Waves and their Representation in CMIP6 Models**' and the work presented in it are my own.

| | | |
|---|---|---|
| Rosa M. Vargas Martes | | |
| Author | Signature | Date |

I hereby approve and recommend for acceptance this work in partial fulfillment of the requirements for the degree of Doctor of Philosophy:

| | | |
|---|---|---|
| Ángel F. Adames Corraliza | | |
| Committee Chair | Signature | Date |
| Larissa E. Back | | |
| Faculty Member | Signature | Date |
| Stephanie Henderson | | |
| Faculty Member | Signature | Date |
| Angela Rowe | | |
| Faculty Member | Signature | Date |
| Alex O. Gonzalez | | |
| External Member | Signature | Date |

# Abstract

**Governing Thermodynamic Structure of Tropical East Pacific and African Easterly Waves and their Representation in CMIP6 Models**

by Rosa M. Vargas Martes

Easterly Waves (EWs) are convectively coupled systems of alternating high and low pressure that propagate westward in the Tropics with a period of 3-6 days and horizontal scale of $\sim$ 3000 km. They are most commonly observed in the western hemisphere over the east Pacific Ocean (PEWs) and Africa and the east Atlantic Ocean (AEWs). While significant progress has been achieved in understanding PEWs and AEWs, a thorough comparison between the waves as well as their representation in global climate models (GCMs) remains elusive. The thermodynamic processes associated with convection in AEWs, and PEWs are examined on the basis of empirical orthogonal functions (EOFs) and a plume buoyancy framework. Plume buoyancy is found to be highly correlated with rainfall in both AEWs and PEWs. Close inspection of the contribution of moisture and temperature to plume buoyancy reveals that temperature and moisture contribute roughly equally to the buoyancy in AEWs, while moisture dominates the distribution of buoyancy in PEWs. The results of this study indicate that PEWs are moisture modes: waves in which water vapor plays a dominant role in their thermodynamics. AEWs, on the other hand, are mixed waves in which temperature and moisture play similar roles in their thermodynamics. The representation of these governing thermodynamic structures is further examined in historical Coupled Model Intercomparison Project phase

6 (CMIP6) models. Simulations are compared to data from the Fifth Reanalysis from the European Centre for Medium-Range Weather Forecasts (ERA5). Two representation skill metrics are employed to select models with accurate PEW and AEW representation, the (1) wave relative amplitude and (2) spatial coherence obtained from the pattern correlations of lag-regressed anomalous precipitation between ERA5 and CMIP6 models. A large spread in PEW and AEW representations is observed. Results suggest that the spread in representation skill may be tied to the misrepresentation of convection sensitivity to column moisture, the horizontal distribution of mean column moisture, and precipitation. Furthermore, examination of model diagnostics reveal that both waves grow from moisture-vortex instability, even in the presence of strong meridional temperature gradients. These results underscore the relevance of the accurate representation of moist processes for the accurate representation of PEWs and AEWs in CMIP6 Models.

*"I was the first woman to ever get a Ph.D. in meteorology. Now, over half of the graduate students in the field are women and this makes me very very happy."*

Joanne Simpson

*This work is dedicated to my parents Rosa L. Martes Cordero, and Saúl E. Vargas Rivera, for their unwavering conviction to learning and service through education during my formation years and thereafter. I also thank them for their love and never ending support throughout the completion of this doctoral program. This work is also dedicated to my loving sister Rocío M. Vargas Martes, whose healing conversations and support have been crucial during this process. To my late friend, Ángel Sanchez Bibilony whose memory has helped me endure difficult educational and life periods. To my extended family for all their love and support. Moreover, this work is especially dedicated to my loving husband Derick E. González Acevedo, for his undying love for science and myself, and for being my rock and fuel during this process.*

# Acknowledgements

First and foremost, I thank my advisor Ángel F. Adames Corraliza, for his excellence in research, teaching, and mentoring. Becoming his student has been one of the best decisions I have made in my life, and your example has shaped the type of professional I wish to become. Thank you for the long conversations and advice both in research and in life. Thank you for creating a safe and welcoming environment that made me look forward to my future as a scientist. Thank you for your unwavering commitment to diversity, equity, inclusion, and justice (DEIJ), especially your dedication for creating and supporting students from Puerto Rico. I cannot thank you enough for your help and encouragement through this whole process.

I also thank my second advisor, friend, and brother, Víctor C. Mayta, for his advise, mentoring and support during my time in the program. Thank you for answering my numerous research questions and for providing a safe environment that allowed me to make them in the first place. The numerous visits to your office allowed me to nurture a curious scientific mindset that I will cherish as I continue to pursue a career in science. In addition to this, thank you for being there through every step of this journey, your friendship is one of the best things I will take away from this experience.

I thank my third advisor, friend and desk neighbor, Qiao-Jun. Thank you for all the help, especially with downloading data and letting me run ideas by you. You are so smart and such a role model. Thank you for all the advise and support especially over the past year as I stumbled working with the CMIP6 models!

I thank my doctoral committee, Dr. Larissa E. Back, Dr. Stephanie Henderson, Dr. Angela Rowe, and Dr. Alex O. Gonzalez, your advice and suggestions have been invaluable to the final form on this dissertation. Thank you for your understanding and kind words as I underwent difficult health periods. Moreover, thank you for being great scientific

and life role models. I cannot believe how lucky I am to work with, and learn from every one of you.

I thank Dr. Mayra Oyola-Merced, for being an inspiration and great help throughout my journey in the Ph.D. program. Thank you for being one of my greatest life mentors. For being a great instructor during my first time as a TA! You made me fall in love with radiative transfer (which is no small feat!). Thank you for always providing a caring ear, for your understanding, and wise words in research, work and life. Thank you for your unwavering commitment to DEIJ efforts, especially those pertaining our Puerto Rican community.

I thank Dr. Hannah Zanowski for trusting me as a project assistant for the National Science Foundation (NSF) Student Training in Oceanography Remote Sensing and Meteorology (STORM) program. It had always been my dream to work in and be involved with the planning and execution of a research experience for undergraduates (REU) program. Thank you for giving me this opportunity to work with you during two summers. Thank you for your unwavering commitment with DEIJ. Thank you for the conversations, help, and advice. You are one of my biggest role models.

To Pete Pokrandt, thank you, thank you, thank you! You really are the key to success for every graduate student. Thank you with all the help with the computer, servers, seminar, printers, and much more. Thank you for speaking Spanish with me and for all your patience.

To the administrative staff, Christi, Carolyn, Dee, Scott, Sabrina, and Kaitlyn, thank you for keeping the department running. Thank you for all the help with courses, program requirements, expense reports, travel, payroll, and much more. Thank you for making my summer as a project assistant very enjoyable and for your patience during the process. To all my professors both at the University of Michigan-Ann Arbor (UM) and the University of Wisconsin-Madison (UW), you allowed me to learn so much. Thank you for all the

effort and dedication you put into the preparation of your classes. Thank you for providing me with essential knowledge that aided in my understanding of complex research topics.

I thank the the UW departmental community, for creating a safe and welcoming environment that allowed me to succeed academically. Both classes, seminars, and colloquiums felt like safe spaces which allowed me to truly learn and engage. Thank you for your ongoing commitment to DEIJ efforts and for fostering a diverse community. I feel honored to have been a graduate student in the department.

I thank all the members that have come through the Large Scale Tropical Dynamics family, including Chelsea, Haochang, Kayleen, Becca, Sofia, Adrianna, Yi-Bin, Qiao-Jun, Víctor, Qin-Lu, Ian, Juan, Idamis, Sabrina, Luke, Nelly, Brandon, Sam, and Brittany (phew!). For fostering a community that made my years in the graduate program more productive and successful. You made our office a second home that I always looked forward to return to. Thank you for all the help and feedback with reseach. Thank you for all the conversations, the laughter, and yes, the tears, that we shared. You truly made me feel like I wasn't so alone and made me feel capable, and intelligent. I cannot thank you all enough!

To my friends at the UW outside of my research group, Karimar, Vijit, Steph, Marissa, Maggie, and Doreen, and at the UM Anthony, Alan, Jamie, Samar, Sam, Garret, Zach, Colten, Chloe, and Madison. Thank you for the conversations, shared hobbies, and for making the AOS hallways an enjoyable place to be!

To my graduate school roommates, Chelsea, Kayleen, Karimar, and Víctor, there are no words that can express the gratitude I feel for having been your roommate. You became my second family, brothers and sisters I will always cherish. Thank you for sticking with me through difficult periods throughout my Ph.D. journey.

I thank the students that were a part of the two courses I was a teaching assistant for. Working with you brought so much happiness to my semesters as TA. You are all awesome!

I thank my writing partner, Maggie. You know more than anyone the amount of work that it took to get here. I am so beyond grateful, and wish you the best in research and in life.

I thank the NSF Significant Opportunities in Atmospheric Research and Science (SOARS) and Pre-colledge internship program (PRECIP) for believing in me and seeing a potential I didn't even know I possessed. My summer research experiences with the SOARS and PRECIP programs introduced me to tropical meteorology and propelled my love for tropical waves. It also allowed me to explore and fall in love with research early on in my academic journey. Furthermore, it allowed me to do so within an environment that fostered diverse identities in atmospheric sciences. I can't thank you enough!

Finally, I thank my undergraduate family, Derick, Rocío, Tai, Ivan, Marcel, Ramón, Milton, Edwin, and Alexuan, for all the conversations that we have shared after leaving Puerto Rico, they have helped keep me grounded and connected to our Island. I also thank my extended family (Familia Martes Cordero and Vargas Rivera), for believing in me and never letting me give up. I thank the love of my life, mi abuelita María Rivera, thank you for your unwavering and unconditional love. I also thank all my Tios and Tias (they are a lot to mention one by one!) and my cousins, especially Yair, Jemaris, Cheche, Esthela, Jose I., Jose O., Marcos, Melissa Karina, Yomara, Valeria, Jaime, Tania, Mara, Arielito, and many more (they are also a lot!). I thank my in-laws Gilberto R., Antonia (Nelly), Omar, Yamil, Yari, Betsy, Yarieliz, Nani, Kiara, Dominic Arelis and Lily, for always believing in me and loving me as one of your own. As they say "it takes a village", and what a loving and supporting village I have! I still remember a conversation I had with Luis José (Cheché). around my second year in undergrad, I wanted to give up and you said: "Clean those tears and let's keep going, this is your dream and you can't give up. You can handle this and much more". Thank you for not letting me fall Che!

# Contents

**Abstract** **ii**

**Dedication** **v**

**Acknowledgements** **vi**

**Contents** **x**

**List of Figures** **xiii**

**List of Tables** **xviii**

**Abbreviations** **xix**

**1 Introduction** **1**

**2 The role of water vapor and temperature in the thermodynamics of Tropical Northeast Pacific and African easterly waves** **5**

2.1 Introduction . . . . . 7
2.2 Data and Methods . . . . . 10
2.2.1 Data . . . . . 10
2.2.2 Methods . . . . . 10
2.3 Framework used to evaluate AEW and PEW thermodynamics . . . . . 14
2.3.1 Plume buoyancy-based precipitation estimate . . . . . 14
2.3.2 Scale Analysis . . . . . 19
2.3.3 Moisture Mode Criteria . . . . . 20
2.4 Results . . . . . 21
2.4.1 $q$ and $T$ climatology . . . . . 21
2.4.2 Horizontal Structure of PEWs and AEWs . . . . . 23
2.4.3 EW-related precipitation in a buoyancy framework . . . . . 27
2.4.4 Contribution of $q$ and $T$ to PEW and AEW thermodynamics . . . 29
2.4.4.1 $N_{mode}$ . . . . . 29
2.4.4.2 The thermodynamic contributions to rainfall and $N_{mode}$ 32

2.4.4.3 Moisture Mode Criteria . . . . . 33
2.5 Discussion and Conclusions . . . . . 34

**3 East Pacific Easterly Wave Representation in CMIP6 Models 40**
3.1 Introduction . . . . . 43
3.2 Data and Methods . . . . . 47
3.2.1 Data . . . . . 47
3.2.2 Methods . . . . . 47
3.3 CMIP6 Model Assessment . . . . . 49
3.4 Results . . . . . 51
3.4.1 Thermodynamic Mean State . . . . . 51
3.4.2 PEW Horizontal Structure . . . . . 54
3.4.3 Diagnostics of physical mechanisms important for PEWs . . . . . 55
3.5 Summary and Conclusions . . . . . 58

**4 African Easterly Wave Representation in CMIP6 Models 61**
4.1 Introduction . . . . . 63
4.2 Data and Methods . . . . . 65
4.2.1 Data . . . . . 65
4.2.2 Methods . . . . . 66
4.3 CMIP6 Model Assessment . . . . . 67
4.4 Results . . . . . 71
4.4.1 Thermodynamic Mean State . . . . . 71
4.4.2 PEW Horizontal Structure . . . . . 76
4.4.3 Diagnostics of physical mechanisms important for AEWs . . . . . 79
4.4.3.1 D1: $\overline{\tau}_c$ . . . . . 80
4.4.3.2 D2: $\overline{P}_{indx}$ . . . . . 82
4.4.3.3 D3: $\partial_y L_v \overline{q}_{\text{avg}}$, $\partial_y C_p \overline{T}_{\text{avg}}$, and $\partial_y \overline{m}_{\text{avg}}$. . . . . 82
4.4.3.4 D4: MVI Criterion . . . . . 84
4.5 Summary and Conclusions . . . . . 88

**5 Summary and Conclusion 92**
5.1 Chapter 2: The role of water vapor and temperature in the thermodynamics of Tropical Northeast Pacific and African easterly Waves . . . . . 93
5.2 Chapter 3: East Pacific Easterly Wave Representation in CMIP6 models 94
5.3 Chapter 4: African Easterly Wave Representation in CMIP6 models . . . 95
5.4 Future Work . . . . . 97

**A Appendix: q′ and T′ structure and relationship 98**

**B Appendix: Plume buoyancy-based precipitation estimate and TRMM precipitation 102**

**C Appendix: Leading omega structure in PEWs and AEWs 105**

**D Appendix: Supporting Information for "East Pacific Easterly Wave Representation in CMIP6 Models" 107**

**Bibliography 109**

# List of Figures

2.1 Variance explained by the leading EOFs of the OLR for (a) EPAC (150°W-75°W and 10°$S$-30°N) and (b) WAEA (45°W-30°E and 10°$S$-30°N) regions. The whiskers denote the 95% confidence interval of each eigenvalue. . . . 12

2.2 Distribution of ERA5 precipitation ($P$) and buoyancy averaged over the lower free troposphere ($B_L$) over (a) the EPAC (150°W-75°W and 10°$S$-30°N) and (b) WAEA (45°W-30°E and 10°$S$-30°N) regions, for the time period ranging from 1980-2018. The shaded field shows the natural logarithm of the number of data points in each bin. Values of $P$ are binned every mm day$^{-1}$ and values of $B_L$ are binned every 0.005 m s$^{-2}$. The black line shows the exponential fit to the data. . . . . 17

2.3 Horizontal maps of 600-850 hPa average (top) $L_v q_L$ (shading with units of $kJ\ kg^{-1}$), (middle) $C_p T_L$ (shading with units of $kJ\ kg^{-1}$), and (bottom) $m$ (shading with units of $kJ\ kg^{-1}$) averaged for the months of July-August-September (JAS) over (left) the EPAC and (right) WAEA regions. The root mean square (RMS) amplitude of anomalous precipitation ($P'_{rms}$) for PEWs and AEWs is overlaid as solid contours in all the panels. . . . . 24

2.4 Anomalous ERA5 precipitation ($P'$), estimated precipitation ($P'_{est}$), contribution of specific humidity ($q'$) to $P'_{est}$ ($P'_{estQ}$), contribution of temperature ($T'$) to $P'_{est}$ ($P'_{estT}$) (shaded fields), geopotential height ($z'$) (contours), and horizontal winds ($\mathbf{v}'$) (vectors), regressed upon PC1 of (left) PEWs and (right) AEWs. Contour interval is 0.5 m, starting at 1 m. The longest arrows correspond to a wind anomaly of 1.8 m s$^{-1}$. . . . . 26

2.5 Scatterplot of anomalous estimated precipitation ($P'_{est}$) against ERA5 precipitation ($P'$) for (a) PEWs and (b) AEWs. The shaded field shows the base 10-logarithm of the number of data points in each bin. Values are binned every 0.25 × 0.25 mm day$^{-1}$. The one-to-one line is shown in light gray and the slope ($\mu$) and correlation coefficient ($r$) are shown in the top-left of each panel. The black line shows the linear least squares fit regression of the two fields. The relationships are determined over the region of strongest EW activity, 125°W-90°W and 5°N-20°N for PEWs and 27.5°W-10°E and 5°N-20°N for AEWs. . . . . 28

2.6 Time-longitude diagrams of outgoing long-wave radiation (OLR) (shaded) and geopotential height ($z'$) (contoured) lag regressed onto (b and e) PC1 and (c and f) PC2 of (left) PEW and (right) AEW activity. The fields were averaged over the 5°N-20°N latitude belt. The contour interval is 0.35 m, starting at 0.1m. The EPAC and WAEA regions are shown in panels (a) and (d), for reference. The data presented has a horizontal resolution of 2.5°×2.5° and a 12 hr temporal resolution. . . . . 31

2.7 As in Fig. 2.5, but showing (a and d) the column integrated humidity ($\langle q \rangle'$) against the precipitation rate ($P'$), (b and e) as the apparent heating rate ($\langle Q1 \rangle' \simeq \langle Q_R \rangle' + L_v P' + SH'$) against the advection of dry static energy ($\nabla \cdot \langle s\mathbf{v} \rangle'$), and (b and d) latent energy ($\langle L_v q \rangle$') against moist static energy ($\langle m \rangle'$) for PEWs (left column) and AEWs (right column). Values are binned every 0.45 kg m$^{-2}$ × 0.45 mm day$^{-1}$ in (a) and (d), 25 × 25 W m$^{-2}$ in (b) and (e), and every 0.30×10$^6$ × 0.30×10$^6$ J m$^{-2}$ for (c) and (f). The relationships are determined over the region of strongest EW activity, 125°W-90°W and 5°N-20°N for PEWs and 27.5°W-10°E and 5°N-20°N for AEWs. The slope ($\mu$) and the correlation coefficient ($r$) are shown on the top-left corner of each panel. . . . . 35

2.8 Schematic describing the relative magnitude of total estimated precipitation ($P'_{est}$) (black line), along with its components due to moisture ($P'_{estQ}$) (cyan line) and temperature ($P'_{estT}$) (red line) for (a) PEWs and (b) AEWs. Areas of enhanced precipitation are depicted by the convective clouds and rain. The horizontal circulation is shown by the blue arrows. Blue and orange shading has been added to distinguish waves with origin over (a) ocean, and (b) land respectively. The $N_{mode}$ (top right) and phase speed ($c_p$) (bottom right) values are included for comparison. The thermodynamic structure of (a) PEWs and (b) AEWs are representative of off-equatorial moisture modes and mixed systems as presented by Adames (2022). . . . . 38

3.1 Taylor diagram of the relative standard deviation ($\sigma_r$) of the lag-regressed precipitation ($P'$) from reanalysis and model dataset (radial axis) and the Pearson correlation coefficient ($r$) between the reanalysis and model fields (angle axis). $P'$ is obtained from a lag-regression analysis of the anomalous field onto the first principal component (PC1) of the outgoing longwave radiation (OLR$'$). The dark grey lines denote the centered root mean squared difference from the ERA5 reference value (black triangle). The dashed black line indicates the reference $\sigma_r$ value. Models that fall to the left of the dashed black line underestimate the wave amplitude, while models that fall to the right produce stronger waves. The closer the models are to the reference value, the more realistic the simulation. Models from the same modeling center have the same color and are denoted by triangle markers (up, down, right or left). Models with realistic and unrealistically weak PEW representation are denoted with blue and maroon borders respectively. Analysis is carried over the region of strongest PEW activity, 5°–20°N, 125°–90°W. . . . . 53

3.2 Time-longitude diagram of PEW ERA5 (left), good and unrealistically weak model ensemble (center and right respectively) seasonal (JAS) $P'$ (shaded contours) averaged over the 5°− 20°N latitude belt. Solid and dashed contours denote positive and negative $z'_{700hPa}$ contours respectively. The contour interval is 0.35 m starting at 0.5 m. . . . . 54

3.3 East Pacific Ocean maps of $\overline{P}$ (first row) and column integrated (1000-100 hPa) $L_v\langle\overline{q}\rangle$ (second row), averaged over the months of JAS for ERA5 (first column), good model ensemble (second column), unrealistically weak model ensemble (third column), and good minus unrealistically weak ensemble difference (fourth column) shown as the shadded contours. $P'_{\text{rms}}$ is overlaid as solid contours. . . . . 55

3.4 Horizontal maps of seasonal (JAS) PEW $P'$ (first row) and $L_v\langle q\rangle'$ (second row) for ERA5 (first column), good (second column), and unrealistically weak (third column) ensembles. The $z'_{700hPa}$ (solid and dashed contours) and $\mathbf{v}'_{700hPa}$ (arrows) fields are overlaid in each panel. . . . . 56

3.5 Significant relationships in the representation of PEWs. The relationship between (a) $\sigma_r$ and latent energy gradient index ($\triangle_y L_v\langle\overline{q}\rangle\ indx$), (b) $\sigma_r$ and the moist convective adjustment timescale ($\tau'_c$), and (c) $\sigma_r$ and a $P'$ index over the Panama Bight ($P'_{\text{indx}}$) are all significant at the 95% confidence level. 58

4.1 As in Figure 3.1 but for AEWs. Models with realistic, US−SC, and US−WC AEW representation are denoted with green, purple, and blue borders respectively. Analysis is carried over the region of strongest AEW activity, 5°–20°N, 35°W–20°E. . . . . 70

4.2 As in Figure 3.2 but for AEWs in reanalysis (first row), good (second row), US−SC (third row), and US−WC (fourth row). . . . . 71

4.3 East Atlantic Ocean and West Africa maps of $\overline{P}$ (first column), $L_v\overline{q}_{\text{avg}}$ (second column), $C_p\overline{T}_{\text{avg}}$ (third column), and $\overline{m}_{\text{avg}}$ (fourth column), averaged over the months of JAS for ERA5 (first row), and good (second and third rows), US−SC (fourth and fifth rows), and US−WC (sixth and seventh rows) models. $P'_{\text{rms}}$ is overlaid as solid contours in the $\overline{P}$ maps (first column). 74

4.4 Differences between ERA5 and good (first row), US−SC (second row), and US−WC (third row) $\overline{P}$ during JAS. . . . . 75

4.5 As in Figure 2.2, but for the distribution of $P$ and CSF in ERA5 (first row), good (second row), US−SC (third row) and US−WC (fourth row), determined over a region of high AEW activity (25°W-0° and 5°-17.5°N), during boreal summer (JAS) during the period of 1980-2014. $P$ values are binned every 1 mm day$^{-1}$, beginning at 0 mm day$^{-1}$. While CSF values are binned every 0.05 units of CSF, beginning at 0 units of CSF. . . . . 76

4.6 As in Figure 3.4 but for AEWs-related (a-g) $P$, (h-n) $L_v q'_{\text{avg}}$, (o-u) $C_p T'_{\text{avg}}$, and (v-ab) $m'_{\text{avg}}$ in ERA5 (first row), good (second and third rows), US-SC (fourth and fifth rows), and US-WC (sixth and seventh rows) models. Wind vectors are shown beginning at 0.35 m s$^{-1}$, while $z'_{700\text{hPa}}$ values begin at 1 m with increases every 0.35 m. . . . . 78

4.7 As in Figure 3.5 but for AEW relationships between $\sigma_r$ and (a) $\overline{\tau}_c$, and (b) $\overline{P}_{indx}$. Models with good, US−SC, and US−WC AEW representation are denoted with green, purple, and blue borders respectively. Analysis for $\overline{\tau}_c$ is carried over a region of strong AEW activity, 5°–17.5°N, 25°W–0°. $\overline{P}_{indx}$ is determined by subtracting the average values over land (2.5°-12.5°E and 5°-12.5°N) and ocean (30°-20°W and 5°-12.5°N). Both relationships are significant at the 95% confidence level. . . . . 81

4.8 Meridional gradients in (a and d) $L_v\overline{q}_{\text{avg}}$, (b and e) $C_p\overline{T}_{\text{avg}}$, and (c and f) $\overline{m}_{\text{avg}}$ of reanalysis, and model datasets over the ocean (top row), and land (bottom row). Gradients are determined by zonally averaging over the ocean (25°-20°W) and land (2.5°-7.5°E). The latitudes where most models exhibit positive gradients are further highlighted by the gray box. The names of models that reproduce realistic AEWs are shown in bold. Models selected as good, US−SC and US−WC are denoted by asterisks (*), crosses (†), and stars ($\star$) respectively. . . . . 83

4.9 As in Figure 4.7 but for (a and d) $\partial_y L_v\overline{q}_{\text{avg}}$, (b and e) $\partial_y C_p\overline{T}_{\text{avg}}$, and (c and f) $\partial_y\overline{m}_{\text{avg}}$, over ocean (top row), and land (bottom row). Over the ocean, both $\partial_y L_v\overline{q}_{\text{avg}}$ and $\partial_y\overline{m}_{\text{avg}}$ relationships are significant at the 95% confidence level, whereas over land they are significant at the 90% confidence level. . . . . 85

4.10 As in Figure 4.8 but for (a-b) $-f\partial_y Lv\overline{P}$ over the east Pacific Ocean (top row), and west Africa (bottom row). The names of models with realistic PEW representation are shown in bold. Models used in the realistic and unrealistically weak model ensembles in Chapter 3, are marked with asterisks (*) and stars ($\star$) respectively. The $-f\partial_y Lv\overline{P}$ values are determined by zonally averaging over 85°-80°W for the east Pacific, and 5°W-0° for West Africa. . . . . 86

4.11 As in Figure 4.8 but for the relationship between $\sigma_r$ and $-f\partial_y\overline{P}$ over (a) the east Pacific, and (b) west Africa. Models with good, US−SC, and US−WC AEW representation are denoted with green, purple, and blue borders respectively. Models with good, and unrealistically weak PEW representation are denoted by the dashed green, maroon borders respectively. 88

A.1 As in Fig. 2.4, but showing latent energy ($L_v q'_L$) and temperature energy ($C_p T'$) as the shaded fields. . . . . 100

A.2 As in Fig. 2.4, but showing latent energy ($L_v q'_L$) and temperature energy ($C_p T'$) as the shaded fields for PC2. . . . . 101

B.1 Regression maps of anomalous (top) ERA5 precipitation ($P'$), geopotential height ($z'$), and horizontal winds ($\mathbf{v}'$), (middle) estimated precipitation ($P'_{est}$), $z'$, and $\mathbf{v}'$, and (bottom) TRMM/GPM precipitation ($P'_{TRMM}$), $z'$, and $\mathbf{v}'$, for PC1 for (left) PEWs and (right) AEWs. Contour interval is 0.5 m, starting at 1 m. The longest arrows correspond to a wind anomaly of 1.8 m s$^{-1}$ . . . . . 104

C.1 Leading principal component of vertical velocity ($\omega'$) over the EPAC (150°W-75°W and 10°$S$-30°N) (left) and WAEA (45°W-30°E and 10°$S$-30°N) (right). 106

# List of Tables


2.1 The variables used in the study, all drawn from ERA5. . . . . 11

2.2 Constants, values, and units used throughout the study. . . . . 18

2.3 Correlation coefficients (r) and slopes ($\mu$) of the relationship between $P'$, $P'_{est}$, $P_{estQ}$, $P'_{estT}$, and $P'_{estH}$. The relationships are determined over the region of strongest EW activity, 125°W-90°W and 5°N-20°N for PEWs and 27.5°W-10°E and 5°N-20°N for AEWs. . . . . 29

2.4 Phase speed ($c_p$) and $N_{mode}$ values for PEWs and AEWs. . . . . 29

2.5 $P'_{estT} - P'_{estQ}$ ratio calculated from Table 2.3 (Calc) and the right-hand side of Eq (2.23). . . . . 33

3.1 Relative standard deviation ($\sigma_r$) between ERA5 and CMIP6 models $P'$, as well as the correlation coefficient ($r$) of the relationship between both fields. The relationships are determined over the region of strongest PEW activity, 125°W-90°W and 5°N-20°N. Crosses (†) and asterisks (*) denote the models used for the good and unrealistically weak model ensembles respectively. The models with realistic representation of PEWs, are presented in bold for emphasis. . . . . 52

4.1 Relative standard deviation ($\sigma_r$) between ERA5 and CMIP6 models $P'$, as well as the correlation coefficient ($r$) of the relationship between both fields. The relationships are determined over the region of strongest AEW activity, 35°W-20°E and 5°N-20°N. Models chosen for further analysis are identified as good, unrealistically strong-strong correlation, and unrealistically strong-weak correlation and are denoted by crosses (†), asterisks (*), and stars (⋆) respectively. The models with realistic representation of AEWs, are presented in bold for emphasis. . . . . 68

D.1 CMIP6 model name, run, and original resolution used in the study Eyring et al. (2016). . . . . 108

# Abbreviations

| | |
|---|---|
| **EW** | **E**asterly **W**aves |
| **PEW** | **P**acific-**E**asterly **W**ave |
| **AEW** | **A**frican-**E**asterly **W**ave |
| **TRMM** | **T**ropical **R**ainfall **M**easuring **M**ission |
| **EPAC** | **E**ast-**P**acific **O**cean |
| **WAEA** | **W**est-**A**frica and the **E**ast **A**tlantic Ocean |
| **CMIP6** | **C**oupled **M**odel **I**ntercomparison **P**roject, Phase **6** |

# Chapter 1

# Introduction

For a long time, the tropical atmosphere was believed to be quiescent with the exception of occasional hurricanes (Air Weather Service Scott AFB, 1944, Riehl, 1954). It wasn't until periods of global unrest circa the 1940s, that the need to further our understanding of marine tropical meteorology arose, and with it challenged this notion.

This propelled pioneering studies such as those carried by institutions such as the Institute of Tropical Meteorology (cooperative effort between the University of Chicago and the University of Puerto Rico) (e.g., Riehl, 1945, Riehl, 1954), United States (US) Air Weather Service (e.g., Air Weather Service Scott AFB, 1944) and the Army Air force (e.g., Kindle, 1944) and Weather Bureau (e.g., Dunn, 1940). Among the studied phenomenon, "waves in the easterlies" were the first type of convectively coupled tropical waves to be recognized (Air Weather Service Scott AFB, 1944, Dunn, 1940, Kiladis et al., 2009, Kindle, 1944,

Riehl, 1945, 1954). Early studies and observations of easterly waves (EWs) identified them as westward propagating wave-like disturbances within the easterly flow, with a horizontal length-scale of 2,500 - 3,000 km, periods of 3-4 days, and phase speeds of around 8 m $s^{-1}$ (Air Weather Service Scott AFB, 1944, Dunn, 1940, Kiladis et al., 2009, Reed et al., 1977, Reed and Recker, 1971, Riehl, 1945, Thompson et al., 1979). They had inverted trough structures (Riehl, 1945, 1954) and could organize convection and serve as seed disturbances for tropical cyclones (Dunn, 1940, Riehl, 1948).

EW research has come a long way since then. We now know that these disturbances are tropical depression-type systems with westward wavenumbers ($k$) 5-20 and periods from 2.5-10 days (e.g., Feng et al., 2020, Kiladis et al., 2009, Mayta and Adames Corraliza, 2024) that are ubiquitous across the tropical atmosphere (Lau and Lau, 1990, Mayta and Adames Corraliza, 2024). While EWs are convectively coupled, they do not correspond to a normal mode solution of Matsuno's dry shallow water (SW) theory (Matsuno, 1966). Some studies have shown that the evolution of EWs is tied to deep convection (e.g., Janiga and Thorncroft, 2013) and that moist processes are as important as dry dynamics for the growth of EWs (Berry and Thorncroft, 2012, Mayta and Adames, 2023, Mayta and Adames Corraliza, 2024).

Thus, two schools of thoughts have formed with regards to EW research, dry and moist perspectives. For instance, in regards to the dry perspective, Torres and Thorncroft (2022) posed that over the east Pacific Ocean, EW evolution could be tied to potential vorticity gradients over the region. Kiladis et al. (2006) employed a dynamical model to examine

the three-dimensional structure and dynamics of AEWs but found that barotropic and baroclinic instability alone could not explain wave initiation. On the other hand, recent studies have highlighted the relevance of moist processes in governing the thermodynamics of EWs (Berry and Thorncroft, 2012, Huaman et al., 2021, Mayta and Adames, 2023, Mayta and Adames Corraliza, 2024, Núñez Ocasio and Rios-Berrios, 2023, Russell and Aiyyer, 2020, Russell et al., 2020, Wolding et al., 2020). Mayta and Adames Corraliza (2024) found that advection of anomalous moisture by background trade winds aided the propagation of oceanic TD-type waves around the globe. In addition, they found that both the propagation and growth of moist static energy ($m$) anomalies resulted from the advection of the background moisture by the anomalous meridional winds.

Recent advances in moisture mode theory (e.g., Adames, 2022, Adames et al., 2019, Mayta et al., 2022, Neelin and Yu, 1994, Sobel et al., 2001, Yu and Neelin, 1994) have posited that EWs over oceanic regions are moisture modes, waves whose thermodynamics are governed by moisture (Mayta and Adames, 2023, Mayta and Adames Corraliza, 2024, Vargas Martes et al., 2023, Wolding et al., 2020), whereas EWs that evolve over land masses are mixed systems whose thermodynamics are modulated comparably by moisture and temperature (e.g., Núñez Ocasio and Rios-Berrios, 2023, Vargas Martes et al., 2023, Wolding et al., 2020). Over the western hemisphere, tropical northeast Pacific and African EWs (PEWs and AEWs respectively), serve as seeds for TC development (e.g., Avila and Guiney, 2000, Avila et al., 2003, Landsea et al., 1998, Pasch et al., 2009, Thorncroft and Hodges, 2001), are important sources of precipitation variability (e.g., Dominguez et al.,

2020, Fahrin et al., 2024, Kiladis et al., 2009), and contribute non-negligibly to the tropical general circulation (e.g., Mayta and Adames Corraliza, 2024).

While PEWs and AEWs occur over the same hemisphere, they exhibit distinct characteristics (Vargas Martes et al., 2023, Wolding et al., 2020). For instance, PEWs have been found to exhibit smaller horizontal thermodynamic and dynamic structures. In addition, previous results indicate that their thermodynamics are governed by moisture. Whereas, the thermodynamic evolution in AEWs has been found to be governed by moisture and temperature comparably. With recent efforts evidencing these differences, a study assessing global climate model (GCM) skill at reproducing these transients remains elusive. Said tasks are the main objective of this doctoral dissertation.

The study is structured as follows. Chapter 2 examines the governing thermodynamic structure of PEWs and AEWs on the basis of a novel plume buoyancy framework (Adames et al., 2021, Ahmed and Neelin, 2018, Ahmed et al., 2021), empirical orthogonal function (EOF) analysis, and moisture mode theory. Chapter 3 assesses the representation of PEWs in Coupled Model Intercomparison Project, Phase 6 (CMIP6) (Eyring et al., 2016). Similarly, chapter 4 examines the representation of AEWs in CMIP6 models. Finally, a summary and concluding remarks are presented in Chapter 5.

# Chapter 2

# The role of water vapor and temperature in the thermodynamics of Tropical Northeast Pacific and African easterly waves

Vargas Martes, R.M., Á. F. Adames Corraliza, and V. C. Mayta, 2023: The role of water vapor and temperature in the thermodynamics of Tropical Northeast Pacific and African easterly waves. *J. Atmos. Sci.*, 2305 - 2322, doi: https://doi.org/10.1175/JAS-D-22-0177.1.

© American Meteorological Society. Used with permission.

# Abstract

The thermodynamic processes associated with convection in Tropical African and Northeastern Pacific Easterly Waves (AEWs and PEWs, respectively) are examined on the basis of Empirical Orthogonal Functions (EOFs) and a plume-buoyancy framework. Linear regression analysis reveals the relationship between temperature, moisture, buoyancy, and precipitation in EWs. Plume buoyancy is found to be highly correlated with rainfall in both AEWs and PEWs, and a near 1:1 relationship is found between a buoyancy-based diagnostic of rainfall and rainfall rates from ERA5. Close inspection of the contribution of moisture and temperature to plume buoyancy reveals that temperature and moisture contribute roughly equally to the buoyancy in AEWs, while moisture dominates the distribution of buoyancy in PEWs. A scale analysis is performed in order to understand the relative amplitudes of temperature and moisture in easterly waves. It is found that the smaller contribution of temperature to the thermodynamics of PEWs relative to AEWs is related to their slower propagation speed, which allows PEWs to more robustly adjust to weak temperature gradient (WTG) balance. The consistency of the buoyancy analysis and the scale analysis indicates that PEWs are moisture modes: waves in which water vapor plays a dominant role in their thermodynamics. AEWs, on the other hand, are mixed waves in which temperature and moisture play similar roles in their thermodynamics.

## 2.1 Introduction

Easterly waves (EWs) are ubiquitous systems in the tropical atmosphere. They are westward-propagating regions of alternating high and low pressure with a horizontal scale of $\sim 3000$ km and a time scale of $\sim 3-6$ days (Lau and Lau, 1990). They can be observed in several regions of the northern tropics including the Pacific and Atlantic oceans (Lau and Lau, 1990, 1992). EWs are often coupled to convection and their associated precipitation plays an important role in the hydrological cycle of the Tropical Northeast Pacific Ocean, the islands of the Caribbean Sea (Dominguez et al., 2020), and sub-Saharan Africa (Kiladis et al., 2009).

Many studies have shown that deep convection in the tropics is sensitive to the concentration of water vapor in the free troposphere (Bretherton et al., 2004, Chaboureau et al., 2004, Holloway and Neelin, 2009, Jensen and Genio, 2006, Myoung and Nielsen-Gammon, 2010, Raymond, 2000, Redelsperger et al., 2002, Sherwood, 1999, Sherwood et al., 2004, Waite and Khouider, 2010). This coupling is likely due to the dilution updrafts experience as they entrain dry environmental air, which reduces their buoyancy (Ahmed and Neelin, 2018, Hannah, 2017, Kuo et al., 2017, Lucas et al., 1994). Temperature also plays a role in the occurrence and organization of deep convection. It is well known that temperature fluctuations in the free troposphere can increase or suppress the convective available potential energy (CAPE) and convective inhibition (CIN), both of which are essential factors in the occurrence of deep convection (Kuang, 2008, Mapes, 2000, Raymond et al., 2006).

While EWs can be identified over different regions (Lau and Lau, 1990, 1992), Tropical Northeast Pacific and African Easterly Waves (PEWs and AEWs respectively) propagate across the western hemisphere yet exhibit distinct characteristics. Several studies, have shown that deep convection plays a central role in the evolution of AEWs (Cheng et al., 2019, Fink and Reiner, 2003, Janiga and Thorncroft, 2013, Russell and Aiyyer, 2020, Russell et al., 2020). Berry and Thorncroft (2012), for example, showed that moist convection is as important as dry dynamics for the growth of EWs in the African-Atlantic region. On the other hand, moist convection has been found to be equally, if not more important to the evolution of PEWs (Lau and Lau, 1992, Mayta and Adames, 2023, Rydbeck and Maloney, 2015, Serra et al., 2008, 2010, Wolding et al., 2020). Rydbeck and Maloney (2015) found that the convective coupling of PEWs can be explained in terms of large-scale moisture fluctuations.

In addition to the effects on convection, temperature and humidity fluctuations also modulate the propagation of convectively coupled waves in the tropics (Adames, 2022, Adames et al., 2019, Adames and Maloney, 2021, Mayta and Adames, 2023, Mayta et al., 2022, Wolding et al., 2020). For instance, waves whose dynamics are predominantly driven by moisture fluctuations will exhibit slower propagation, and are commonly referred to as moisture modes (Adames, 2022, Adames and Maloney, 2021, Mayta and Adames, 2023, Neelin and Yu, 1994, Raymond and Fuchs, 2009, Yu and Neelin, 1994). On the other hand, waves whose dynamics are driven by temperature fluctuations exhibit fast propagation speeds as in convectively-coupled gravity waves, and mixed Rossby-gravity waves (Adames, 2022, Adames et al., 2019, Adames and Maloney, 2021, Mayta and Adames,

2023). Finally, waves who exhibit shared characteristics of moisture modes and gravity waves have been identified as mixed systems. Transients within these wave groups exhibit distinct propagation speeds and unique thermodynamic structures. Understanding within which group EWs fall can aid in discerning which fields hold the highest relevance in their thermodynamic evolution.

In this study, we will examine the role that temperature and moisture may have in the convective coupling and thermodynamics of AEWs and PEWs. To understand the convective coupling we will make use of the plume buoyancy framework developed by Ahmed and Neelin (2018) and expanded upon by Ahmed et al. (2020) and Adames et al. (2021). We will also implement the scale analysis framework of Adames et al. (2019) and Adames (2022) to understand the relative importance of temperature and moisture in the thermodynamic evolution of these waves. Our results show that moisture governs the convective coupling and thermodynamic evolution of PEWs, while temperature and moisture play a comparable role in AEWs. Thus, our results suggest that, in spite of sharing a similar name, AEWs and PEWs are governed by distinct thermodynamic processes and may couple to convection differently.

This study is structured as follows. Section 2.2 discusses the data and statistical techniques implemented. Section 2.3 outlines the plume buoyancy-based precipitation estimate, the scale analysis, and moisture mode criteria used to evaluate PEWs and AEWs. Section 2.4 presents the results of the study. Finally, the discussion and concluding remarks are presented in Section 2.5.

## 2.2 Data and Methods

### 2.2.1 Data

The data employed in the study is from the European Centre for Medium-range Weather Forecasting's (ECMWF) Fifth Reanalysis (ERA 5) (Hersbach et al., 2020). The data used is twice daily at 00 and 12 UTC from 1980-2018. We study the waves that occur from July to September (JAS) season when tropical cyclone activity is the highest over the Tropical Atlantic and Northeast Pacific oceans. Precipitation and OLR data used in this study are also taken from ERA5. We make use of surface and pressure level data from 1000-100 hPa. The domains of interest are the regions of the Tropical Northeast Pacific Ocean (EPAC) (150°W-75°W and 10°S–30N°) and West Africa and the Northeast Atlantic Ocean (WAEA) (45°W-30°E and 10°S–30°N). The domains are chosen to be of the same size to facilitate the comparison of the waves. The main fields and their definitions are shown in Table 2.1. The variables averaged over the planetary boundary layer (PBL) (1000 hPa−950 hPa), and the lower free troposphere (LFT) (950 hPa−600 hPa) are denoted by the subscripts $B$ and $L$, respectively. Angle brackets ($\langle\cdot\rangle$) denote a mass-weighted vertical integral from 1000 to 100 hPa.

### 2.2.2 Methods

Anomalies in the aforementioned fields are obtained by subtracting their annual means. A 2-6 day Lanczos filter (Duchon, 1979) is then applied to retain variability at the timescale of PEWs and AEWs.

Table 2.1: The variables used in the study, all drawn from ERA5.

| *Var.* | *Description* | *Units* |
|---|---|---|
| OLR | Outgoing Longwave Radiation | $\mathrm{Wm}^{-2}$ |
| $\Phi$ | Geopotential | m |
| $z$ | Geopotential Height | m |
| $\mathbf{v}$ | Horizontal vector wind | $\mathrm{m\ s}^{-1}$ |
| $\omega$ | Vertical Velocity | $\mathrm{Pa\ s}^{-1}$ |
| $B$ | Plume Buoyancy | $\mathrm{m\ s}^{-2}$ |
| $q$ | Specific Humidity | $\mathrm{kg\ kg}^{-1}$ |
| $q^*$ | Saturation Specific Humidity | $\mathrm{kg\ kg}^{-1}$ |
| $T$ | Temperature | K |
| $m$ | Moist Static Energy | $\mathrm{J\ kg}^{-1}$ |
| $h$ | Moist Enthalpy | $\mathrm{J\ kg}^{-1}$ |
| $h^*$ | Saturation Moist Enthalpy | $\mathrm{J\ kg}^{-1}$ |
| $P$ | Surface Precipitation Rate | $\mathrm{mm\ s}^{-1}$ |
| $P_{est}$ | Precipitation estimated from $B$ | $\mathrm{mm\ s}^{-1}$ |

To capture the predominant wave patterns of the filtered data set, an EOF analysis is applied to the OLR field over the EPAC and WAEA. While analysis was performed over the broader EPAC and WAEA domains, the results are consistent if the EOF is employed over a smaller domain where wave activity is the strongest (125°W-90°W and 5°N-20°N for PEWs and 27.5°W-10°E and 5°N-20°N for AEWs). The resulting eigenvalue spectrum is shown in Fig. 2.1.a,b, for the EPAC and WAEA respectively. The two leading EOFs are well separated from the rest in both regions and are statistically-significant according to the North et al. (1982) criterion. The fraction of the total variance explained by the leading EOFs over WAEA are 5.2% and 4.9% for EOF1 and 2 respectively. Over the EPAC the two leading EOFs explain 3.2% and 3.1% of the OLR variance.

Many of the results of this study are based on linear regression of the leading principle components (PCs) of OLR onto the fields of interest. These regressions are obtained

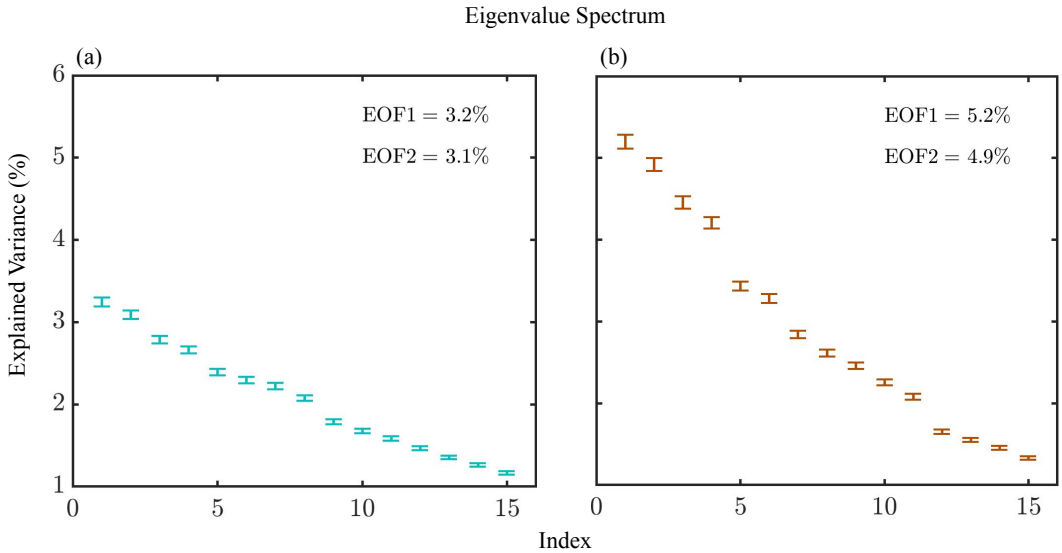


FIGURE 2.1: Variance explained by the leading EOFs of the OLR for (a) EPAC (150°W-75°W and 10°$S$-30°N) and (b) WAEA (45°W-30°E and 10°$S$-30°N) regions. The whiskers denote the 95% confidence interval of each eigenvalue.

following Eq. (1) of Adames and Wallace (2014):

$$\mathbf{D} = \mathbf{S}\hat{\mathbf{P}}^T/N, \tag{2.1}$$

where $\mathbf{D}$ is the regression, $\mathbf{S}$ is the field variable, $\hat{\mathbf{P}}$ is the PC time series, and $N$ is the length of the PC. The statistical significance of the data was determined by a two-sided t-test as in previous studies of EWs (e.g., Kiladis et al. 2006). The effective degrees of freedom in the filtered data ($N^*$) is obtained following Chen (1982):

$$N^* = \frac{N\Delta t}{\tau^*} \tag{2.2}$$

where $N$ is the sample size, $\Delta t$ is the time step, and $\tau^*$ is the decorrelation timescale:

$$\tau^* = \sum_{i=1}^{k} C_{xx}(i\Delta t) C_{yy}(i\Delta t)\Delta t \tag{2.3}$$

where $C_{xx}$ and $C_{yy}$ are the discrete autocorrelation coefficients of the PC time series ($\hat{\mathbf{P}}$) and the field of interest ($\mathbf{S}$). The contour intervals in many of the figures shown below are chosen such that they are statistically significant at the 95% confidence interval.

Time longitude diagrams of OLR and $\Phi$ are also used in this study. These are constructed via a lag regression analysis as in Adames and Kim (2016). Lag regression maps are obtained from lag day -6 to lag day 6, which are then meridionally averaged from 5°N-20°N. From these diagrams we can calculate the zonal component of the phase speed ($c_p$) of PEWs and AEWs by applying a Radon Transform (Radon, 1917) to the OLR field. To determine the two-dimensional Radon Transform from a time-longitude diagram in the ($x$, $y$) space, an arbitrary plane ($x'$, $y'$) is allowed to rotate anti-clockwise in a way that allows $x'$ to be oriented at an angle $\theta$ (ranging from 0°-180°) with respect to the $x$ axis (Mayta and Adames, 2021, Mayta et al., 2021). The wave signal in the time-longitude diagram is then projected onto an arbitrary line ($L$) along $x'$. The variance of the wave signal is then calculated along this line $L$. The angle $\theta_{max}$ in which the rotation leads to the maximum signal variance along $L$ is then used to calculate the phase speed, which can be obtained following Eq. (A3) in Mayta et al. (2021):

$$c_p = \frac{\Delta x}{\Delta t} \tan(\theta_{max}), \tag{2.4}$$

where $\Delta x$ is the zonal distance of each grid point.

## 2.3 Framework used to evaluate AEW and PEW thermodynamics

### 2.3.1 Plume buoyancy-based precipitation estimate

In this study, we make use of the plume buoyancy framework developed by Ahmed and Neelin (2018) and extended upon by Ahmed et al. (2020) and Adames et al. (2021) to diagnose PEW and AEW-related rainfall. The main variables are shown in Table 2.1. Constants and their values are shown in Table 3.1. We will use the definition of plume buoyancy described by Adames et al. (2021), which is written as:

$$B = g\frac{\theta_{eu} - \overline{\theta_e^*}}{\kappa\overline{\theta_e^*}} \tag{2.5}$$

where $\theta_{eu}$ is the equivalent potential temperature of a rising plume, $\overline{\theta_e^*}$ is the saturation equivalent potential temperature of the environment, $g$ is the gravitational acceleration, and $\kappa$ is defined as:

$$\kappa = 1 + \frac{L_v^2 q^*}{C_p R_v T^2}, \tag{2.6}$$

where $L_v$ is the latent heat of vaporization, $q^*$ is the saturation specific humidity, $C_p$ is the specific heat of dry air at constant pressure, $R_v$ is the gas constant of water vapor, and $T$ is the temperature.

Ahmed et al. (2020) showed that precipitation increases quasi-linearly once the LFT averaged value of $B$ ($B_L$) exceeds a critical value. They parameterized this pickup curve in their model using a ramp function. While this representation may describe the sudden onset of tropical deep convection more accurately, it is not amenable to the linear analysis we want to perform here. Instead, we will represent $P$ as an exponential function of $B_L$:

$$P_{est} = P_0 \exp(a_L B_L) \tag{2.7}$$

where $a_L$ is an empirically-determined constant that describes the steepness of the pickup curve. A value of $\approx$ 75 mm day$^{-1}$ s$^2$ m$^{-1}$ was obtained from least-squares fit of the $P - B_L$ relation for the PEW and AEW regions, as shown in Fig. 2.2. This relationship is similar to the one Bretherton et al. (2004) found for $P$ and column saturation fraction, but replacing the latter with $B_L$. While Ahmed et al. (2020), use TRMM precipitation and ERA5 $B_L$ to examine this relationship, we choose to incorporate both ERA5 fields, due to the limited temporal availability of the TRMM satellite observations (1998-2014). Nonetheless, Wolding et al. (2022) compare the convective life cycles of TRMM and ERA5 precipitation on the basis of the plume buoyancy framework, and find that these have similar characteristics. Furthermore, the first mode of the linear regression analysis for both ERA5 and TRMM precipitation presented in Fig. B.1, shows that the horizontal structure of these fields over the studied regions is consistent. Thus, we posit that results would be consistent whether reanalysis or satellite observations are used in the study.

Following Adames (2017), we linearize Eq. (2.7) with respect to a climatological-mean precipitation $\overline{P}$, yielding the following expression for the precipitation anomalies:

$$P'_{est} = \overline{P} a_L B'_L, \tag{2.8}$$

where primed variables are anomalies with respect to the JAS climatology. Following Ahmed et al. (2020) we can also linearize $B_L$, so that we can write $P'_{est}$ as:

$$P'_{est} = \left( \frac{h'_B}{\tau_h} + \frac{L_v q'_L}{\tau_q} + \frac{C_p T'_L}{\tau_t} \right) \frac{\Delta p}{g L_v}, \tag{2.9}$$

where $h'_B$ is the moist enthalpy anomaly of the PBL and $\Delta p$ is the thickness of the troposphere. Eqs. (2.8) and (2.9) explain the relative consumption of buoyancy by convection (Ahmed et al., 2020). This estimated quantity is useful as we can examine the separate contributions from the LFT and PBL. Thus from eq. (2.9) we see that $B'_L$ is sensitive to the $h_B$, dryness of the LFT, and the stratification of $T'$ (Ahmed et al., 2020). The $\tau_q$, $\tau_t$ and $\tau_h$ terms represent these sensitivities to perturbations in $q_L$, $T_L$, and $h_B$ respectively, and are defined by:

$$\tau_h = \frac{\overline{\kappa}_L \Delta p}{a_L g L_v \overline{P}} \left( \frac{g \Pi_L w_B}{\Pi_B \overline{h^*_L}} \right)^{-1}, \tag{2.10}$$

$$\tau_q = \frac{\overline{\kappa}_L \Delta p}{a_L g L_v \overline{P}} \left( \frac{g w_L}{\overline{h^*_L}} \right)^{-1}, \tag{2.11}$$

$$\tau_t = \frac{\overline{\kappa}_L \Delta p}{a_L g L_v \overline{P}} \left( \frac{g \Pi_L}{\overline{h^*_L}} \left[ \left( \frac{w_B \overline{h^*_B}}{\Pi_B \overline{h^*_L}} + \frac{w_L \overline{h_L}}{\Pi_L \overline{h^*_L}} \right) \overline{\kappa_L} - \frac{w_L}{\Pi_L} \right] \right)^{-1}, \tag{2.12}$$

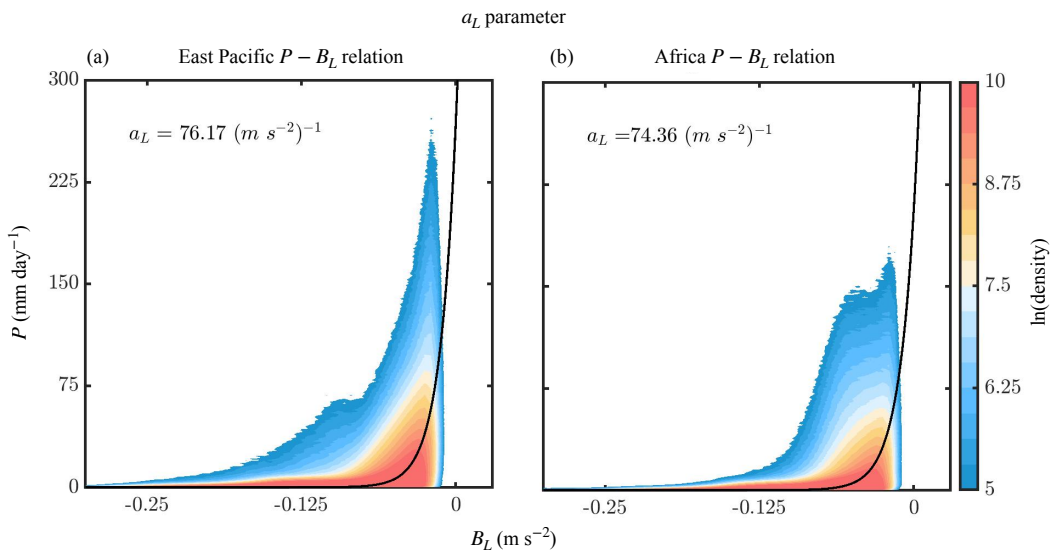


FIGURE 2.2: Distribution of ERA5 precipitation ($P$) and buoyancy averaged over the lower free troposphere ($B_L$) over (a) the EPAC (150°W-75°W and 10°$S$-30°N) and (b) WAEA (45°W-30°E and 10°$S$-30°N) regions, for the time period ranging from 1980-2018. The shaded field shows the natural logarithm of the number of data points in each bin. Values of $P$ are binned every mm day$^{-1}$ and values of $B_L$ are binned every 0.005 m s$^{-2}$. The black line shows the exponential fit to the data.

where $h^*$ is the saturation moist enthalpy, $\Pi = (p/p_0)^{R_d/C_p}$ is the Exner function, where $p_0 = 1000$ hPa, and

$$w_B = \frac{\Delta p_B}{\Delta p_L} ln\left(1 + \frac{\Delta p_L}{\Delta p_B}\right) \tag{2.13}$$

$$w_L = 1 - w_B \tag{2.14}$$

are weights that describe the relative contribution of the PBL and LFT to $B'_L$. These sensitivities ($\tau_h$, $\tau_q$, and $\tau_t$) impact the convective response in different ways, while $P'$ acts to remove cold $T'_L$, $q'_L$ impacts $P'$ by altering the subsaturation of the environment (Ahmed et al., 2020). While $P'$ in the PBL is not sensitive to variations in $q'$ and $T'$, $h'_B$ impacts $P'$ by changing the stability of the plume (Ahmed et al., 2020).

TABLE 2.2: Constants, values, and units used throughout the study.

| *Quantity* | *Description* | *Value* | *Units* |
|---|---|---|---|
| PBL | planetary boundary layer | $1000 - 950$ | hPa |
| LFT | lower free troposphere | $950 - 600$ | hPa |
| $\Delta p$ | thickness of the troposphere | 900 | hPa |
| $\Delta p_B$ | thickness of the PBL | 50 | hPa |
| $\Delta p_L$ | thickness of the LFT | 350 | hPa |
| $g$ | gravitational acceleration | 9.806 | $m$ s$^{-2}$ |
| $C_p$ | specific heat of dry air at constant pressure | 1004 | J kg$^{-1}$ K$^{-1}$ |
| $R_v$ | gas constant of water vapor | 461 | J kg$^{-1}$ K$^{-1}$ |
| $L_v$ | latent heat of vaporization | $2.5 \times 10^6$ | J kg$^{-1}$ |
| $w_B$ | weighted contribution to $B_L$ from the PBL | 0.2971 | – |
| $w_L$ | weighted contribution to $B_L$ from the LFT | 0.7029 | – |
| $\Pi_B$ | PBL Exner function | 0.99 | – |
| $\Pi_L$ | LFT Exner function | 0.93 | – |
| $a_L$ | exponential fit to the $P - B_L$ distribution | 75 | s$^2$ m$^{-1}$ |

Eq. (2.9) allows us to estimate the contributions of $q'_L$, $T'_L$ and $h'_B$ to $P'_{est}$. These individual components are defined as:

$$P'_{estT} = \frac{\Delta p}{gL_v}\frac{C_p T'_L}{\tau_t}, \tag{2.15}$$

$$P'_{estQ} = \frac{\Delta p}{gL_v}\frac{L_v q'_L}{\tau_q}, \tag{2.16}$$

$$P'_{estH} = \frac{\Delta p}{gL_v}\frac{h'_B}{\tau_h}. \tag{2.17}$$

We will apply these definitions to understand the relative contributions of these components to AEW and PEW-related rainfall.

### 2.3.2 Scale Analysis

The governing thermodynamics of PEWs and AEWs can be understood through the application the scale analysis performed by Adames et al. (2019) and Adames (2022). Through scale analysis of a simple moist shallow water model, Adames et al. (2019) defined a nondimensional quantity they referred to as $\mathrm{N}_{mode}$ that describes the "relative contribution of moisture and temperature to the evolution of moist enthalpy". It is written as:

$$\mathrm{N}_{mode} \simeq \frac{c_p^2 \tau}{c^2 \tau_c}, \tag{2.18}$$

where $c$ is the gravity wave phase speed ($c \sim 50$ m s$^{-1}$ for first baroclinic mode), $\tau$ is the wave's timescale, and $\tau_c$ is the convective moisture adjustment timescale. The scale analysis was generalized to the full atmosphere by Adames (2022), who obtained the following expression for $\mathrm{N}_{mode}$

$$\mathrm{N}_{mode} \equiv \frac{c_p^2}{c^2 \hat{\alpha}(1-\hat{\alpha})}, \tag{2.19}$$

where $\hat{\alpha}$ is the scale of the ratio of the vertical gradients of latent energy ($L_v q$) and dry static energy, also known as the Chikira (2014) parameter.

Both Adames et al. (2019) and Adames (2022) showed that when $N_{mode} \ll 1$ the anomalies in $L_v q$ are much larger than the anomalies in dry enthalpy ($C_p T$) and dominate the thermodynamic evolution of the wave, resulting in moisture modes. According to Adames (2022), moisture modes exhibit characteristic phase speeds of $\sim$5 m s$^{-1}$ or less. On the

other hand, gravity waves exhibit $N_{mode} \gg 1$, and $c_p \geq 30$ m s$^{-1}$. In this study we will broadly define moisture modes as any system whose $N_{mode}$ value is 0.2 or less.

### 2.3.3 Moisture Mode Criteria

While the value of $\mathrm{N}_{mode}$ provides important information on the processes that govern the thermodynamic evolution of transients, further assessment is needed to determine if a wave is a moisture mode. Ahmed et al. (2021) developed three diagnostic criteria to assess whether a wave is a moisture mode. This idea was recently modified by Mayta et al. (2022) to make it more applicable to model, reanalysis, and observational data. They state that moisture modes must satisfy the following three conditions:

1. Column integrated moisture must be highly coherent with precipitation and must be able to explain most of its variance, such that:

$$\langle q \rangle' \propto P'. \tag{2.20}$$

2. The mode must be in weak temperature gradient (WTG) balance:

$$\nabla \cdot \langle s\mathbf{v} \rangle' \simeq \langle Q_1 \rangle'. \tag{2.21}$$

where $s' = \langle C_p T \rangle' + \langle \Phi \rangle'$ is the dry static energy, and $\langle Q_1 \rangle' = \langle Q_R \rangle' + L_v P' + H'$ is the apparent heating rate, where $Q_R$ is the radiative heating, and $H$ is the

surface sensible heat flux. Thus, in WTG balance the vertical advection of $s$ will be predominantly driven by diabatic heating.

3. Latent energy governs the distribution of column-integrated moist static energy ($m$):

$$\langle m \rangle' = \langle C_p T \rangle' + \langle \Phi \rangle' + \langle L_v q \rangle' \approx \langle L_v q \rangle'. \tag{2.22}$$

To satisfy the first criterion, the correlation between $\langle q \rangle'$ and $P'$ must be higher than 0.9 rounded to the first decimal. For criterion two and three, the slope between $\nabla \cdot \langle s\mathbf{v} \rangle'$ and $\langle Q_1 \rangle'$, and $\langle m \rangle'$ and $\langle L_v q \rangle$ must be between 0.9-1.1 rounded to the nearest decimal, in addition to a high correlation ($\sim 0.9$).

## 2.4 Results

### 2.4.1 $q$ and $T$ climatology

To get a better picture of the large scale thermodynamic environment over the EPAC and WAEA, Fig. 2.3 shows the climatologies for $q_L$ ($\overline{q}_L$) (Fig. 2.3.a,d), $T_L$ ($\overline{T}_L$) (Fig. 2.3.b,e), and $m_L$ ($\overline{m}_L$) (Fig. 2.3.c,f) in these regions. We also overlay Fig. 2.3 with the the root mean square (RMS) amplitude of $P'$ for PEWs and AEWs. The RMS amplitude of $P'$ is obtained as the square root of the square of $P'$ regressed onto PC1 and PC2 of EW activity, i.e. $P'_{rms} = \sqrt{P'(PC1)^2 + P'(PC2)^2}$. When we examine the horizontal distribution of $\overline{q}_L$, we see that over WAEA the maximum values are zonally distributed along 10°N. In contrast, the distribution over the EPAC exhibits two regions

where moisture is a local maximum: one following the ITCZ band near 10°N, and another following the southern coastline of Central America and Mexico.

Comparing the horizontal structure of $\overline{T}_L$ between the two basins reveals that the horizontal gradient in $\overline{T}_L$ is stronger over WAEA than over the EPAC. Over the WAEA, the maximum in $\overline{T}_L$ values centered over the western Sahara around 15°W-15°E and 17°N-30°N. As a result, the horizontal temperature gradient over western Africa is dominated by its meridional component. In contrast, the horizontal $\overline{T}$ gradient over the EPAC is weaker and is oriented towards northern Mexico.

It is also instructive to examine the distribution of $m_L$. Recent studies have shown that in the presence of a strong horizontal $\overline{m}_L$ gradient ($\nabla\overline{m}_L$) to the north of a EW-like disturbance, meridional $\overline{m}$ advection can induce their growth (Adames and Ming, 2018, Clark et al., 2020, Diaz and Boos, 2019, 2021a,b). Over the EPAC $\overline{m}$ has a similar horizontal structure to $\overline{q}_L$, although the local maximum over southern Mexico is amplified and hence larger than the maximum along the ITCZ. In contrast, the distribution of $\overline{m}_L$ exhibits a maximum near 15°N over Africa. This position is equatorward of the $\overline{T}_L$ maximum, but north of the $L_v\overline{q}_L$ maximum, suggesting that the $\overline{m}_L$ maximum has comparable contributions from the two fields.

In order to get a qualitative understanding of how the EWs propagate with respect to the distribution of $L_v\overline{q}_L$, $C_p\overline{T}_L$ and $\overline{m}_L$, we examine the $P'_{rms}$ structure in Fig. 2.3. The resulting patterns reveal that $P'$ (Fig. 2.3), follows the $\overline{q}$ maximum over the WAEA and EPAC regions, as posited by previous studies (Kiladis et al., 2006, Rydbeck and

Maloney, 2015, Thorncroft and Hoskins, 1994a,b). Over western Africa, $P'$ is a maximum south of the $\overline{m}_L$ maximum near the region where its gradient is strongest. This also seems to be the case over the EPAC, although the fact that there are two local maxima in $\overline{m}_L$ complicates this interpretation. Other sources, such as gradients in potential vorticity could be contributing to the evolution of the system over the EPAC (Torres and Thorncroft, 2022).

### 2.4.2 Horizontal Structure of PEWs and AEWs

To understand the convective coupling mechanism of EWs Fig. 2.4 shows $P'$, $z'$, and $\mathbf{v}'$ regressed upon PC1 of EW activity. The results for PC2 are consistent with Fig. 2.4 and are presented in Fig. S1. The left column shows PEWs while the right column shows AEWs. The regression maps show regions of alternating high and low $z'$ with cyclonic (anticyclonic) flow around the low (high) that are characteristic of these disturbances (Cheng et al., 2019, Rydbeck and Maloney, 2015). A close examination of the PEW structure reveals a SW-NE horizontal tilt in $P'$, captured by previous studies (e.g., Serra et al., 2008, Serra et al., 2010, Rydbeck and Maloney, 2014, Rydbeck and Maloney, 2015). As described in the preceding section, PEWs propagate along a path oriented from SE-NW. On the other hand, AEWs have a propagation that is predominantly zonal.

The second row of Fig. 2.4 shows $P'_{est}$. A close correspondence between $P'_{est}$ and $P'$ is observed over both regions. The similarity of these patterns is robust whether reanalysis or satellite rainfall is used (see Fig. B.1). The final two rows of Fig. 2.4 show the contributions of $P'_{estQ}$ and $P'_{estT}$ to $P'_{est}$. In PEWs along 10°N it is clear that $P'_{estQ}$ is the

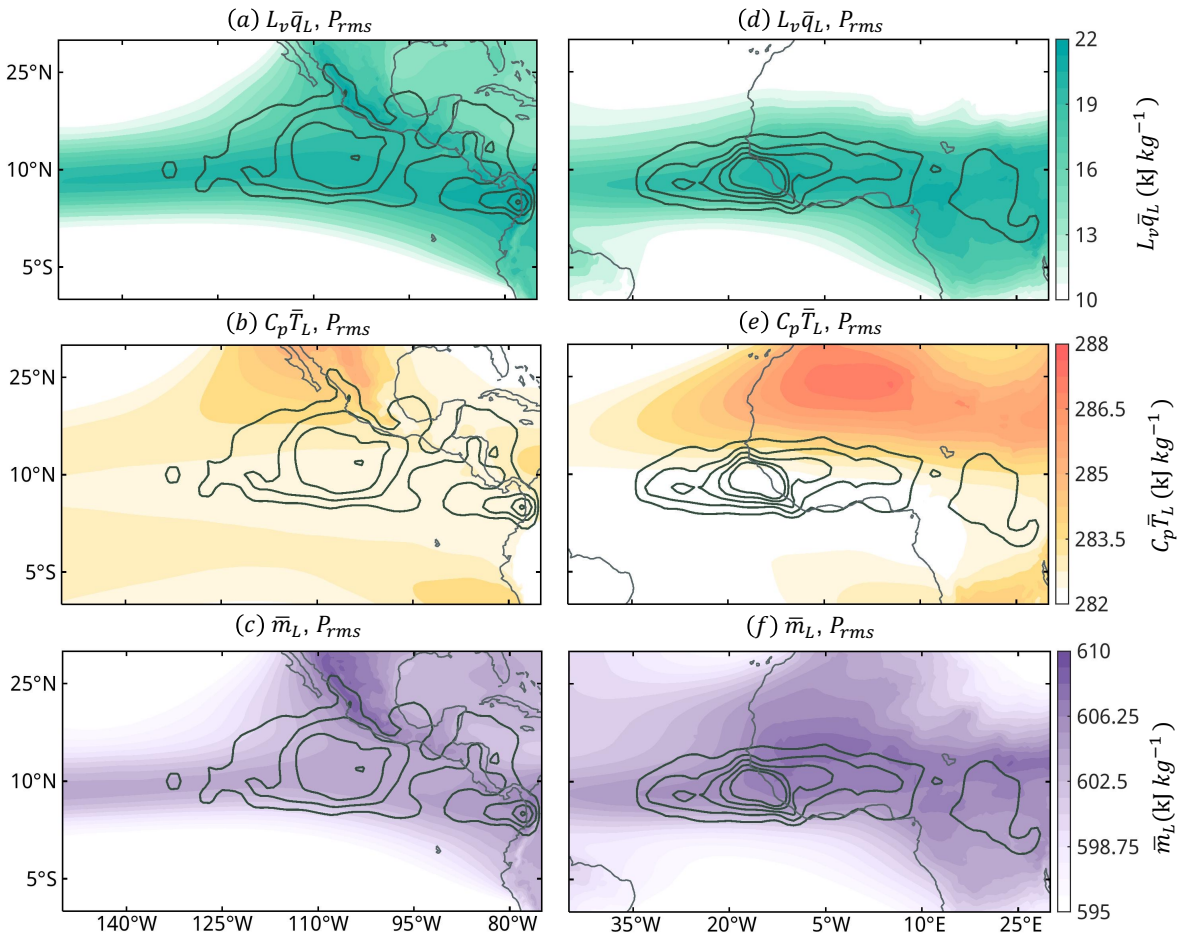


FIGURE 2.3: Horizontal maps of 600-850 hPa average (top) $L_v q_L$ (shading with units of $kJ\ kg^{-1}$), (middle) $C_p T_L$ (shading with units of $kJ\ kg^{-1}$), and (bottom) $m$ (shading with units of $kJ\ kg^{-1}$) averaged for the months of July-August-September (JAS) over (left) the EPAC and (right) WAEA regions. The root mean square (RMS) amplitude of anomalous precipitation ($P'_{rms}$) for PEWs and AEWs is overlaid as solid contours in all the panels.

dominant contributor to $P'_{est}$, with $P'_{estT}$ showing larger contributions for PC2, and only for the anomalous anticyclone that is south of the coast of Mexico (see Fig. S1). However, over the Panama Bight region $P'_{estT}$ has the largest contribution to $P'_{est}$. Previous studies have suggested that PEWs generation can be attributed to local convective forces (Rydbeck et al., 2017, Thorncroft et al., 2008, Torres et al., 2021, Whitaker and Maloney, 2020). Mesoscale convective systems (MCS) over the Panama Bight have been found to originate from temperature anomalies associated with the gravity wave response resulting from diurnal temperature changes over the Colombian Andes (Mapes et al., 2003, Warner et al., 2003). For example, a regional modeling study by Rydbeck et al. (2017) showed a significant reduction in PEW activity as topography over South America decreased, highlighting the importance of these frequent MCSs (Mapes et al., 2003) for in-situ PEW generation. Following these previous findings, since Fig. 2.4d shows that $P'_{estT}$ is the dominant contributor to $P'_{est}$ over the Panama Bight, this suggests that the EW-related precipitation relevant to this analysis could come from temperature anomalies from the gravity wave response as suggested by Rydbeck et al. (2017). On the other hand, $P'_{estQ}$ and $P'_{estT}$ are of comparable magnitude in AEWs. These results are consistent with the findings of Wolding et al. (2020), who found that column saturation fraction explains a larger fraction of rainfall in PEWs than in AEWs. The contribution of $P'_{estH}$ was found to be negligibly small for both PEWs and AEWs, and hence it is not shown. Thus, precipitation in PEWs is predominantly driven by $q'_L$ while for AEWs both $q'_L$ and $T'_L$ play comparable roles.

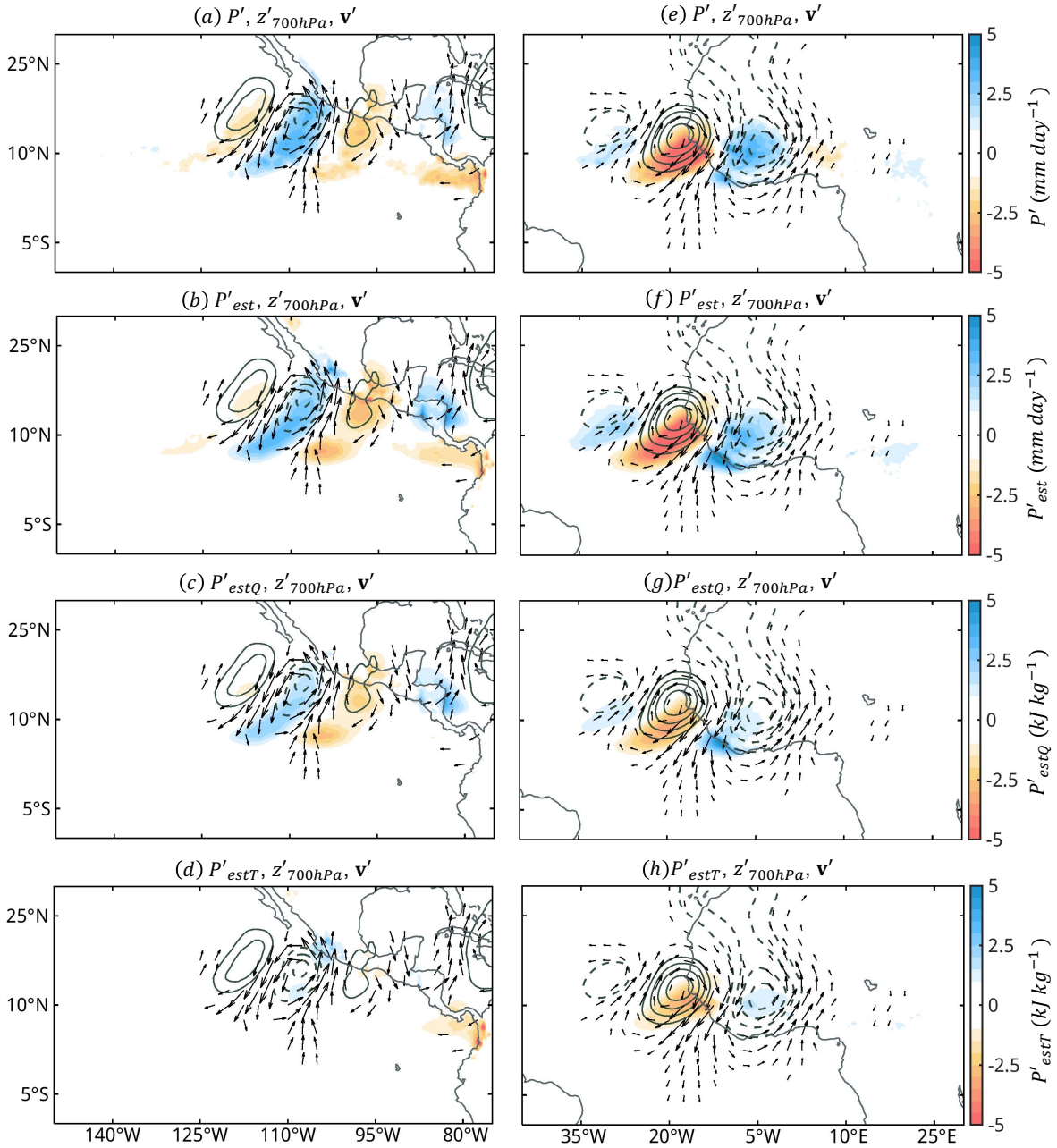


FIGURE 2.4: Anomalous ERA5 precipitation ($P'$), estimated precipitation ($P'_{est}$), contribution of specific humidity ($q'$) to $P'_{est}$ ($P'_{estQ}$), contribution of temperature ($T'$) to $P'_{est}$ ($P'_{estT}$) (shaded fields), geopotential height ($z'$) (contours), and horizontal winds ($\mathbf{v}'$) (vectors), regressed upon PC1 of (left) PEWs and (right) AEWs. Contour interval is 0.5 m, starting at 1 m. The longest arrows correspond to a wind anomaly of 1.8 m s$^{-1}$.

### 2.4.3 EW-related precipitation in a buoyancy framework

To further show the robustness of the relationship between $P'_{est}$ and $P'$, Fig. 2.5 shows a scatterplot of the two fields for PEWs and AEWs. In both PEWs and AEWs the cloud of points is tightly clustered, with a correlation coefficient ($r$) of 0.94 for both PEWs and AEWs. This result implies that the plume buoyancy framework can explain ∼88% of the EW-related rainfall variance in ERA5. Moreover, the slopes ($\mu$) of the linear least squares fit are near unity, showing that $P'_{est}$ also adequately explains the amplitude of anomalous rainfall in EWs.

Table 2.3 summarizes the $r$ and $\mu$ values of $P'_{estQ}$, $P'_{estT}$, and $P'_{estH}$ when compared to $P'$. The results of Fig. 2.5 are also included, for reference. While the scatterplots showing these values are not included in the main text they are presented in Fig. S2. From Table 2.3 we see that $P'_{estQ}$ is also highly correlated with $P'$, with values being just slightly smaller than $P'_{est}$. However, the slope of the linear least squares fit is substantially smaller. It is larger for PEWs than for AEWs. This result indicates that moisture explains a larger fraction of the $P'$ in PEWs than in AEWs, as the results of Fig. 2.4 indicate. When examining the relationship between $P'_{estT}$ and $P'$ we see that correlations are still high but are substantially smaller than those of $P'_{est}$ and $P'_{estQ}$ for PEWs, while comparable values were attained for AEWs. Overall, $P'_{estT}$ is more correlated with $P'$ and exhibits a higher $\mu$ in AEWs than in PEWs, underscoring the importance of temperature fluctuations in the convective coupling of AEWs, as Wolding et al. (2020) indicated. When comparing

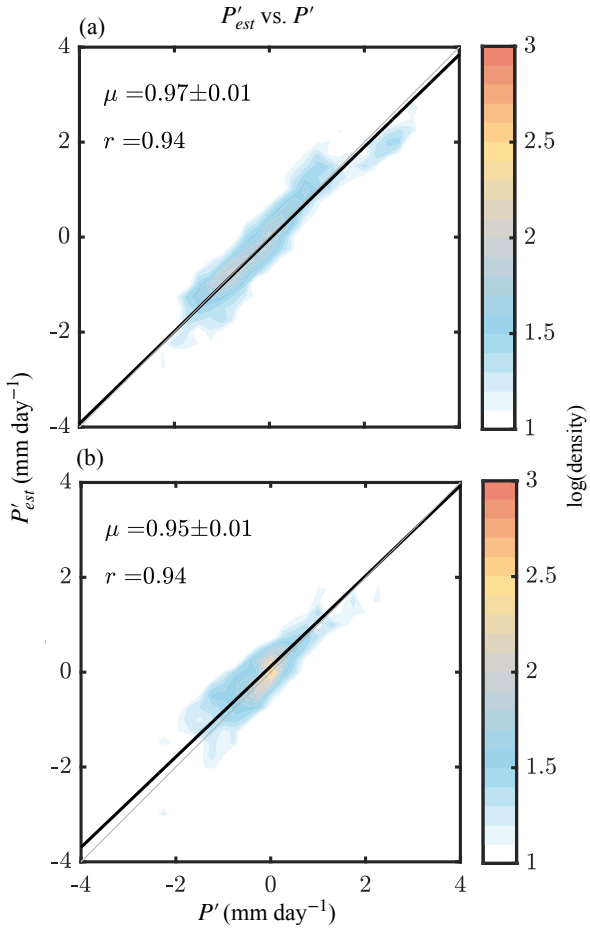


FIGURE 2.5: Scatterplot of anomalous estimated precipitation ($P'_{est}$) against ERA5 precipitation ($P'$) for (a) PEWs and (b) AEWs. The shaded field shows the base 10-logarithm of the number of data points in each bin. Values are binned every 0.25 × 0.25 mm day$^{-1}$. The one-to-one line is shown in light gray and the slope ($\mu$) and correlation coefficient ($r$) are shown in the top-left of each panel. The black line shows the linear least squares fit regression of the two fields. The relationships are determined over the region of strongest EW activity, 125°W-90°W and 5°N-20°N for PEWs and 27.5°W-10°E and 5°N-20°N for AEWs.

the $\mu$ values of $P'_{estQ}$ and $P'_{estT}$, we see that $P'_{estQ}$ contributes nearly three times more to $P'_{est}$ in PEWs, whereas $P'_{estQ}$ and $P'_{estT}$ play comparable roles in AEW precipitation.

TABLE 2.3: Correlation coefficients (r) and slopes ($\mu$) of the relationship between $P'$, $P'_{est}$, $P_{estQ}$, $P'_{estT}$, and $P'_{estH}$. The relationships are determined over the region of strongest EW activity, 125°W-90°W and 5°N-20°N for PEWs and 27.5°W-10°E and 5°N-20°N for AEWs.

| | *Pacific* | | *Africa* | |
|---|---|---|---|---|
| | $r$ | $\mu$ | $r$ | $\mu$ |
| $P'_{est}$ *vs.* $P'$ | 0.94 | 0.97 | 0.94 | 0.95 |
| $P'_{estQ}$ *vs.* $P'$ | 0.90 | 0.68 | 0.89 | 0.55 |
| $P'_{estT}$ *vs.* $P'$ | 0.81 | 0.30 | 0.87 | 0.41 |
| $P'_{estH}$ *vs.* $P'$ | -0.03 | 0.00 | -0.10 | -0.01 |

TABLE 2.4: Phase speed ($c_p$) and $N_{mode}$ values for PEWs and AEWs.

| | | $c_p$ | $N_{mode}$ | |
|---|---|---|---|---|
| | | | Adames et al. (2019) | Adames (2022) |
| Pacific | PC1 | -7.11 | 0.22 | 0.10 |
| | PC2 | -6.86 | 0.20 | 0.09 |
| Africa | PC1 | -9.15 | 0.38 | 0.20 |
| | PC2 | -10.26 | 0.48 | 0.26 |

### 2.4.4 Contribution of $q$ and $T$ to PEW and AEW thermodynamics

#### 2.4.4.1 $N_{mode}$

In addition to their role in modulating convection, $T'$ and $q'$ can play an important role in the governing mechanisms of propagation and growth of EWs (Mayta and Adames, 2023). To understand their relative contributions, we will examine the nondimensional $N_{mode}$ parameter proposed by Adames et al. (2019) (Eq. (2.18)) and Adames (2022)

(Eq. (2.19)). In order to obtain a value of these parameters, we first need to obtain estimates for the zonal phase speeds of PEWs and AEWs. These speeds are obtained from the time-longitude diagrams in Fig. 2.6. The lagged regressions in these diagrams were meridionally averaged over 5°N−20°N, where wave activity is strongest. The phase speed calculated from the Radon transform for OLR' ($c_{OLR}$) is shown in Table 2.4. From these, we can see that PEWs exhibit slower propagation speeds than AEWs.

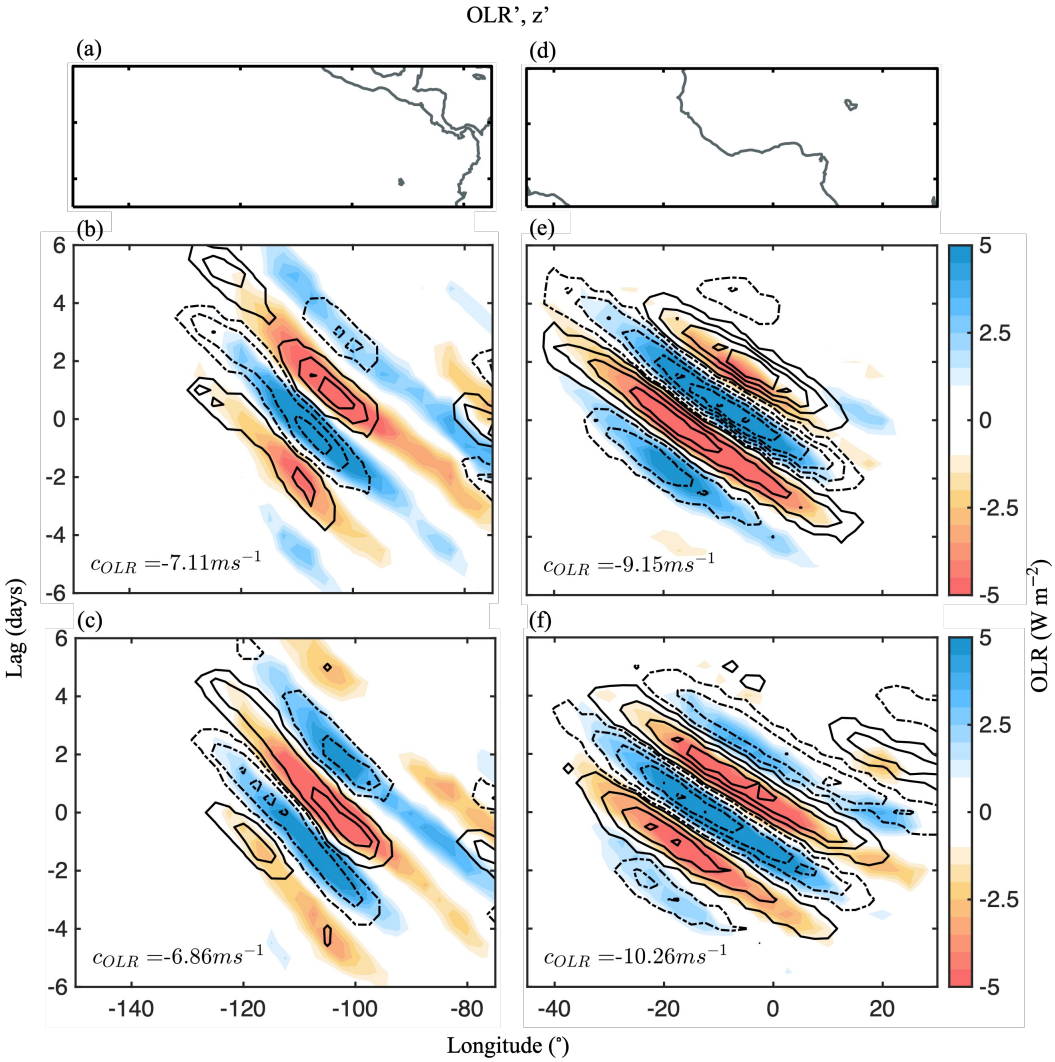


FIGURE 2.6: Time-longitude diagrams of outgoing long-wave radiation (OLR) (shaded) and geopotential height ($z'$) (contoured) lag regressed onto (b and e) PC1 and (c and f) PC2 of (left) PEW and (right) AEW activity. The fields were averaged over the 5°N-20°N latitude belt. The contour interval is 0.35 m, starting at 0.1m. The EPAC and WAEA regions are shown in panels (a) and (d), for reference. The data presented has a horizontal resolution of 2.5°×2.5° and a 12 hr temporal resolution.

$\mathrm{N}_{mode}$ values are determined from Eq. (2.18) by assuming a first baroclinic wave structure over both regions ($c \sim 50$ m s$^{-1}$, see Appendix C), estimating $\tau$ from the time-longitude diagrams as the period it took for a wave to complete an entire life cycle ($\sim$4 days for both waves) and the values for $\tau_c$ were determined from Fig. 2.7.a,d, taking the $\mu$ of the relationship between the column integrated $q'$ and $P'$ over the EPAC and WAEA (0.37 and 0.35 days, respectively). Similarly, to evaluate Eq. (2.19), we calculate $\overline{\alpha}$ for the atmospheric column neglecting the planetary boundary layer (PBL) (850 hPa $-$100 hPa). The resulting values for Eq. (2.18) and (2.19) are presented in Table 2.4. Both calculations indicate that moisture governs the thermodynamics of PEWs ($\overline{N_{mode}} = 0.15$), suggesting that they are moisture modes, consistent with Mayta and Adames (2023). Moisture and temperature play comparable roles in AEWs ($\overline{N_{mode}} = 0.33$), suggesting that they are mixed systems.

#### 2.4.4.2 The thermodynamic contributions to rainfall and $\mathbf{N}_{mode}$

In PEWs temperature plays a non-negligible role in $P'_{est}$ even though $\mathrm{N}_{mode}$ is much smaller than unity. If we follow the same scale analysis performed by Adames (2022) but applied to $P'_{est}$, we find that the relative amplitude of $P'_{estT}$ with respect to $P'_{estQ}$ follows the relationship:

$$\frac{P'_{estT}}{P'_{estQ}} \sim \frac{\tau_q}{\tau_t}\mathrm{N}_{mode}. \tag{2.23}$$

TABLE 2.5: $P'_{estT} - P'_{estQ}$ ratio calculated from Table 2.3 (Calc) and the right-hand side of Eq (2.23).

| | Calc | Eq (2.23) |
|---|---|---|
| Pacific | 0.44 | 0.31-0.67 |
| Africa | 0.75 | 0.71-1.34 |

We calculated the average value of $\tau_q/\tau_t$ from Eq. (2.11) and (2.12) during JAS for both the EPAC and WAEA domains, and found values of 3.08 and 3.53, respectively. These are similar to the global value obtained by Ahmed et al. (2020) of 4. With these ratios and the values of $P'_{estT}$ and $P'_{estQ}$ in Table 2.3, we can compare the ratio $P'_{estT}/P'_{estQ}$ (Calc) in PEWs and AEWs with the results obtained from Eq. (2.23). Both results are shown in Table 2.5.

From Eq. 2.23 we obtain a $P'_{estT}$-$P'_{estQ}$ ratio between 0.31-0.67 for PEWs and 0.71-1.34 for AEWs. Using the $P'_{estT}$-$P'_{estQ}$ values from Table 2.3 we obtain a ratio of 0.44 for PEWs and 0.75 for AEWs. Showing that the numbers obtained are in agreement for both transients.

#### 2.4.4.3 Moisture Mode Criteria

We will now assess the three moisture mode criteria beginning with the relationship between $\langle q \rangle'$ and $P'$. This first criterion is presented in Fig. 2.7.a,d for PEWs and AEWs respectively. The $r$ values are high for PEWs ($r = 0.90$), and moderate for AEWs ($r = 0.69$). While the results from the scale analysis in the preceding section indicate

that $P'_{estT}$ can play a non-negligible role in moisture modes, in PEWs $\langle q \rangle'$ exhibits high coherence with $P'$. This result suggests that $\langle q \rangle'$ is the field dominating the dynamics of the transient over this region. Thus, the condition is only met by the waves over the EPAC.

The second criterion is presented in Fig. 2.7.a,b for PEWs and AEWs respectively. The $r$ value of $\nabla \cdot \langle s\mathbf{v} \rangle$ and $\langle Q_1 \rangle$ is high in both waves. The $\mu$ value is close to unity for both PEWs ($\mu = 0.88 \pm 0.01$) and AEWs ($\mu = 0.97 \pm 0.01$). Given that $\mu$ should be close to 0.9, this result suggest that both AEWs and PEWs satisfy this condition.

Finally, the third criterion is shown in Fig. 2.7.c,d for PEWs and AEWs respectively. The relationship between $\langle q \rangle'$ and $\langle m \rangle'$ is strong for both PEWs ($r \approx 1.00$ and $\mu \approx 1.02$) and AEWs ($r = 0.99$ and $\mu \approx 1.14$). While the one-to-one relationship is stronger for PEWs, both transients satisfy this condition.

## 2.5 Discussion and Conclusions

In this study we sought to further understand the role that $q$ and $T$ play in the thermodynamic evolution of AEWs and PEWs. The employed linear regression analysis revealed that $P'_{est}$, as determined from the buoyancy-centric framework (Adames et al., 2021, Ahmed et al., 2020, Ahmed and Neelin, 2018), was successful in capturing both reanalysis and satellite observed precipitation, thus underscoring the relevance of $q'$ and

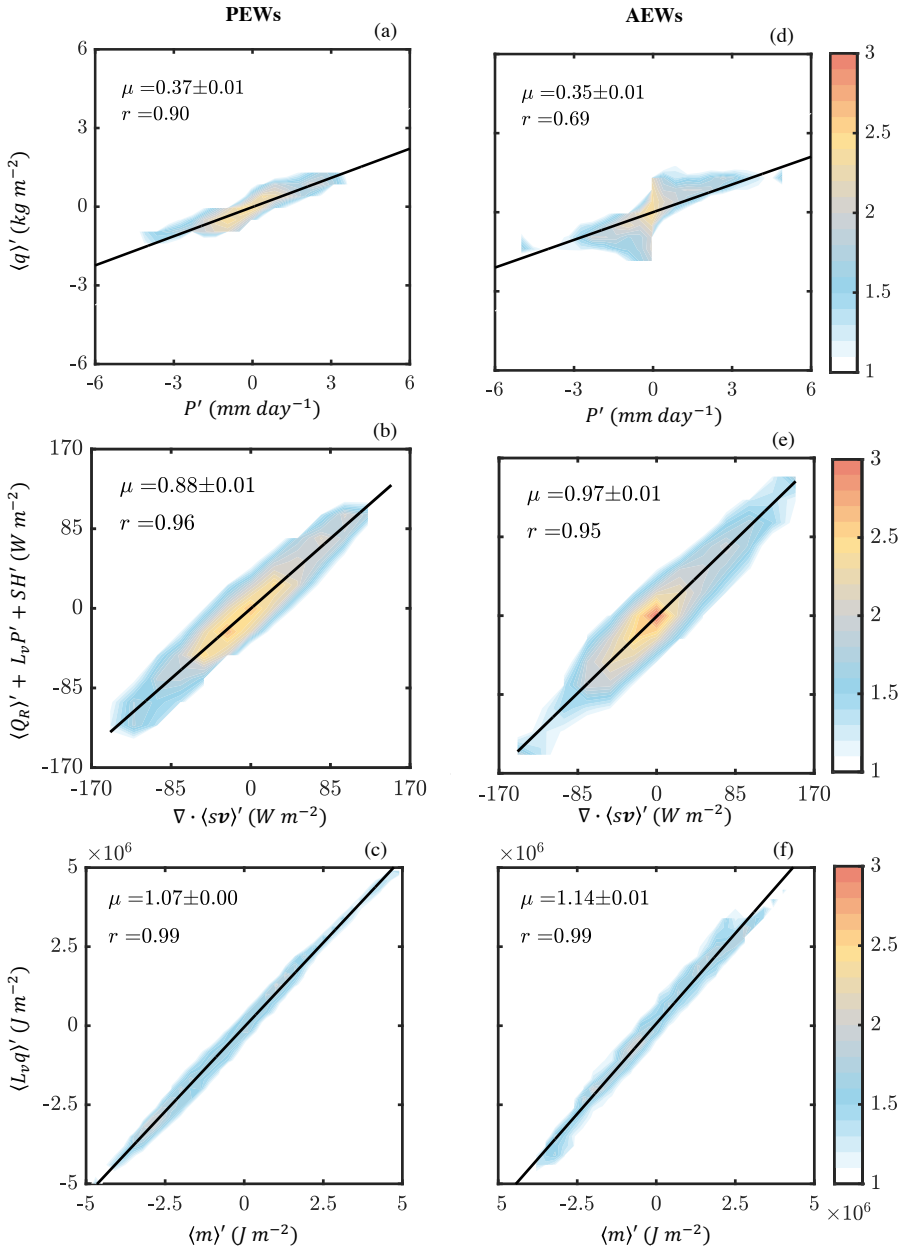


FIGURE 2.7: As in Fig. 2.5, but showing (a and d) the column integrated humidity ($\langle q \rangle'$) against the precipitation rate ($P'$), (b and e) as the apparent heating rate ($\langle Q1 \rangle' \simeq \langle Q_R \rangle' + L_v P' + SH'$) against the advection of dry static energy ($\nabla \cdot \langle s\mathbf{v} \rangle'$), and (b and d) latent energy ($\langle L_v q \rangle$') against moist static energy ($\langle m \rangle'$) for PEWs (left column) and AEWs (right column). Values are binned every 0.45 kg m$^{-2}$ $\times$ 0.45 mm day$^{-1}$ in (a) and (d), 25 $\times$ 25 W m$^{-2}$ in (b) and (e), and every 0.30$\times$10$^6$ $\times$ 0.30$\times$10$^6$ J m$^{-2}$ for (c) and (f). The relationships are determined over the region of strongest EW activity, 125°W-90°W and 5°N-20°N for PEWs and 27.5°W-10°E and 5°N-20°N for AEWs. The slope ($\mu$) and the correlation coefficient ($r$) are shown on the top-left corner of each panel.

$T'$ in the convective evolution of the modes. Close assessment of the governing thermodynamics on the basis of WTG and moisture mode theory revealed that PEWs are governed by moist dynamics while AEWs are governed by both $q'$ and $T'$.

Initial examination of $\overline{q}$, $\overline{T}$, $\overline{m}$, and the RMS of the leading wave patterns revealed that the waves propagate along the $\overline{q}$ maximum and perpendicular to the horizontal $\overline{m}$ gradient.

On the basis of linear regression analysis, we found that the plume buoyancy framework developed by Ahmed and Neelin (2018), Ahmed et al. (2020), and Adames et al. (2021) accurately diagnoses PEW- and AEW-related precipitation. The $r$ value between $P'$ and $P'_{est}$ was found to exceed 0.9 and the $\mu$ between the two fields was found to be near unity for both waves (Fig. 2.5). Examining the contributions of $q'$ and $T'$ to the buoyancy-based rainfall estimate shows that $q'$ dominates PEW precipitation (except in the Panama Bight, where $T'$ contributions are stronger), while $q'$ and $T'$ contribute almost equally to AEW precipitation.

We also examined the relative magnitudes of $L_v q'$ and $C_p T'$, which can elucidate where AEWs and PEWs fit in the the moisture mode-gravity wave spectrum discussed in previous studies (Adames, 2022, Adames et al., 2019, Inoue et al., 2020). Examination of a nondimensional parameter, $N_{mode}$ (Table 2.4), indicates that PEWs are moisture modes (Mayta and Adames, 2023), while AEWs are mixed waves with properties of both moisture modes and gravity waves. The main difference is attributed to the slower $c_p$ PEWs exhibit when compared to AEWs (Table 2.4).

In spite of the much larger magnitude of the $q_L$ anomalies relative to the $T_L$ anomalies in PEWs (see Appendix A), $P'_{estT}$ was still found to contribute significantly to $P'_{est}$. Scale analysis of $P'_{est}$, revealed that this result is due to the fact that $P'_{est}$ is 3-4 times more sensitive to $T'$ than to $q'$ (Ahmed et al., 2020). Thus, even though the $m$ budget of moisture modes is governed by $L_v q$, $T$ anomalies can still contribute significantly to moisture-mode related rainfall. This is an interesting finding that will be examined more carefully in the future.

An analysis of the three moisture mode criteria proposed by Mayta et al. (2022), (1) $q' \propto P'$, (2) $\nabla \cdot \langle s\mathbf{v} \rangle' \simeq \langle Q1 \rangle'$, and (3) $\langle m' \rangle \simeq \langle L_v q' \rangle$, yielded results that are in line with the $\mathrm{N}_{mode}$ analysis. We find that PEWs satisfy all three criteria (Mayta and Adames, 2023), while AEWs only satisfy two. Similar observations were made by previous studies, where the convective coupling of PEWs was found to be dominated by $q$ (Mayta and Adames, 2023, Wolding et al., 2020), while adiabatic motions were more prominent for AEWs (Kiladis et al., 2006, Wolding et al., 2020). These findings support previous studies that propose moist convection is as important as dry dynamics for the growth of AEWs (Berry and Thorncroft, 2012), while the former dominates the dynamics of PEWs (Lau and Lau, 1992, Mayta and Adames, 2023, Rydbeck and Maloney, 2015, Serra et al., 2008, 2010, Wolding et al., 2020). The results from the three criteria also highlight important distinct processes modulating the modes. The key findings of this study are summarized in Fig. 2.8. Over WAEA the convective center is located ahead of the trough axis, while the opposite is true over the EPAC. Once AEWs enter the Atlantic Ocean, the structure becomes similar to that of PEWs, in agreement with findings by Mayta and Adames

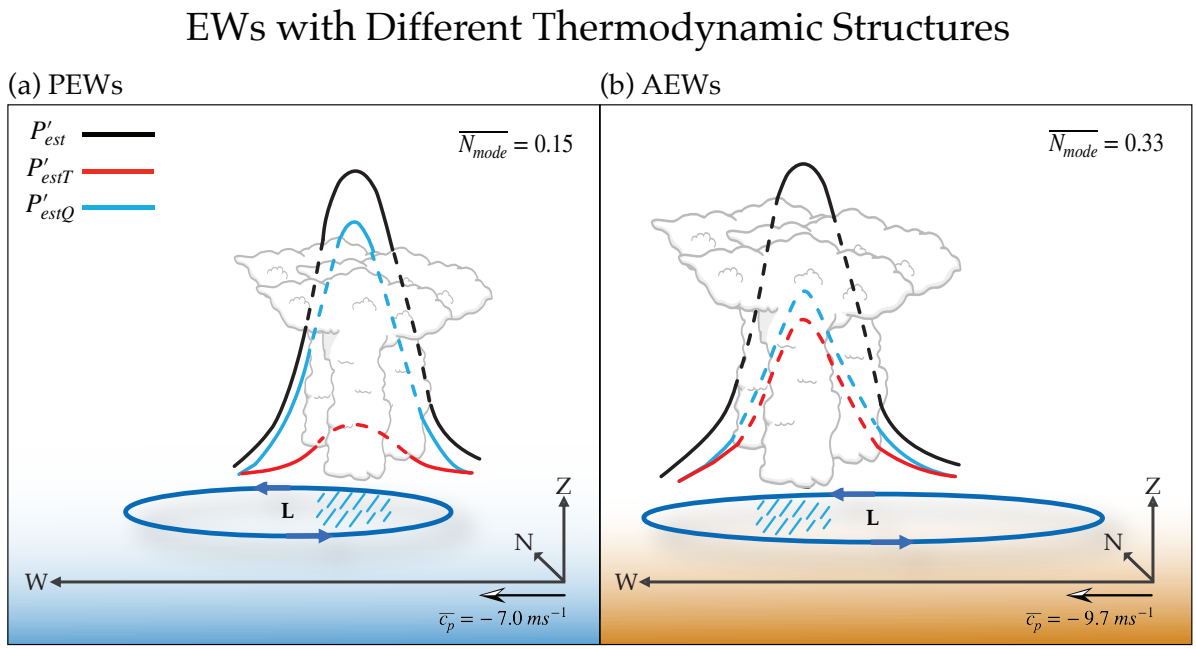


FIGURE 2.8: Schematic describing the relative magnitude of total estimated precipitation ($P'_{est}$) (black line), along with its components due to moisture ($P'_{estQ}$) (cyan line) and temperature ($P'_{estT}$) (red line) for (a) PEWs and (b) AEWs. Areas of enhanced precipitation are depicted by the convective clouds and rain. The horizontal circulation is shown by the blue arrows. Blue and orange shading has been added to distinguish waves with origin over (a) ocean, and (b) land respectively. The $N_{mode}$ (top right) and phase speed ($c_p$) (bottom right) values are included for comparison. The thermodynamic structure of (a) PEWs and (b) AEWs are representative of off-equatorial moisture modes and mixed systems as presented by Adames (2022).

(2023). This result highlights the importance of the continent for the thermodynamic evolution of the wave over this region. In agreement with the results of Adames and Maloney (2021), over the EPAC gravity waves eliminate $T'$ before the convection dissipates, this leads to the dominance of $q'$ throughout the convective evolution of the transient, characteristic of moisture modes. On the other hand, these processes are balanced over the WAEA region, and thus the evolution of the system is modulated by both $T'$ and $q'$, characteristic of mixed waves. As a consequence, PEWs more robustly adjust to WTG balance.

*Acknowledgments.* This material is based upon work supported by the National Science Foundation Graduate Research Fellowship Program under Grant No. DGE-1747503. Any opinions, findings, and conclusions or recommendations expressed in this material are those of the authors and do not necessarily reflect the Views of the National Science Foundation. Support was also provided by the Graduate School and the Office of the Vice Chancellor for Research and Graduate Education at the University of Wisconsin-Madison with funding from the Wisconsin Alumni Research Foundation. RVM also thanks Qiao-Jun Lin, Pete Pokrandt and the Large-scale Tropical Dynamics group for all the help and conversations that facilitated portions of the data analysis presented in this paper. The authors also thank the contributions of three anonymous reviewers that ultimately improved the final version of this manuscript.

The data used in the study is property of the European Centre for Multi-range Weather Forecasting (ECMWF), and is openly available online via `https://www.ecmwf.int/en/forecasts/datasets/reanalysis-datasets/era5/`. TRMM/GPM data was provided by NOAA/ESRL.

# Chapter 3

# East Pacific Easterly Wave Representation in CMIP6 Models

Vargas Martes, R. M., Á. F. Adames Corraliza, V. C. Mayta, and Q.-J. Lin, 2024: East pacific easterly wave representation in CMIP6 models.

https://doi.org/10.22541/essoar.173046728.84436944/v1.

© Copyright by Rosa M. Vargas Martes, Ángel F. Adames Corraliza, Víctor Mayta, Qiao-Jun Lin (2024)

**Key Points**

- CMIP6 models are sorted by their ability to represent East Pacific Easterly Waves.
- Unrealistically weak models exhibit small precipitation anomalies relative to good models, even though moisture fluctuations are comparable.
- Models with larger precipitation anomalies have weaker meridional humidity gradients and higher precipitation over the Panama Bight.

# Abstract

The representation of easterly waves (EWs) over the east Pacific Ocean (PEWs) in Coupled Model Intercomparison Project phase 6 (CMIP6) simulations is examined. Models are assessed based on their ability of reproducing PEW-related precipitation and its evolution. The leading patterns reveal a large spread in the representation of PEW structure and amplitude. A comparison of the models with the most realistic PEWs with those with unrealistically weak PEW skill showed that the more accurate simulations more effectively capture the mean state and EW thermodynamic structures over the northeast Pacific. Particularly, good models exhibit realistic PEW precipitation, weaker meridional mean state humidity gradients, larger mean state precipitation over the Panama Bight, and realistic convective moisture adjustment timescales. These results underscore the importance of accurately representing the sensitivity of PEW convection to anomalous moisture for the realistic representation of the waves.

## Plain Language Summary

Easterly Waves (EWs) are westward propagating regions of high and low pressure that co-evolve and are tied to regions of enhanced and suppressed cloudiness in the tropical atmosphere. While we now have global climate simulations (i.e. models, GCMs) that help us understand how our atmosphere evolves on short (a few days) and climate timescales (longer than 30 years), accurately simulating easterly waves (EWs) remains a challenge. Thus, this study examines the Coupled Model Intercomparison Project simulations and compares them to data from the Fifth Reanalysis from the European Centre for Medium-Range Weather Forecasts. We find that models have difficulty in reproducing the strength of the waves and the spatial distribution of cloudiness in PEWs. Further analysis reveals that good simulations also better capture the wave-related rainfall, mean rainfall over the Panama Bight region, less changes of humidity with latitude, and realistic capture the time it takes the waves to remove anomalous moisture from the atmosphere. Finally, our results indicate that in order to simulate PEWs realistically, it matters not only how moisture is represented in the simulations, but how the wave precipitation responds to anomalous moisture in the GCMs.

## 3.1 Introduction

The tropical atmosphere is the arena of a menagerie of convectively coupled tropical waves. Arguably, the most well-known of these are tropical depression-like (TD-like) systems, such as easterly waves (EWs), with westward wavenumbers ($k$) 5-20 and periods

from 2.5-10 days (e.g., Feng et al., 2020, Kiladis et al., 2009, Mayta and Adames Corraliza, 2024). These transient waves are regions of alternating high and low pressure that are coupled to convection and are ubiquitous in the tropical atmosphere (Lau and Lau, 1990, Mayta and Adames Corraliza, 2024). Across the western hemisphere, Tropical Northeast Pacific Easterly Waves (PEWs) play a significant role in the hydrological cycle of the tropical Northeast Pacific Ocean (Dominguez et al., 2020, Fahrin et al., 2024). Furthermore, they are often involved in the development of tropical cyclones (Avila and Guiney, 2000, Avila et al., 2003, Landsea et al., 1998, Pasch et al., 2009, Thorncroft and Hodges, 2001). Recently, TD-like waves have been found to contribute to the tropical general circulation by transporting moisture from the edges of the equatorial trough to northern latitudes (Adames Corraliza and Mayta, 2024, Mayta and Adames Corraliza, 2024).

Given the myriad of impacts PEWs have, research efforts over past decades have sought to better understand how circulation and convection couple in these transients (Berry and Thorncroft, 2012, Cheng et al., 2019, Duvel, 1990, Fink and Reiner, 2003, Janiga and Thorncroft, 2013, Kiladis et al., 2006, Reed et al., 1977, Rydbeck and Maloney, 2015, Wolding et al., 2020). Wolding et al. (2020) found that convection in PEWs is largely the result of large-scale moisture fluctuations. Similarly, Rydbeck and Maloney (2015) found that horizontal moisture advection explains the evolution of column water vapor and rainfall in PEWs. Recently, Vargas Martes et al. (2023) showed that moisture variations dominate the PEW-related buoyancy and convection, consistent with the notion that the systems are moisture modes (Mayta and Adames, 2023, Mayta and Adames Corraliza,

2024, Vargas Martes et al., 2023, Wolding et al., 2020). Moisture modes are slowly evolving systems whose thermodynamics and growth are driven by moisture fluctuations (Adames, 2022, Adames and Maloney, 2021, Adames Corraliza and Mayta, 2024, Ahmed et al., 2021, Mayta and Adames, 2023, Mayta et al., 2022, Mayta and Adames Corraliza, 2024, Neelin and Yu, 1994, Raymond and Fuchs, 2009, Yu and Neelin, 1994). In moisture modes that resemble PEWs, the mean meridional moisture gradient has been posited to be particularly important for their propagation and growth (Adames Corraliza and Mayta, 2024, Sobel et al., 2001).

While significant progress has been made in understanding the structure of EWs and the processes leading to its evolution over the east Pacific Ocean, west Africa, and the east Atlantic Ocean, less work has been done in examining their representation in global climate models (GCMs) (Daloz et al., 2012, Ruti and Dell' Aquila, 2010, Skinner and Diffenbaugh, 2013). Several studies have sought to better understand EW variability under a warming climate by looking at present and future projections of the Coupled Model Intercomparison Project (CMIP) models (e.g., Camargo, 2013, Martin and Thorncroft, 2015, Skinner and Diffenbaugh, 2013, 2014, Tory et al., 2020). However, these studies have focused on African EWs (AEWs), which have been found to exhibit distinct thermodynamic structures when compared to PEWs (Vargas Martes et al., 2023, Wolding et al., 2020). These studies found significant biases in the representation of AEWs such as their convective coupling mechanism and propagation characteristics over coastal regions (Camargo, 2013, Martin and Thorncroft, 2015, Skinner and Diffenbaugh, 2013). Martin and

Thorncroft (2015) suggested that the poor representation of EWs in GCMs is possibly due to insufficient sensitivity of convection to tropospheric moisture.

With mounting evidence of the importance of moisture in the organization and evolution of EW-related convection (Huaman et al., 2021, Mayta and Adames Corraliza, 2024, Rydbeck and Maloney, 2015, Vargas Martes et al., 2023, Wolding et al., 2020), and with few studies focusing on the East Pacific, an evaluation of model representation of PEWs is necessary. The main objective of this study is to assess the CMIP6 model representation of PEWs by answering the following questions:

Q1: Are CMIP6 models able to reproduce PEWs?

Q2: What are the differences in the governing PEW thermodynamics and mean state between models with realistic and unrealistically weak skill?

This study is structured as follows. Section 3.2 discusses the data and statistical techniques implemented. Section 3.3 outlines the employed model assessment. Section 3.4 presents the results of the study. Finally, the summary and concluding remarks are presented in section 3.5.

## 3.2 Data and Methods

### 3.2.1 Data

We incorporate data from the Fifth Reanalysis from the European Centre for Medium-Range Weather Forecasts (ECMWF) (ERA5; Hersbach et al., 2020). The data spans from 1980-2014 for the July-September (JAS) season. The data is analyzed at single and pressure levels from 1000-100 hPa. The horizontal extent of the east Pacific Ocean domain covers 150°W-75°W and 10°S–30°N. The variables of interest in this study are specific humidity ($q$), geopotential height ($z$), mean total precipitation rate ($P$), outgoing long-wave radiation (OLR), and horizontal winds ($\mathbf{v}$). Finally, as seen in Table 3.1, data from 25 CMIP6 models with daily output will be employed. Additional model information can be seen in Table S1. Model data was regridded to a 2.5° × 2.5° horizontal resolution to attain a uniform grid that matched ERA5 output. Further model and experiment description can be found in the Program for Climate Model Diagnosis & Intercomparison webpage (2022) and Eyring et al. (2016).

### 3.2.2 Methods

Anomalies in the model and reanalysis fields were obtained by removing the annual mean of the data and applying a 2-10 day Lanczos filter (Duchon, 1979), these fields are denoted by a prime ($'$). The data is evaluated over the JAS season when PEW activity is strongest (e.g., Cheng et al., 2019, Rydbeck and Maloney, 2014, 2015, Wolding et al., 2020). The seasonal climatology of the variables were determined by averaging across JAS and are

denoted as variables with an overbar ($\bar{\cdot}$). Mass-weighted vertically-integrated variables from 1000 to 100 hPa are denoted by angle brackets ($\langle\cdot\rangle$). An EOF analysis is employed on the OLR$'$ field over the region of maximum wave activity (5°–20°N and 125°–90°W) following Vargas Martes et al. (2023). Over the east Pacific Ocean the leading structures are a statistically significant pair at the 95% confidence level following North et al. (1982) criterion, with explained variances of 5.4% for EOF1 and 4.9% for EOF2 in ERA5.

Following Vargas Martes et al. (2023), the leading EW structure is attained by linearly regressing the leading principal component (PC) to the fields of interest following Eq. (1) in Adames and Wallace (2014):

$$\mathbf{D} = \mathbf{S}\hat{\mathbf{P}}^T/N, \tag{3.1}$$

where $\mathbf{D}$ is the regression, $\mathbf{S}$ is the field variable, $\hat{\mathbf{P}}$ is the PC time series, and $N$ is the length of the PC. A two-sided t-test was employed to evaluate the statistical significance of the regressions (Kiladis et al., 2009). The contours and shading of the figures shown here are statistically significant at the 95% confidence interval.

Projection of the model OLR field onto the leading reanalysis EOF is performed to examine PEW structure in CMIP6 models following:

$$\hat{\mathbf{P}}_\mathbf{m} = \frac{\left(\mathbf{V}^T\mathbf{OL}\hat{\mathbf{R}}_\mathbf{m}\right)^T - \mu}{\sigma}, \tag{3.2}$$

where $\hat{\mathbf{P}}_\mathbf{m}$ is the standardized CMIP6 model projected PC time series, $\mathbf{V}$ is the reanalysis singular value matrix, $\mathbf{OL}\hat{\mathbf{R}}_\mathbf{m}$ is the model OLR, and $\mu$ and $\sigma$ are the mean and standard

deviation of $\left(\mathbf{V}^T\mathbf{OL}\hat{\mathbf{R}}_\mathbf{m}\right)^T$. The leading PCs are used to obtain the EW-like fields in each model following Eq. 3.1. EOF projections are often employed to ensure that the modes of variability from the model are physically meaningful (Henderson et al., 2017, Waliser and coauthors, 2009). A direct comparison between models and reanalysis is obtained even in models that cannot reproduce EWs but have variability in the same timescale (Henderson et al., 2017, Waliser and coauthors, 2009). In this case, only the models that reproduce a realistic spatiotemporal evolution of PEWs will yield realistic projected PC timeseries.

Time-longitude diagrams of $P'$ are used to determine the model skill in reproducing the evolution of PEWs. As in Vargas Martes et al. (2023), we construct the diagrams via a lag-regression analysis (e.g, Adames and Kim, 2016, Adames and Ming, 2018). The diagrams are obtained by regressing $OLR'$ at lag-0 onto $P'$ as a function of time-lag (from -10 to 10 days) and then meridionally averaging from, 5°N to 20°N.

## 3.3 CMIP6 Model Assessment

Assessment of CMIP6 model skill is performed on the basis of pattern correlations of lag-regressed $P'$ in reanalysis and model data. Previous work by Vargas Martes et al. (2023), showed that the horizontal structure of the leading $P'$ mode in ERA5 and the Tropical Rainfall Measuring Mission/Global Precipitation Measurement Mission (TRMM/GPM) satellite observations (1998-2014) are consistent. In addition, Wolding et al. (2020) observed similar characteristics when comparing the convective life cycles in both ERA5 and

TRMM/GPM satellite observations. Thus, we choose to incorporate ERA5 data given its more extensive temporal availability. Two metrics are used in the model evaluation: (1) the standard deviation of each of the model and reanalysis lag-regressed $P$ standardized by the ERA5 value ($\sigma_r$), and (2) the Pearson's correlation coefficient ($r$) between model and reanalysis fields. These are shown in Table 3.1. The $\sigma_r$ serves to assess model skill at reproducing the reference wave amplitude, while $r$ provides information on the spatial coherence between the model and reanalysis datasets. To assess the realistic representation of PEWs, models are categorized as follows:

1. Good: Models that reproduce realistic PEWs ($r \geq 0.8$ and $0.8 \leq \sigma_r \leq 1.2$).

2. Unrealistically Weak: Models that fail at reproducing a realistic structure and exhibit a weak wave amplitude ($r \leq 0.7$ and $\sigma_r \leq 0.7$).

Good models should explain more than 64% of the total variance, and have an amplitude that is within 20% of the reanalysis value when rounded to the first decimal. Whereas, unrealistically weak models should explain less than 50% of the total variance and 70% of the reanalysis amplitude. A large spread in model representation of PEWs is observed in the Taylor diagram (Copin, 2021, Taylor, 2001) in Fig. 3.1. The thresholds chosen are based on the strongest and weakest models seen in in Fig. 3.1. Over the east Pacific Ocean models exhibit good-to-poor skill in capturing the realistic structure and evolution of PEWs. To reduce model bias (i.e., ensemble mean dominated by simulations that are too similar, e.g., Lin et al., 2024a), only models from different modeling institutions

were further chosen for a multi-model ensemble based on a more rigorous threshold for the good (r≥0.80 and 0.95≤ $\sigma_r$ ≤1.05) and unrealistically weak (r≤0.71 and $\sigma_r$ ≤0.71) models. According to the criteria outlined above, the following three models categorized as good were chosen for a multi-model ensemble: ACCESS-CM2, CESM2-WACCM, and CNRM-CM6-1-HR. While the following models categorized as unrealistically weak were chosen for a multi-model ensemble: FGOALS-g3, INM-CM4-8, and IPSL-CM6A-LR. A full list of models with good PEW representation is shown in Table 3.1.

The leading PEW $P'$ structure and evolution for reanalysis, good, and unrealistically weak model ensembles are shown in the time-longitude diagram in Fig. 3.2. Good models are able to robustly capture the amplitude and spatiotemporal evolution of PEWs, whereas unrealistically weak models exhibit a weak wave signal.

## 3.4 Results

### 3.4.1 Thermodynamic Mean State

The seasonal climatology of the field variables is shown in Fig. 3.3 and is overlaid with the root-mean-squared amplitude of $P'$ regressed onto the PC1 and PC2 of PEW activity (i.e., $P'_{\text{rms}} = \sqrt{P'(PC1)^2 + P'(PC2)^2}$). The horizontal distribution of $\overline{P}$ (Fig. 3.3.a-d) reveals that good models exhibit more coastal $\overline{P}$ than unrealistically weak models especially over the Panama Bight and the southern portion of Central America. The $P'_{\text{rms}}$ distribution in good models is collocated with these regions of enhanced coastal $\overline{P}$. Good

TABLE 3.1: Relative standard deviation ($\sigma_r$) between ERA5 and CMIP6 models $P'$, as well as the correlation coefficient ($r$) of the relationship between both fields. The relationships are determined over the region of strongest PEW activity, 125°W-90°W and 5°N-20°N. Crosses (†) and asterisks (*) denote the models used for the good and unrealistically weak model ensembles respectively. The models with realistic representation of PEWs, are presented in bold for emphasis.

| CMIP6 Model | $\sigma_r$ | $r$ |
|---|---|---|
| **ACCESS-CM2**† | **1.02** | **0.81** |
| AWI-ESM-1-1-LR | 1.13 | 0.69 |
| BCC-ESM1 | 1.58 | 0.66 |
| CanESM5 | 0.74 | 0.68 |
| **CESM2-FV2** | **1.06** | **0.83** |
| **CESM2** | **0.88** | **0.85** |
| **CESM2-WACCM-FV2** | **0.93** | **0.82** |
| **CESM2-WACCM**† | **1.04** | **0.83** |
| **CNRM-CM6-1-HR**† | **0.95** | **0.82** |
| CNRM-CM6-1 | 1.30 | 0.70 |
| CNRM-ESM2-1 | 1.37 | 0.75 |
| **EC-Earth3** | **0.80** | **0.80** |
| FGOALS-g3* | 0.55 | 0.62 |
| GFDL-CM4 | 1.31 | 0.85 |
| IITM-ESM1 | 1.12 | 0.64 |
| INM-CM4-8* | 0.62 | 0.71 |
| INM-CM5-0 | 0.77 | 0.68 |
| IPSL-CM6A-LR-INCA | 0.74 | 0.51 |
| IPSL-CM6A-LR* | 0.71 | 0.53 |
| **MIROC6** | **1.20** | **0.79** |
| MPI-ESM-1-2-HAM | 0.88 | 0.71 |
| MPI-ESM1-2-HR | 1.23 | 0.70 |
| MPI-ESM1-2-LR | 0.98 | 0.69 |
| MRI-ESM2-0 | 0.72 | 0.82 |
| TaiESM1 | 0.71 | 0.81 |

models also exhibit more $\overline{P}$ over the east side of the domain while unrealistically weak models exhibit more oceanic precipitation over the west side.

The distribution of $L_v\langle\overline{q}\rangle$ (Fig. 3.3.e-h) indicates that both the good and unrealistically

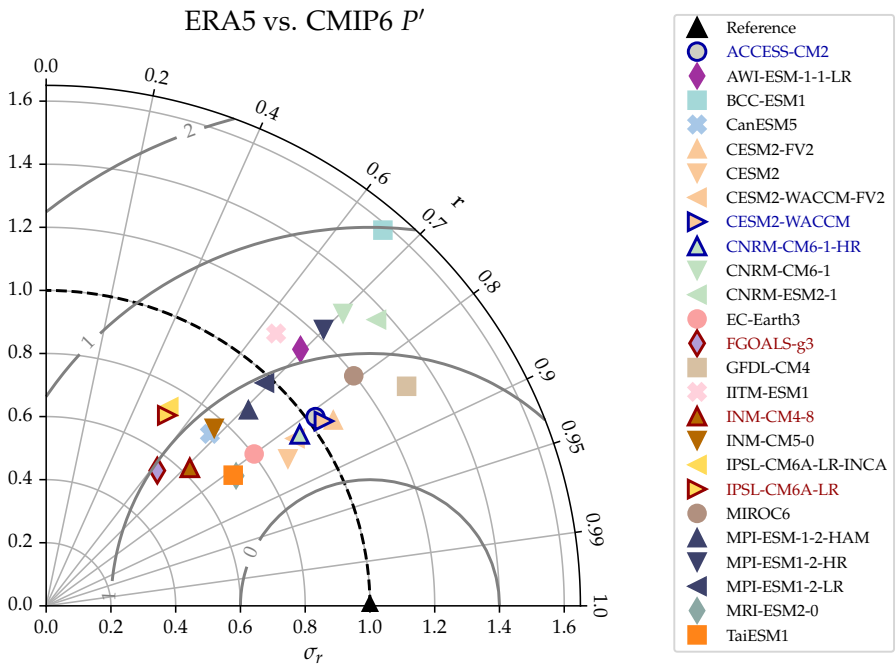


FIGURE 3.1: Taylor diagram of the relative standard deviation ($\sigma_r$) of the lag-regressed precipitation ($P'$) from reanalysis and model dataset (radial axis) and the Pearson correlation coefficient ($r$) between the reanalysis and model fields (angle axis). $P'$ is obtained from a lag-regression analysis of the anomalous field onto the first principal component (PC1) of the outgoing longwave radiation (OLR$'$). The dark grey lines denote the centered root mean squared difference from the ERA5 reference value (black triangle). The dashed black line indicates the reference $\sigma_r$ value. Models that fall to the left of the dashed black line underestimate the wave amplitude, while models that fall to the right produce stronger waves. The closer the models are to the reference value, the more realistic the simulation. Models from the same modeling center have the same color and are denoted by triangle markers (up, down, right or left). Models with realistic and unrealistically weak PEW representation are denoted with blue and maroon borders respectively. Analysis is carried over the region of strongest PEW activity, 5°–20°N, 125°–90°W.

weak CMIP6 ensembles produce a more humid mean state than reanalysis. This overestimation is larger in unrealistically weak models, with high $L_v\langle\overline{q}\rangle$ values observed across the domain. Good models exhibit maximum $L_v\langle\overline{q}\rangle$ value across coastal regions and the eastern portion of the domain, similar to the $\overline{P}$ pattern. While the maximum in unrealistically weak models extends to the western portion of the domain and is centered around

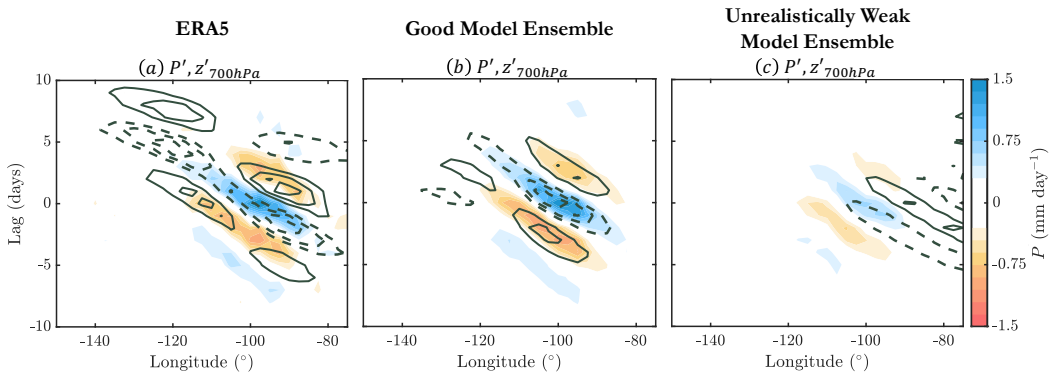


FIGURE 3.2: Time-longitude diagram of PEW ERA5 (left), good and unrealistically weak model ensemble (center and right respectively) seasonal (JAS) $P'$ (shaded contours) averaged over the 5°− 20°N latitude belt. Solid and dashed contours denote positive and negative $z'_{700hPa}$ contours respectively. The contour interval is 0.35 m starting at 0.5 m.

10°N. When comparing the horizontal distribution of $L_v\langle\overline{q}\rangle$ to that of $P'_{\text{rms}}$ we see that PEWs propagate slightly northward of maximum $L_v\langle\overline{q}\rangle$ values, where the meridional gradient ($\partial_y L_v\langle\overline{q}\rangle$) is strongest. This favors a southeast-to-northwest propagation of waves in the good model ensemble, akin to that seen for ERA5 over the east Pacific Ocean, while unrealistically weak models which favor a east-to-west evolution.

Further mean state thermodynamic analysis reveals that temperature exhibits a homogeneous distribution across the domain and the moist static energy shows a similar distribution to the latent energy (not shown).

### 3.4.2 PEW Horizontal Structure

To gain a better understanding of how PEWs are simulated in GCMs, Figure 3.4 shows the $P'$ and $L_v\langle q\rangle'$ as shaded contours, along with $z'_{700hPa}$ as solid and dashed contours and $\mathbf{v}'_{700hPa}$ as wind vectors, regressed onto the leading PC of PEW structure.

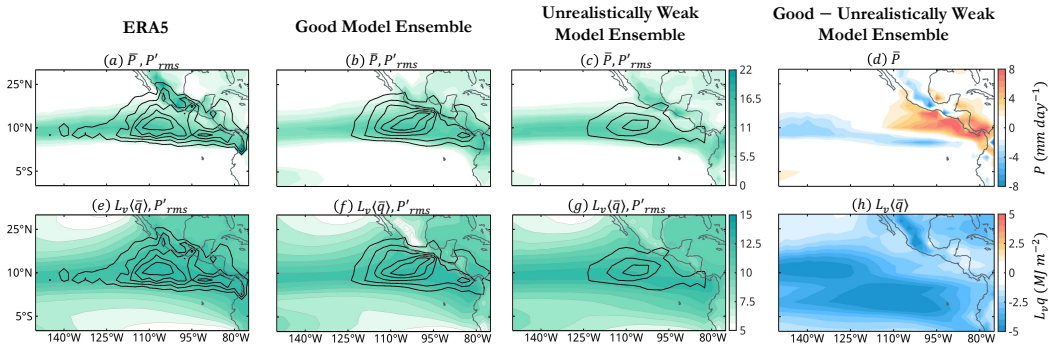


FIGURE 3.3: East Pacific Ocean maps of $\overline{P}$ (first row) and column integrated (1000-100 hPa) $L_v\langle\overline{q}\rangle$ (second row), averaged over the months of JAS for ERA5 (first column), good model ensemble (second column), unrealistically weak model ensemble (third column), and good minus unrealistically weak ensemble difference (fourth column) shown as the shadded contours. $P'_{\text{rms}}$ is overlaid as solid contours.

The wave structure in Fig. 3.4.a-c, shows that in both reanalysis and model ensembles the convective and circulation centers are partially collocated, in agreement with previous studies (e.g., Mayta and Adames Corraliza, 2024, Vargas Martes et al., 2023). Additionally, Figure 3.4 shows that good models reproduce stronger $\mathbf{v}'_{700hPa}$ and $z'_{700hPa}$ over the east Pacific whereas unrealistically poor models produce stronger signals over the Caribbean. While both the good and unrealistically weak model ensembles are able to reproduce the observed $L_v\langle q\rangle'$ as shown in Fig. 3.4.d-f, unrealistically weak models do not reproduce the ERA5 $P'$ (Fig. 3.4.a). This could imply insufficient sensitivity of $P'$ to $\langle q\rangle'$ in the weak models.

### 3.4.3 Diagnostics of physical mechanisms important for PEWs

We now generalize the results of the previous subsection by examining all CMIP6 models in Table 1. Based on previous research and the results of the previous subsection, three diagnostics are chosen for this comparison. (1) A measure of the meridional moisture

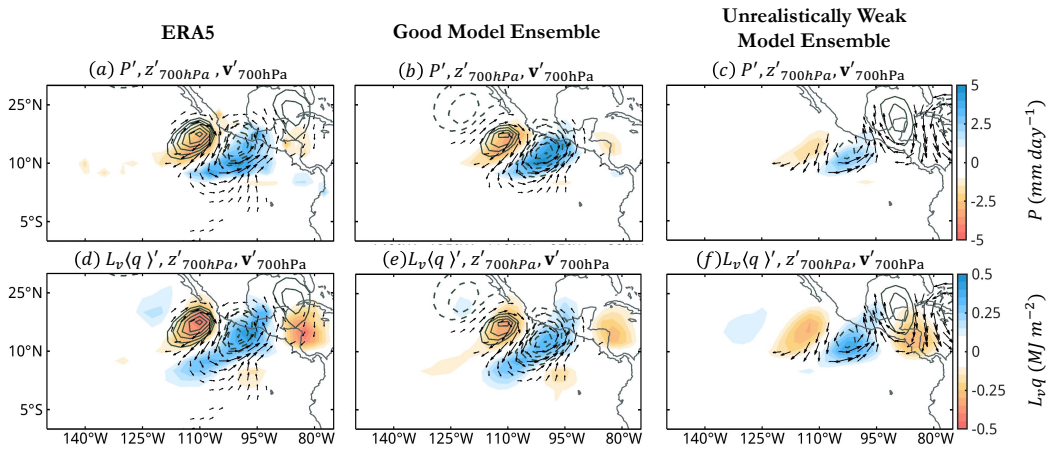


FIGURE 3.4: Horizontal maps of seasonal (JAS) PEW $P'$ (first row) and $L_v\langle q\rangle'$ (second row) for ERA5 (first column), good (second column), and unrealistically weak (third column) ensembles. The $z'_{700hPa}$ (solid and dashed contours) and $\mathbf{v}'_{700hPa}$ (arrows) fields are overlaid in each panel.

gradient ($\triangle_y L_v\langle\overline{q}\rangle$ $indx$) is chosen based on work suggesting its importance in PEW growth (Mayta and Adames Corraliza, 2024). (2) A measure of rainfall over the Panama Bight ($\overline{P}_{indx}$) is selected given its importance for the in-situ generation of PEWs (e.g., Rydbeck and Maloney, 2014, Rydbeck et al., 2017, Serra et al., 2008). (3) Lastly, the results of Fig. 3.4 indicate that the convective moisture adjustment timescale ($\tau_c'$) is important for the representation of moisture modes, as seen by previous studies (e.g., Jiang et al., 2016). We determine the strength of $\triangle_y L_v\langle\overline{q}\rangle$ $indx$ by averaging $L_v\langle\overline{q}\rangle$ over the region of maximum (100°W-95°W and 5°N-10°N) and minimum (100°W-95°W and 25°N-30°N) values, and then calculate their difference. Similarly, we constructed $\overline{P}_{indx}$ by averaging $\overline{P}$ over the Panama Bight region (85°-75°W and 0°-10°N). Finally, $\tau_c'$ is given as the slope of the relationship between PEW $\langle q\rangle'$ and $P'$, $\tau_c' \equiv \frac{\langle q\rangle'}{P'}$. The relationships presented in Fig. 3.5 are all significant at a 95% confidence level.

Figure 3.5.a shows that the models with the largest (smallest) PEW amplitude exhibit the smallest (largest) $\triangle_y L_v \langle \overline{q} \rangle$ *indx* values. Further examination of Fig. 3.3.e-h reveals that this relationship holds in the model ensembles, with good (unrealistically weak) models exhibiting weaker (stronger) $\triangle_y L_v \langle \overline{q} \rangle$ *indx* values. In addition, Fig. 3.5.b shows that models with stronger (weaker) amplitudes exhibit smaller (larger) values of $\tau_c'$. Models with realistic PEW representation have $\tau_c'$ values that are close to those of ERA5 ($\tau_c' \approx 8.9$ hours). Finally, the results shown in Fig. 3.5.c indicate that models with strong (weak) PEW amplitude exhibit higher (lower) $\overline{P}$ over the Panama Bight, which supports the results that suggest that the region is important for PEW development (e.g., Rydbeck and Maloney, 2014, Rydbeck et al., 2017, Serra et al., 2008). While the relationships shown in Fig. 3.5.a-c (a: $r = -0.48$, b: $r = -0.53$, and c: $r = 0.45$) do not fully explain the spread in model representation of PEWs seen in Fig. 3.1, they aid in our understanding of core processes related to PEW evolution and how these are represented in the CMIP6 models. More specifically, the good and unrealistically weak models do not fall close to each other in the panels in Fig. 3.4.3. This result indicates that while the models selected for the good model ensemble reproduce realistic PEW-related $P'$, they struggle at consistently reproducing some of the key physical processes important for PEW development (e.g., Rydbeck and Maloney, 2014, Rydbeck et al., 2017, Serra et al., 2008, Vargas Martes et al., 2023.

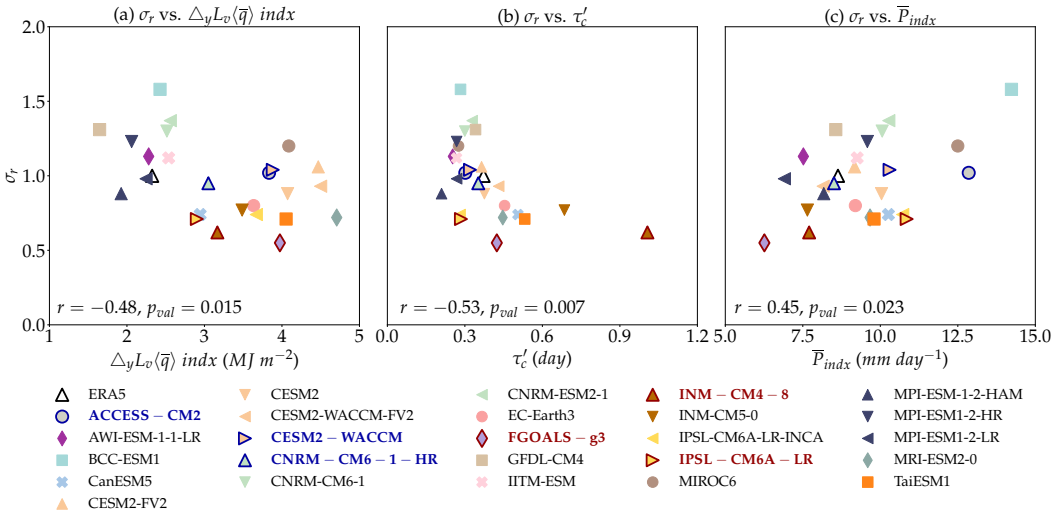


FIGURE 3.5: Significant relationships in the representation of PEWs. The relationship between (a) $\sigma_r$ and latent energy gradient index ($\triangle_y L_v \langle \overline{q} \rangle$ *indx*), (b) $\sigma_r$ and the moist convective adjustment timescale ($\tau_c'$), and (c) $\sigma_r$ and a $P'$ index over the Panama Bight ($P'_{\text{indx}}$) are all significant at the 95% confidence level.

## 3.5 Summary and Conclusions

In this study we assess the representation of PEWs in 25 CMIP6 models during boreal summer by comparing the spatial coherence and amplitude of $P'$ in models versus reanalysis. At the beginning of this study we posed two research questions. Q1: Are CMIP6 models able to reproduce PEWs? Q2: What are the differences in the governing thermodynamics and mean state between models with high and low skill? Our results reveal a large spread in PEW representation over the east Pacific Ocean. The ensemble results and the PEW representation diagnostics reveal three findings that help us answer Q2.

First, models with stronger (weaker) $P'$ signals exhibited weaker (stronger) humidity gradients. This finding appears counterintuitive at first, but is consistent with recent work by Adames Corraliza and Mayta (2024). They proposed that wave activity ($\mathcal{A}$) and

the strength of the mean meridional moisture gradient obey the following conservation equation in the absence of major moisture sources and sinks:

$$\frac{\partial}{\partial t}(\mathrm{ALE} + \mathcal{A}) = 0. \tag{3.3}$$

where ALE is the "available latent energy", a measure of the mean moisture gradient. Under this lens, models with higher PEW activity should exhibit weaker moisture gradients, in agreement with our results. This theory is based on the assumption that the waves are moisture modes. Hence, that PEWs follow this relationship can be interpreted as further evidence that these waves are moisture modes that extract energy from the mean moisture gradient, in agreement with previous work (Mayta and Adames Corraliza, 2024, Vargas Martes et al., 2023, Wolding et al., 2020). Although it does directly explain why the good models simulate more realistic PEWs, it hints at the possibility that the good models are better able to simulate moisture mode behavior.

The second finding related to Q2 is that waves with stronger (weaker) $P'$ amplitude exhibit smaller (larger) values of $\tau_c'$. Thus, good models exhibit a higher rainfall sensitivity to moisture than poor models. This is a result that was first found to be related to a model's ability to simulate a strong MJO (Jiang et al., 2016, Lin et al., 2024a). The sensitivity of MJO simulation to convection sensitivity to moisture fluctuations was a key prediction of moisture mode theory (Adames and Kim, 2016, Raymond, 2001, Sobel and Maloney, 2013). That it applies to PEWs as well indicates that the theory applies to these waves as well, consistent with the findings of Fig. 5a. It is worth noting that several of the models

that simulate the weakest PEWs also simulate weak MJOs according to the results of Lin et al. (2024a), suggesting that there is some overlap between the ability of models to simulate both. Future work should further examine this possibility.

The third finding related to Q2 is that models with stronger (weaker) $P'$ signal also exhibit a stronger (weaker) amount of rainfall over the Panama Bight. This result aligns with the ensembles which show that good models favor wave signals over the east Pacific, whereas unrealistically weak models favor incoming signals from the Caribbean (i.e, AEWs). On its own, this finding highlights the importance of local forcing mechanisms in order to realistically simulate PEWs. This result also agrees with studies that identified the Panama Bight region as playing a significant role in the in-situ development of PEWs (e.g., Rydbeck and Maloney, 2014, Rydbeck et al., 2017, Serra et al., 2008, Torres and Thorncroft, 2022, Torres et al., 2021).

Individually, none of the results explain the majority of the variance (25% at most), but together they elucidate the core processes of PEWs. It shows that a realistic representation of moisture-convection coupling is critical to realistically simulate PEWs. Second, how precipitation is locally distributed (e.g. land vs sea contrasts) may also be important. Future examination should examine these relations in further detail. In particular, how PEW representation is connected to the MJO and other tropical weather systems could provide further insights onto the core mechanisms of all these systems. Additionally, the models that reproduce the most realistic PEWs can be employed to understand how the systems will respond to a warming climate.

# Chapter 4

# African Easterly Wave Representation in CMIP6 Models

**Key Points**

- Twenty-five CMIP6 models are assessed based on their representation of African Easterly waves.
- Models with unrealistically strong AEWs exhibit strong mean state precipitation over the continent, stronger AEW-related thermodynamic fields, smaller moist convective adjustment timescales, and weaker mean state thermodynamic gradients.
- Both east Pacific and African Easterly Wave growth is more consistent with moisture-vortex instability than baroclinic instability.

## 4.1 Introduction

African Easterly Waves (AEWs) are alternating regions of high and low pressure that propagate westward and are coupled to convection (e.g., Kiladis et al., 2009, Lau and Lau, 1990, 1992). They originate over West Africa, and the initial stages of their evolution occur over the continent, making them unique among their oceanic counterparts (i.e. EWs over the Indian, West Pacific, East Pacific, and Atlantic Ocean and the Caribbean Sea). AEWs are arguably one of the most well known tropical depression-type (TD-type) systems (westward wavenumbers 5-20 and periods from 2.5-10 days; e.g., Feng et al., 2020, Kiladis et al., 2009, Mayta and Adames Corraliza, 2024). They play an important role in the hydrological cycle of Subsaharan Africa (Kiladis et al., 2009) and serve as main seeds for Atlantic Hurricanes (e.g., Erickson, 1963, Frank, 1970).

Given the myriad of impacts AEWs have in the regions over which they evolve, research efforts over past decades have sought to better understand how circulation and convection couple in these transient waves (e.g., Berry and Thorncroft, 2012, Cheng et al., 2019, Duvel, 1990, Fink and Reiner, 2003, Janiga and Thorncroft, 2013, Kiladis et al., 2006, Reed et al., 1977, Rydbeck and Maloney, 2015, Wolding et al., 2020). Wolding et al. (2020) found that dry adiabatic motions govern convective coupling of AEWs. While, Vargas Martes et al., 2023 showed that moisture and temperature fluctuations play comparable roles in AEW-associated convection.

While research efforts have posited that AEWs grow from a combination of baroclinic and

barotropic instability (e.g., Hsieh and Cook, 2008, Thorncroft and Hoskins, 1994a), recent studies have shown that moist processes are important for the convective coupling and thermodynamic evolution of AEWs (e.g., Núñez Ocasio and Rios-Berrios, 2023, Russell and Aiyyer, 2020, Russell et al., 2020, Vargas Martes et al., 2023, Wolding et al., 2020). For instance, Thorncroft and Hoskins (1994a) find that AEWs arise from barotropic and baroclinic instabilities, and that the inclusion of diabatic heating in their linear model reinforces baroclinic energy conversions. Similarly, Hsieh and Cook (2008) find that barotropic and baroclinic conversions of the African easterly jet aid in the maintenance of AEWs. Conversely, AEWs undergoing tropical cyclogenesis have been found to evolve over regions of strong meridional humidity gradients (Mayta et al., 2024). In addition Russell et al. (2020) show that low-level potential vorticity generated by moist convection aids in the maintenance of upright AEW-associated circulation (i.e., upright PV vertical structure against the background shear). Similarly, Russell and Aiyyer (2020) posit that convective coupling in AEWs aids in the enhancement of the wave's low-level circulation.

Unlike their EW counterparts over the east Pacific (PEWs), discussed in Chapter 3, several studies have sought to better understand how AEWs will respond to a warming climate by examining present and future projections of the Coupled Model Intercomparison Project (CMIP) models (e.g., Camargo, 2013, Martin and Thorncroft, 2015, Skinner and Diffenbaugh, 2013, 2014, Tory et al., 2020). As discussed in Chapter 3, these studies found that the representation of AEWs in models exhibited significant biases, such as their propagation characteristics over coastal regions and convective coupling mechanism (Camargo, 2013, Martin and Thorncroft, 2015, Skinner and Diffenbaugh, 2013). It

is suggested that insufficient sensitivity of convection to tropospheric moisture may be the cause for the poor representation of AEWs in global climate models (GCMs) (Martin and Thorncroft, 2015). Less work has been done, however, in assessing how AEWs are represented in GCMs (Daloz et al., 2012, Ruti and Dell' Aquila, 2010, Skinner and Diffenbaugh, 2013), especially in the scope of phase six of CMIP (CMIP6) models.

As was done in Chapter 3 for PEWs, this chapter focuses on assessing model representation of AEWs by answering the following questions:

Q1: Are CMIP6 models able to reproduce AEWs?

Q2: What are the differences in the thermodynamics and mean state between models with realistic and unrealistically strong waves?

This study is structured as follows. Section 4.2 discusses the data and the implemented statistical techniques. Section 4.3 describes the employed model assessment metrics. Section 4.4 presents the results of the study. Finally, the summary and concluding remarks are presented in section 4.5.

## 4.2 Data and Methods

### 4.2.1 Data

As in Chapter 3, we employ data from the European Centre for Medium-Range Weather Forecasts' (ECMWF) fifth reanalysis (ERA5) (Hersbach et al., 2020) and from 25 CMIP6

models with daily output (see Table 2.3; Eyring et al., 2016). The fields analyzed in this chapter are the outgoing long-wave radiation (OLR), mean total precipitation rate ($P$), 700 hPa geopotential height ($z_{700\text{hPa}}$), 700hPa horizontal winds ($\mathbf{v}_{700\text{hPa}}$), and column average (850-200 hPa) specific humidity ($q_{\text{avg}}$), temperature ($T_{\text{avg}}$) and moist static energy ($m_{\text{avg}} = C_p T_{\text{avg}} + g z_{\text{avg}} + L_v q_{\text{avg}}$). Where $m_{\text{avg}}$ is the sum of dry enthalpy, potential energy, and latent energy and $C_p$, $L_v$, and $g$ are constants denoting the specific heat of air at constant pressure, latent heat of vaporization, and gravitational acceleration, respectively. Data is regridded to a 2.5°×2.5° horizontal resolution to match ERA5's uniform grid. Data is analyzed over the July-September (JAS) season, when AEW activity is highest, and spans from 1980-2014. For further CMIP6 experiment information refer to Eyring et al. (2016).

### 4.2.2 Methods

This chapter closely follows the methods outlined in Chapter 3, Section 3.2. Thus, in this section we only discuss the methods employed for AEW analysis that differ from those presented in the previous chapter. An EOF analysis is employed on the OLR field over the region of maximum wave activity (35°W-20°E and 5°N-20°N), motivated by previous studies (e.g., Cheng et al., 2019, Kiladis et al., 2006, Vargas Martes et al., 2023, 2024). Over West Africa and the East Atlantic region, the explained variance of the leading empirical orthogonal functions (EOFs) is 7.00% for EOF1 and 6.44% for EOF2. This orthogonal pair is significant at the 95% confidence interval following the North et al. (1982) criterion.

## 4.3 CMIP6 Model Assessment

As in Chapter 3, section 3.3, we assess model skill on the basis of pattern correlations between ERA5 and CMIP6 model lagged-$P'$. The same metrics are employed for model evaluation: (1) the Pearson correlation coefficient ($r$) between the reanalysis and model datasets, and (2) the relative standard deviation ($\sigma_r$) of each dataset (standardized by the ERA value). While $r$ provides information of the spatial coherence between the lagged-$P'$ in reanalysis and models, $\sigma_r$ provides information on the relative amplitude of the wave in each dataset. The attained $r$ and $\sigma_r$ values are presented in Table 4.1. To assess the realistic representation of AEWs, models are categorized using the following criteria:

1. Good: Similar to Chapter 3, section 3.3, models that reproduce realistic AEWs ($r \geq 0.8$ and $0.8 \leq \sigma_r \leq 1.2$, rounded to the first decimal). These models should explain over 64% of the observed variance and be within 20% of the observed AEW amplitude.

2. Unrealistically Strong−Strong Correlation (US-SC): Models that fail to reproduce a realistic wave amplitude ($r \geq 0.8$ and $\sigma_r \geq 1.5$, rounded to the first decimal). They should explain over 64% of the observed AEW variance, and overestimate the precipitation anomalies by 50 % or more.

3. Unrealistically Strong−Weak Correlation(US-WC): Models that fail to reproduce a realistic wave amplitude and spatial distribution ($r \leq 0.6$ and $\sigma_r \geq 1.5$, rounded

TABLE 4.1: Relative standard deviation ($\sigma_r$) between ERA5 and CMIP6 models $P'$, as well as the correlation coefficient ($r$) of the relationship between both fields. The relationships are determined over the region of strongest AEW activity, 35°W-20°E and 5°N-20°N. Models chosen for further analysis are identified as good, unrealistically strong-strong correlation, and unrealistically strong-weak correlation and are denoted by crosses (†), asterisks (*), and stars (⋆) respectively. The models with realistic representation of AEWs, are presented in bold for emphasis.

| CMIP6 Model | $\sigma_r$ | $r$ |
|---|---|---|
| ACCESS-CM2 | 0.76 | 0.62 |
| AWI-ESM-1-1-LR | 1.66 | 0.68 |
| BCC-ESM1⋆ | 1.88 | 0.56 |
| CanESM5⋆ | 1.85 | 0.52 |
| CESM2-FV2 | 1.58 | 0.72 |
| CESM2 | 1.36 | 0.65 |
| CESM2-WACCM-FV2 | 1.69 | 0.66 |
| CESM2-WACCM | 1.46 | 0.61 |
| **CNRM-CM6-1-HR**† | 0.99 | 0.83 |
| CNRM-CM6-1 | 1.65 | 0.65 |
| CNRM-ESM2-1 | 1.70 | 0.74 |
| **EC-Earth3** | 0.91 | 0.76 |
| FGOALS-g3 | 0.83 | 0.62 |
| GFDL-CM4* | 2.13 | 0.75 |
| IITM-ESM1 | 1.17 | 0.70 |
| INM-CM4-8 | 0.92 | 0.67 |
| **INM-CM5-0** | 0.97 | 0.75 |
| IPSL-CM6A-LR-INCA | 1.65 | 0.76 |
| IPSL-CM6A-LR | 1.48 | 0.75 |
| MIROC6* | 2.73 | 0.81 |
| MPI-ESM-1-2-HAM | 1.20 | 0.66 |
| **MPI-ESM1-2-HR** | 0.80 | 0.85 |
| MPI-ESM1-2-LR | 1.49 | 0.71 |
| **MRI-ESM2-0** | 0.91 | 0.85 |
| **TaiESM1**† | 1.00 | 0.83 |

to the first decimal). These should explain less than 36% of the observed AEW variance, and overestimate the precipitation anomalies by 50% or more.

We see a large spread in AEW representation in the Taylor Diagram in Figure 4.1. As in the previous chapter, these thresholds are chosen based on the results attained in the Taylor diagram. More specifically, we choose the thresholds and models by focusing on models that stant out based on their overestimation of wave amplitude (US−SC and US−WC models) and the closest models to observations (good models). Unlike the spread we observed for PEW in the previous chapter (see Figure 3.1), most of the models produce AEWs with an amplitude that explains more than 80% of the reanalysis value. The difference in model skill comes predominantly from the overestimation of the wave amplitude and the varying values for spatial coherence. For the good models we consider TaiESM1 and CNRM-CM61-HR ($r > 0.8$ and $\sigma_r = 1.0$), as they explain over 64% of the explained variance and 100% of the observed amplitude. We consider GFDL-CM4 and MIROC6 as US−SC ($r > 0.8$ and $\sigma_r > 2.0$) models, which explain over 64% of the observed variance and produce a wave that is twice as ample as the observed. Similarly, BCC-ESM1 and CanESM5 are chosen from the US−WC ($r < 0.6$ and $\sigma_r \geq 1.9$) models, which explain less than 36% of the total variance and are approximately twice as ample as the observed wave. Models that produce realistic AEWs are presented in Table 4.1. It is worth noting that the only models that successfully reproduce both PEWs and AEWs based on the criteria outlined above and in Chapter 3, section 3.3, are the CNRM-CM6-1-HR and EC-Earth3 models.

The good, US−SC, and US−WC time-longitude diagrams are shown in Figure 4.2. Good models are able to reproduce the observed wave amplitude and spatio-temporal evolution. Whereas, in US−SC and US−WC, both the circulation ($z'_{700hPa}$) and $P'$ are too strong

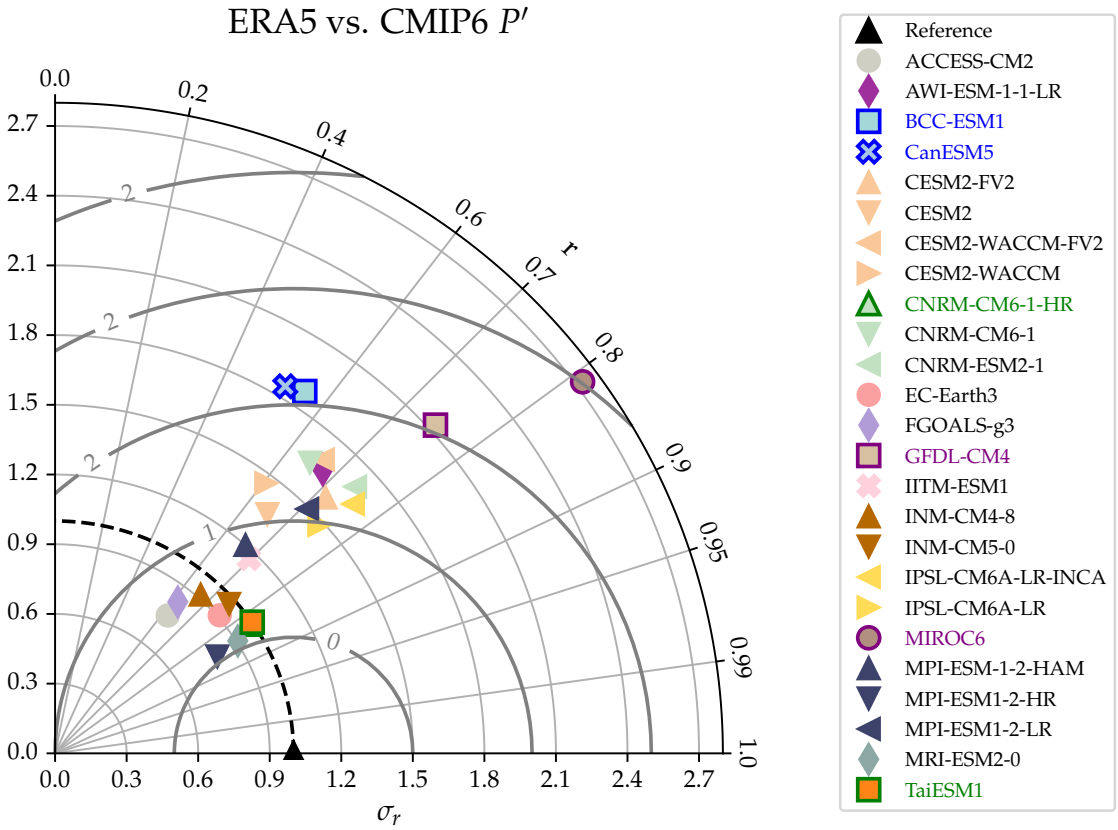


FIGURE 4.1: As in Figure 3.1 but for AEWs. Models with realistic, US−SC, and US−WC AEW representation are denoted with green, purple, and blue borders respectively. Analysis is carried over the region of strongest AEW activity, 5°–20°N, 35°W–20°E.

when compared to reanalysis. In addition, $P'$ and $z'_{700\text{hPa}}$ signals originate further east (i.e., close-to or before 20°E) in most US−SC, and US−WC models. While in US−SC models $P'$ and $z'_{700\text{hPa}}$ are either fully or partially collocated, in US−WC models the field variables are either partially collocated or off-phase across all longitudes. US−WC models also exhibit $P'$ signals at earlier lags when compared to reanalysis, good and US−SC models. We also note that $P'$ signals persist longer in both US−SC and US−WC models than they do in reanalysis.

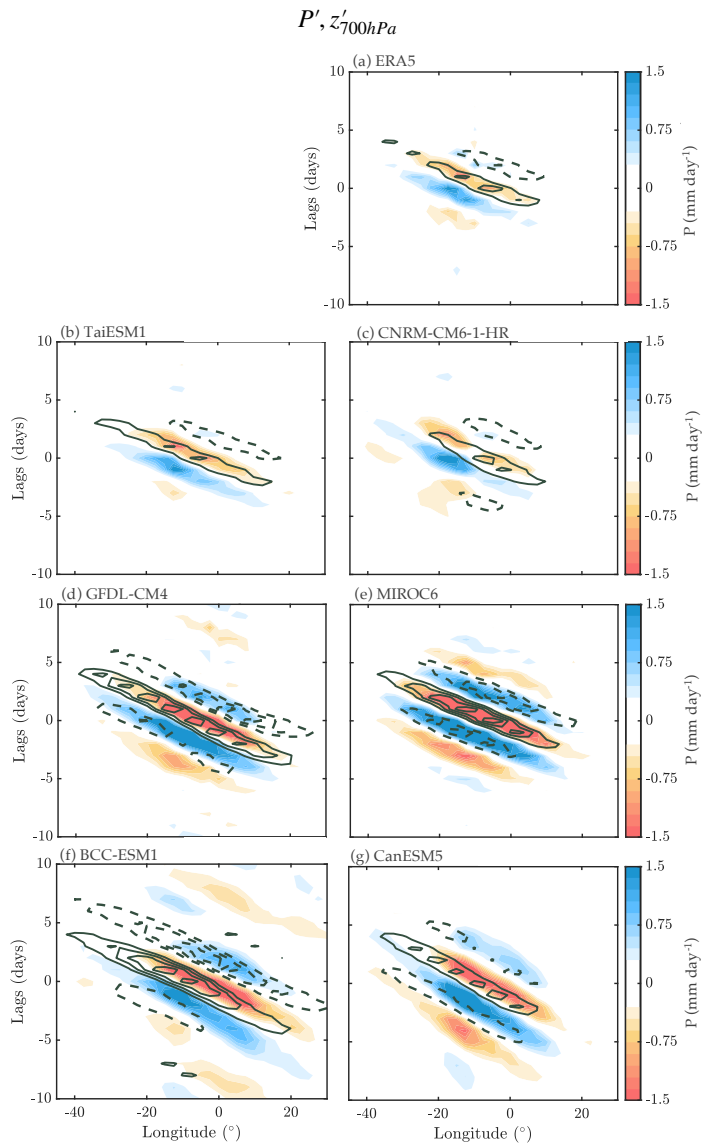


FIGURE 4.2: As in Figure 3.2 but for AEWs in reanalysis (first row), good (second row), US−SC (third row), and US−WC (fourth row).

## 4.4 Results

### 4.4.1 Thermodynamic Mean State

The seasonal mean states of the studied field variables are presented in Figure 4.3. As in Chapter 3, section 3.4.1, we overlay the the root-mean-squared amplitude of $P'$ linearly

regressed onto the PC1 and PC2 of AEW activity ($P'_{\text{rms}} = \sqrt{P'(PC1)^2 + P'(PC2)^2}$) onto $\overline{P}$. The horizontal distribution of $\overline{P}$ in Figure 4.3.a-g shows that while good models are able to reproduce the wave's evolution and are the closest at reproducing the observed $\overline{P}$, most models overestimate the seasonal $\overline{P}$ values, especially over the African Monsoon region. In addition, both US−SC and US−WC models exhibit $P'_{\text{rms}}$ that extend further into the continental and oceanic region when compared to reanalysis and good models. To gain further insight on the land versus oceanic differences between the models and reanalysis, Figure 4.4 shows the horizontal distribution of the differences between ERA5 and the good (a-b), US−SC (c-d), and US−WC (e-f) models. As suggested in Figure 4.3.a-g, US−SC and US−WC models overestimate $\overline{P}$ over the AM, with MIROC6 and CanESM5 also having larger values over oceanic regions and BCC-ESM1 underestimating $\overline{P}$ over the ocean. Good models exhibit close-to or less-than the observed $\overline{P}$ value over the African Monsoon and have a southward shift of the Intertropical Convergence Zone (ITCZ) in both models, with the differences being more prominent in CNRM-CM6-1-HR.

We also examine the horizontal distribution of $L_v\overline{q}_{\text{avg}}$ (Figure 4.3.h-n). We see that good, US−SC, and US−WC overestimate the horizontal distribution of $L_v\overline{q}_{\text{avg}}$ with the closest mean state being reproduced by CNRM-CM6-1-HR. The $L_v\overline{q}_{\text{avg}}$ distribution in US−SC, and US−WC also suggest a weaker meridional gradient in ($\partial_y L_v\overline{q}_{\text{avg}}$) with larger $L_v\overline{q}_{\text{avg}}$ values observed across the domain in the models. As in $\overline{P}$ the overestimation in most models is more prominent over the African Monsoon and over the oceanic region along 10°N.

Similarly, the horizontal distribution of $C_p\overline{T}_{\text{avg}}$ (Figure 4.3.o-u), shows that most models also overestimate $C_p\overline{T}_{\text{avg}}$, with the exception of CNRM-CM6-1-HR and GFDL-CM4 in which the distribution is notably weaker. We note that there is less agreement between simulations in the representation of this field variable.

While the horizontal distribution of $\overline{m}_{\text{avg}}$ (Figure 4.3.v-ab) is modulated by both the latent and dry enthalpy, we see that its overall structure resembles that of $L_v\overline{q}_{\text{avg}}$. It is also seen that most models exhibit larger values over the African Monsoon and the oceanic region along 10°N. As with $C_p\overline{T}_{\text{avg}}$, CNRM-CM6-1-HR and GFDL-CM4 reproduce a $\overline{m}_{\text{avg}}$ that is close-to or less than the observed.

It is worth noting that while some simulations reproduce horizontal distributions that are close to reanalysis $\overline{m}_{\text{avg}}$, none of them exhibit a combination of $\partial_y L_v\overline{q}_{\text{avg}}$ and $\partial_y C_p\overline{T}_{\text{avg}}$ that is close to the observed. Moreover, the simulation that more closely reproduces the observed $L_v\overline{q}_{\text{avg}}$, $C_p\overline{T}_{\text{avg}}$, $L_v\overline{m}_{\text{avg}}$, is GFDL-CM4. Yet, this model simulates AEWs with $P'$ signals that are too strong.

Given the relevance of moist convection in the growth of AEWs over the African-Atlantic region (Berry and Thorncroft, 2012, Russell and Aiyyer, 2020) and its governing thermodynamic structure (Vargas Martes et al., 2023, Wolding et al., 2020), we examine the relationship between $P$ and column saturation fraction CSF ($\langle q\rangle/\langle q_s\rangle$, where $\langle q_s\rangle$ is the column integrated saturated specific humidity) in Figure 4.5 (e.g., Bretherton et al., 2004, Fuchs and Raymond, 2002). Results show that while models simulate distributions of $P$ and CSF that exhibit a slow buildup of CSF and the rapid onset of $P$, the sensitivity

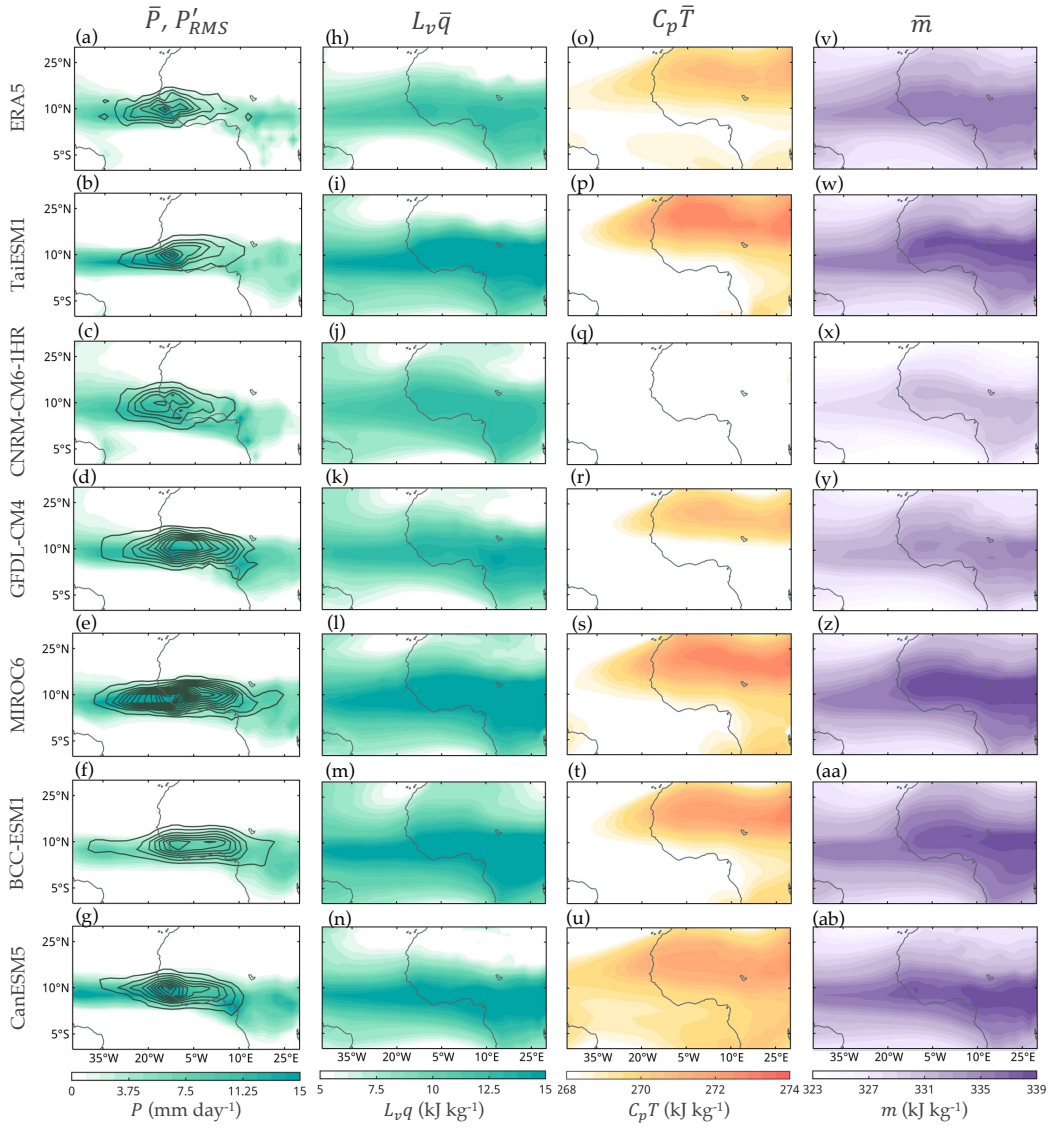


FIGURE 4.3: East Atlantic Ocean and West Africa maps of $\overline{P}$ (first column), $L_v\overline{q}_{\text{avg}}$ (second column), $C_p\overline{T}_{\text{avg}}$ (third column), and $\overline{m}_{\text{avg}}$ (fourth column), averaged over the months of JAS for ERA5 (first row), and good (second and third rows), US−SC (fourth and fifth rows), and US−WC (sixth and seventh rows) models. $P'_{\text{rms}}$ is overlaid as solid contours in the $\overline{P}$ maps (first column).

of $P$ to CSF differs across datasets. The exponential fit of the $P$−CSF distribution is shown as a black line. The steepness of this pickup curve is denoted by the slope. In

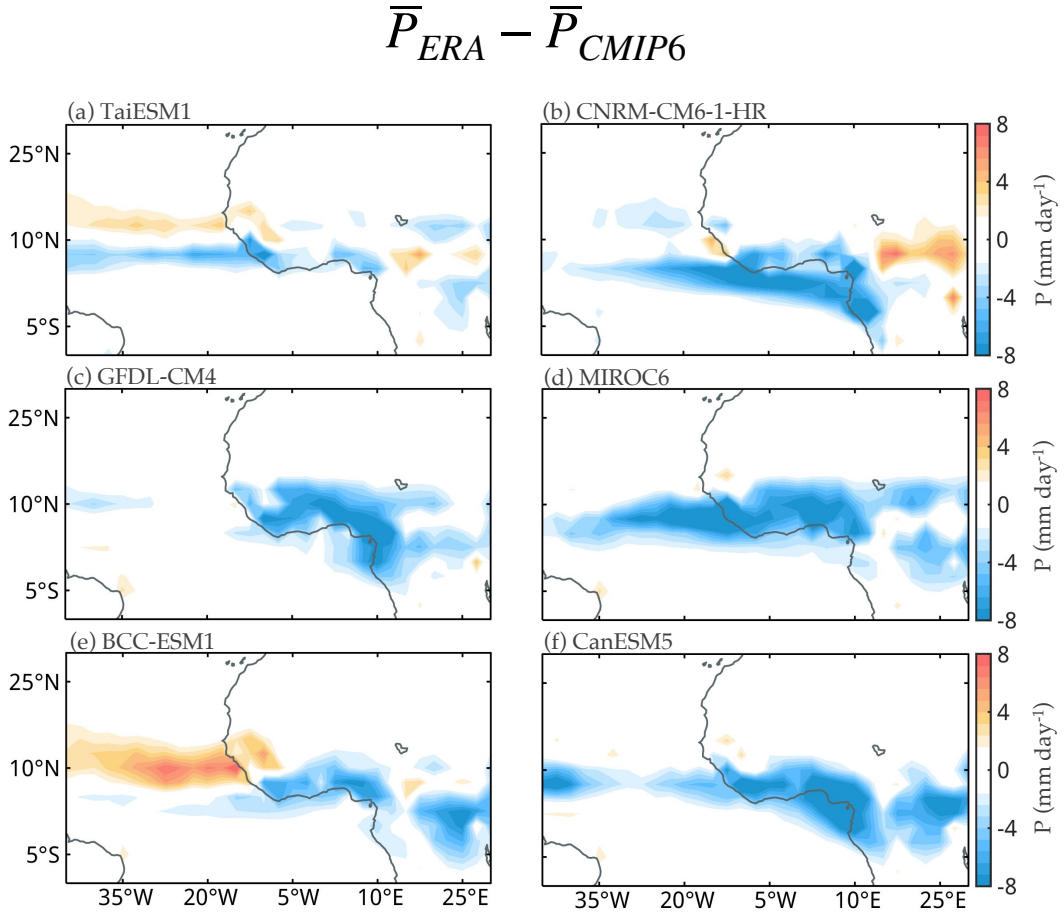


FIGURE 4.4: Differences between ERA5 and good (first row), US−SC (second row), and US−WC (third row) $\overline{P}$ during JAS.

models the slopes vary and fall between 7.65 and 14.77. When we compare these distributions to reanalysis, three things become evident: (1) there is a higher density of points at higher values of $P$ in most models (red shading). (2) The extremes (blue shading) are close to the observed in good models, and higher in most unrealistically strong models. Finally, (3) the steepness of the curve exhibit significant variations across datasets, and is significantly smaller than that of reanalysis. This suggests that in the absence of other processes modulating convection, $P$ in CMIP6 simulations is insufficiently sensitive to CSF.

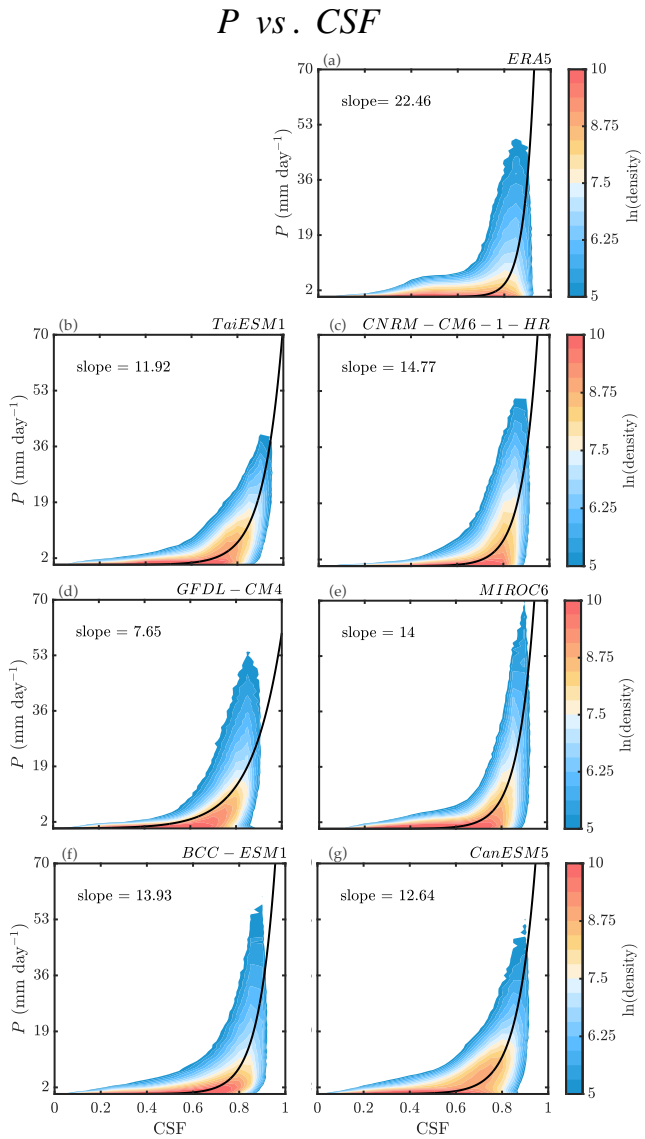


FIGURE 4.5: As in Figure 2.2, but for the distribution of $P$ and CSF in ERA5 (first row), good (second row), US−SC (third row) and US−WC (fourth row), determined over a region of high AEW activity (25°W-0° and 5°-17.5°N), during boreal summer (JAS) during the period of 1980-2014. $P$ values are binned every 1 mm day$^{-1}$, beginning at 0 mm day$^{-1}$. While CSF values are binned every 0.05 units of CSF, beginning at 0 units of CSF.

### 4.4.2 PEW Horizontal Structure

As in Chapter 3, section 3.4.2, to gain further insights on how AEWs are represented in CMIP6 models, in Figure 4.6 we examine the $P'$, $L_v q'_{\text{avg}}$, $C_p T'_{\text{avg}}$, and $m'_{\text{avg}}$ (v-ab). From

the AEW structures in Figure 4.6.a-g, we see that good models are able to reproduce the observed $P'$ and circulation ($z'_{700\text{hPa}}$ and $v'_{700\text{hPa}}$). The suppressed $P'$ is also seen leading the high-pressure over land and lagging the low-pressure over the ocean. US−SC models exhibit stronger $P'$ and circulation signals, with similar phasing between the field variables. On the other hand, in addition to US−WC models exhibiting high values of $P'$ and circulation, enhanced $P'$ lags the low-pressure over both land and ocean.

The wave's horizontal $L_v q'_{\text{avg}}$ structure in Figure 4.6.h-n shows that while good models exhibit the closest values to reanalysis, the horizontal structure in TaiESM1 is closer to reanalysis than CNRM-CM6-1-HR. While both US−SC and US−WC models exhibit signals that are too strong, in the US−WC models, the $L_v q'_{\text{avg}}$ is shifted to the right of the pressure centers when compared to reanalysis. It is worth noting that while some models overestimate the $L_v q'_{\text{avg}}$ values and and others exhibit an eastward shift in the maximum values, the prevailing $L_v q'_{\text{avg}}$ structure is similar across all models. This result aligns with the results presented in the preceding chapter for PEWs.

Whereas, when we examine the $C_p T'_{\text{avg}}$ structure in Figure 4.6.o-u, we see that all models exhibit disagreement between all simulations and with the reanalysis. In both good models, we see stronger extratropical signals over the African continent in CNRM-CM6-1-HR and over the ocean in TaiESM1. These signals are also present in both US−SC models, which also exhibit $C_p T'_{\text{avg}}$ signals along 7°N. In addition to these signals, in US−WC models we see the eastward shift in $C_p T'_{\text{avg}}$.

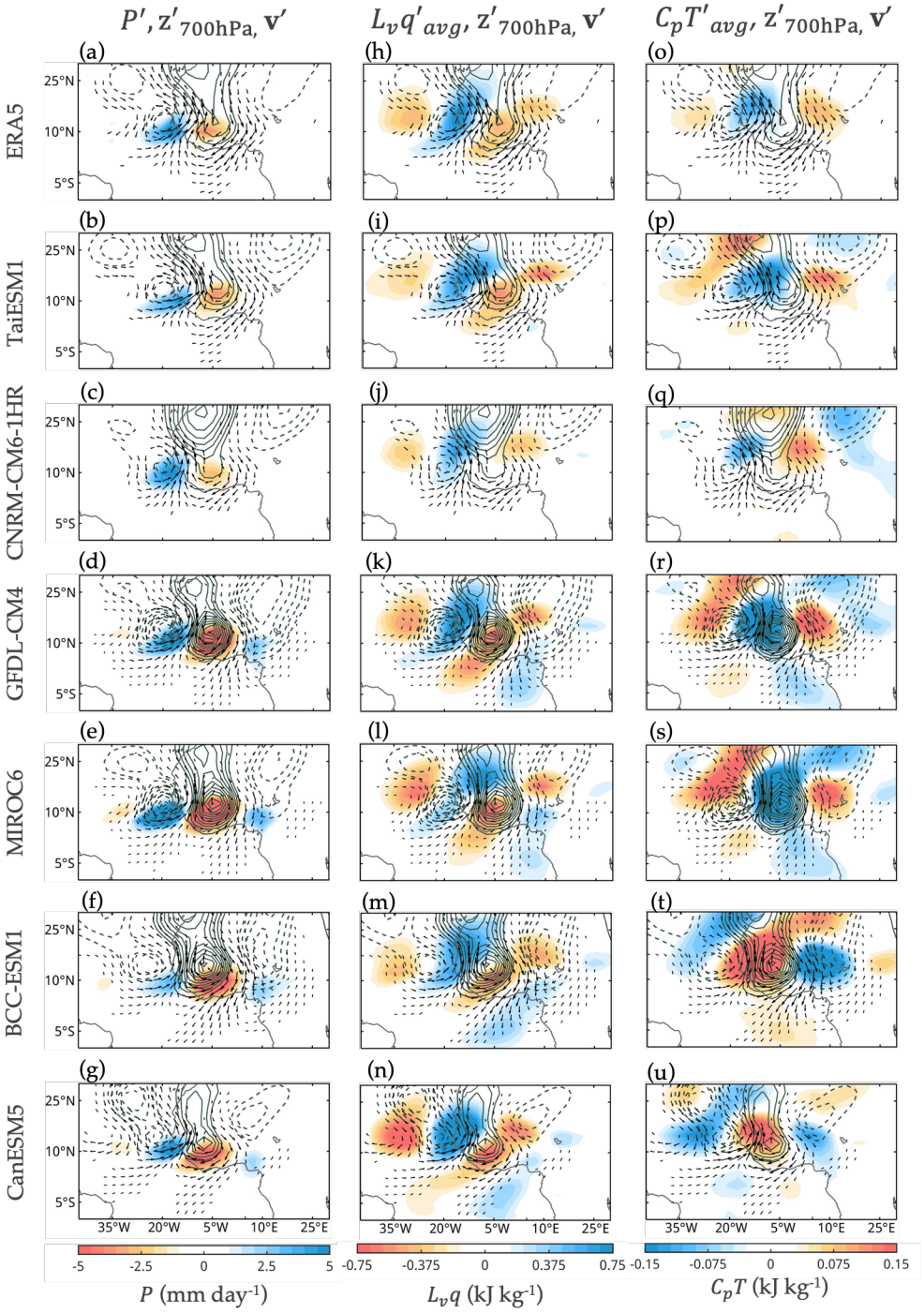


FIGURE 4.6: As in Figure 3.4 but for AEWs-related (a-g) $P$, (h-n) $L_v q'_{\text{avg}}$, (o-u) $C_p T'_{\text{avg}}$, and (v-ab) $m'_{\text{avg}}$ in ERA5 (first row), good (second and third rows), US-SC (fourth and fifth rows), and US-WC (sixth and seventh rows) models. Wind vectors are shown beginning at 0.35 m s$^{-1}$, while $z'_{700\text{hPa}}$ values begin at 1 m with increases every 0.35 m.

The patterns of $m'_{\text{avg}}$ (not shown) indicate that $m'_{\text{avg}}$ can be predominantly explained by its latent energy component (see Figure 4.6.h-n). While the linear regression maps suggest that $m'_{\text{avg}} \simeq L_v q'_{\text{avg}}$ for AEWs, Vargas Martes et al. (2023) show that even then, small values of $C_p T'_{\text{avg}}$ can lead to comparable contributions of $q'_{\text{avg}}$ and $T'_{\text{avg}}$ to $P'$.

### 4.4.3 Diagnostics of physical mechanisms important for AEWs

As in Chapter 3, section 3.4.3, we generalize the results presented in the preceding subsections by analyzing all the models presented in Table 4.1. Based on previous research and the results shown in the preceding subsections, we consider four diagnostics (D1-4) for AEW representation.

D1: We assess the low-frequency background convective adjustment timescale ($\overline{\tau}_c$; Adames, 2017), as Figure 4.6 suggests that it may be important in reproducing AEW-related $P'$.

D2: We analyze a measure of the land ocean differences in $\overline{P}$ ($\overline{P}_{indx}$), as the previous subsections suggest that further decomposing the analysis into its land and oceanic component may provide useful insights on key processes for the generation of realistic AEWs. Moreover, this measure may also provide useful insights on AEW representation, as their growth may be tied to the horizontal distribution of $\overline{P}$ (Adames Corraliza and Mayta, 2024, Lin et al., 2024b).

D3: We examine $\partial_y C_p \overline{T}_{\text{avg}}$, $\partial_y L_v \overline{q}_{\text{avg}}$, and $\partial_y \overline{m}_{\text{avg}}$ to assess baroclinic instability over the region. We examine them based on contradicting bodies of work that suggest

AEWs may grow either from baroclinic (e.g., Hsieh and Cook, 2008, Thorncroft and Hoskins, 1994b) or from moisture-vortex instability (similar mechanisms have also been proposed, such as rotational stratiform instability by Russell et al., 2020) (e.g., Núñez Ocasio and Rios-Berrios, 2023, Russell and Aiyyer, 2020, Russell et al., 2020).

D4: Finally, a measure for AEW growth from moisture-vortex instability (MVI; Adames and Ming, 2018) is assessed by examining the precipitation growth rate presented in Adames Corraliza and Mayta (2024) and Lin et al. (2024b). Their results show that the growth rate of waves that grow from MVI can be predominantly explained by meridional gradients in climatological precipitation and the preferred latitude along which the waves evolve.

The results attained for each diagnostic are presented in the following subsections.

#### 4.4.3.1 D1: $\overline{\tau}_c$

We determine $\overline{\tau}_c$ from equation (7) in Adames (2017),

$$\overline{\tau}_c = \frac{\langle \overline{q_s} \rangle}{a\overline{P}}, \tag{4.1}$$

where $a$ is the steepness of the pickup curve attained from the P$-$CSF distribution in Figure 4.5 (i.e., the slope of the exponential fit). Physically, $\overline{\tau}_c$ can be thought of as

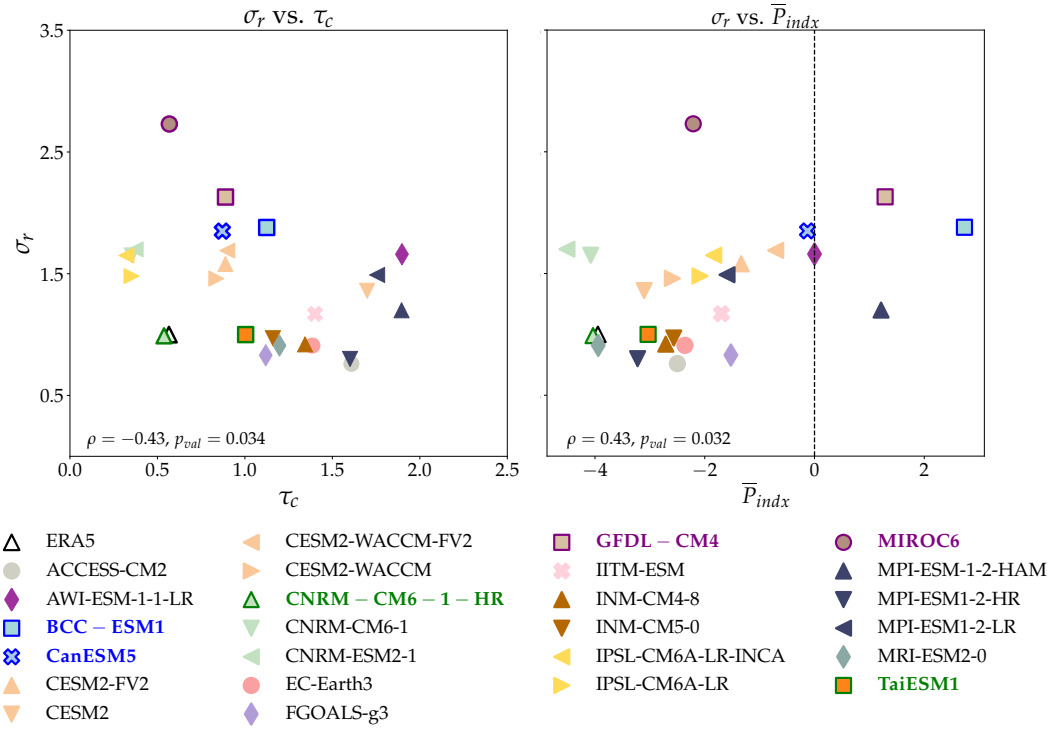


FIGURE 4.7: As in Figure 3.5 but for AEW relationships between $\sigma_r$ and (a) $\overline{\tau}_c$, and (b) $\overline{P}_{indx}$. Models with good, US−SC, and US−WC AEW representation are denoted with green, purple, and blue borders respectively. Analysis for $\overline{\tau}_c$ is carried over a region of strong AEW activity, 5°–17.5°N, 25°W–0°. $\overline{P}_{indx}$ is determined by subtracting the average values over land (2.5°-12.5°E and 5°-12.5°N) and ocean (30°-20°W and 5°-12.5°N). Both relationships are significant at the 95% confidence level.

the timescale for $P'$ to relax the CSF back to its climatological value (Adames, 2017). The values for $\overline{\tau}_c$ in each model are determined by averaging the values in equation 4.1 over 25°W-0° and 5°-17.5°N, where wave activity is high. The spearman correlation coefficient ($\rho$; also known as rank correlation) between $\sigma_r$ and $\overline{\tau}_c$ in Figure 4.7.a indicates that models that produce strong (weaker) AEWs exhibit shorter (longer) $\overline{\tau}_c$ values. This suggests that $P'$ in stronger waves will relax the CSF more quickly than weaker waves.

#### 4.4.3.2 D2: $\overline{P}_{indx}$

Similarly, we determine $\overline{P}_{indx}$ by subtracting the average values over land (2.5°-12.5°E and 5°-12.5°N) and ocean (30°-20°W and 5°-12.5°N). The $\rho$ value between $\sigma_r$ and $\overline{P}_{indx}$ in Figure 4.7.b indicates that models with strong AEWs produce $\overline{P}$ values over land that are larger than or close to the oceanic values (i.e., close to the dashed black line). This result aligns with the results seen in Figure 4.3.a-g, with US−SC and US−WC models overestimating $\overline{P}$ over the continental region.

#### 4.4.3.3 D3: $\partial_y L_v \overline{q}_{\text{avg}}$, $\partial_y C_p \overline{T}_{\text{avg}}$, and $\partial_y \overline{m}_{\text{avg}}$.

To determine $\partial_y L_v \overline{q}_{\text{avg}}$, $\partial_y C_p \overline{T}_{\text{avg}}$, and $\partial_y \overline{m}_{\text{avg}}$ over ocean and land (D3), we choose boxes that correspond to regions of visible meridional changes in each field that coincide with regions of AEW evolution (see Figure 4.3.a-g). The $\partial_y L_v \overline{q}_{\text{avg}}$ is determined over 25°-20°W and 7.5°-25°N (ocean) and 2.5°-7.5°E and 7.5°-25°N (land). Similarly, $\partial_y C_p \overline{T}_{\text{avg}}$ is determined over 25°-20°W and 2.5°-25°N (ocean) and 2.5°-7.5°E and 2.5°-25°N (land). Finally, $\partial_y \overline{m}_{\text{avg}}$ is determined over 25°-20°W and 7.5°-30°N (ocean) and 2.5°-7.5°E and 7.5°-30°N (land). The meridional gradients are determined by first zonally averaging over the selected boxes. Figure 4.8 shows the values of $\partial_y L_v \overline{q}_{\text{avg}}$ (a and d), $\partial_y C_p \overline{T}_{\text{avg}}$ (b and e), and $\partial_y \overline{m}_{\text{avg}}$ (c and f) over the ocean (first row) and land (second row) for ERA5 and all CMIP6 models. The results of Figure 4.8 show a large spread in the representation of the meridional thermodynamic gradients; this spread is more evident over the continental

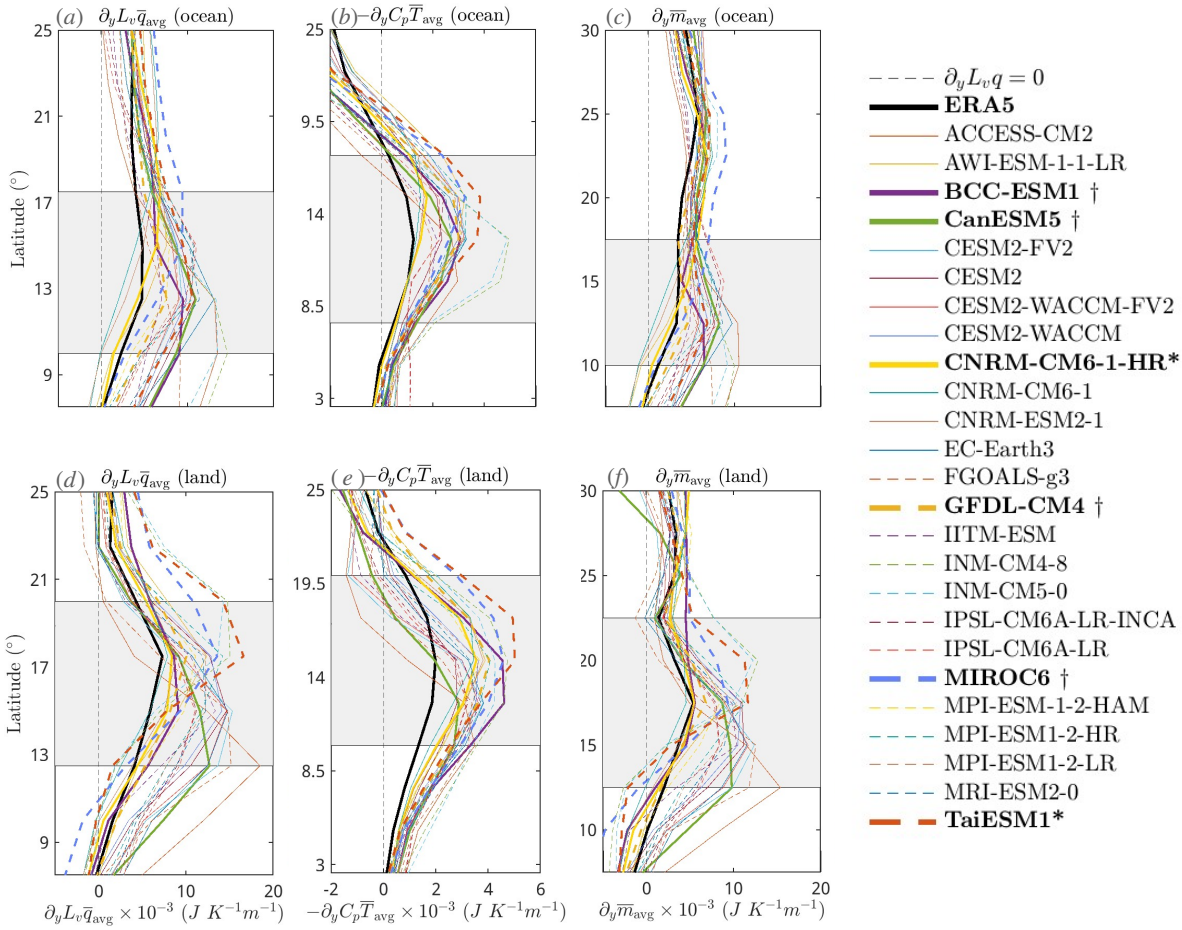


FIGURE 4.8: Meridional gradients in (a and d) $L_v\overline{q}_{\text{avg}}$, (b and e) $C_p\overline{T}_{\text{avg}}$, and (c and f) $\overline{m}_{\text{avg}}$ of reanalysis, and model datasets over the ocean (top row), and land (bottom row). Gradients are determined by zonally averaging over the ocean (25°-20°W) and land (2.5°-7.5°E). The latitudes where most models exhibit positive gradients are further highlighted by the gray box. The names of models that reproduce realistic AEWs are shown in bold. Models selected as good, US−SC and US−WC are denoted by asterisks (*), crosses (†), and stars (⋆) respectively.

region. Most models overestimate the strength of the gradients, with some exhibiting large discrepancies in the latitudes along which the gradient is the strongest.

To compare the average gradient strength between all datasets with $\sigma_r$, we average the values across the latitudes where most models exhibit positive values and that are close to the latitudes where AEW variance is high (gray boxes in Figure 4.8). Figure 4.9 shows

the relationship between $\sigma_r$ and the average strength of $\partial_y L_v \overline{q}_{\text{avg}}$ (a and d), $\partial_y C_p \overline{T}_{\text{avg}}$ (b and e), and $\partial_y \overline{m}_{\text{avg}}$ (c and f) over the ocean (first row) and land (second row) for ERA5 and all CMIP6 models. Figure 4.9.a and d shows that stronger (weaker) AEWs exhibit weaker (stronger) $\partial_y L_v \overline{q}_{\text{avg}}$. While this relationship is stronger over the ocean ($\rho = -0.49$), it is still present over land ($\rho = -0.37$). A similar relationship is observed when examining $\partial_y \overline{m}_{\text{avg}}$ in Figure 4.9.c and f ($\rho = -0.50$ over the ocean and $\rho = -0.37$ over land). While baroclinic instability could still amplify the waves in the presence of $\partial_y L_v \overline{q}_{\text{avg}}$ and $\partial_y \overline{m}_{\text{avg}}$, if there were a significant $\partial_y C_p \overline{T}_{\text{avg}}$ (Adames, 2021), examination of the relationship between $\sigma_r$ and $\partial_y C_p \overline{T}_{\text{avg}}$ in Figure 4.9.b and e did not yield a significant relationship suggesting that the waves do not grow from from baroclinic instability.

#### 4.4.3.4 D4: MVI Criterion

Following previous work that suggests AEWs grow from MVI or similar instabilities (i.e., rotational stratiform instability; Núñez Ocasio and Rios-Berrios, 2023, Russell and Aiyyer, 2020, Russell et al., 2020) as their PEWs (Mayta and Adames, 2023, Mayta and Adames Corraliza, 2024), we examine a measure for growth from MVI, shown in Adames Corraliza and Mayta (2024) and Lin et al. (2024b),

$$\varpi_i \propto -f \partial_y L_v \overline{P}, \tag{4.2}$$

.

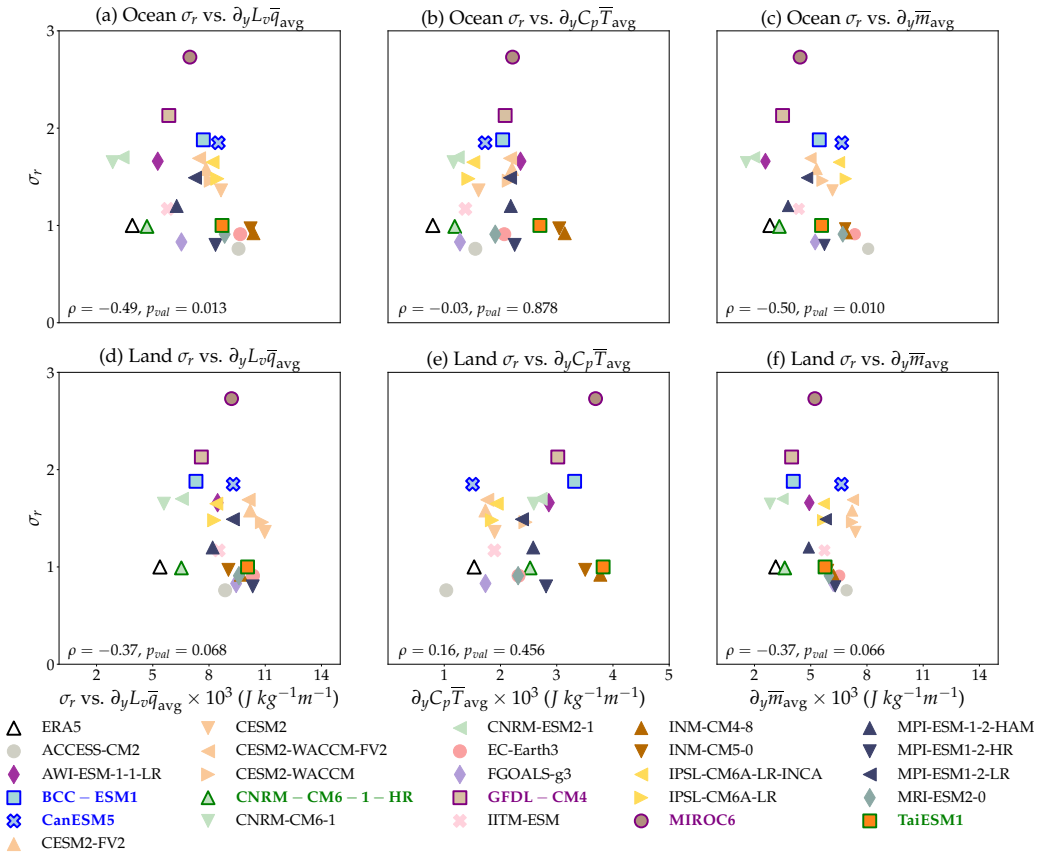


FIGURE 4.9: As in Figure 4.7 but for (a and d) $\partial_y L_v \overline{q}_{\text{avg}}$, (b and e) $\partial_y C_p \overline{T}_{\text{avg}}$, and (c and f) $\partial_y \overline{m}_{\text{avg}}$, over ocean (top row), and land (bottom row). Over the ocean, both $\partial_y L_v \overline{q}_{\text{avg}}$ and $\partial_y \overline{m}_{\text{avg}}$ relationships are significant at the 95% confidence level, whereas over land they are significant at the 90% confidence level.

for both PEWs and AEWs. Where $\varpi_i$ is the $P'$ growth rate, $f = 2\Omega \sin\phi$ is the planetary vorticity, $\Omega = 7.3 \times 10^{-5} s^{-1}$ is the Earth's angular velocity and $\phi = 10°N$ is the EW preferred latitude. Thus, as in the preceding section, we determine $-f\partial_y L_v \overline{P}$ along the PEWs (85°-80°W and 7.5°-25°N) and AEWs (5°W-0° and 7.5°-25°N) evolution regions. The results in Figure 4.10 show that there is a higher agreement between models and reanalysis in the representation of the gradients over West Africa than over the east Pacific.

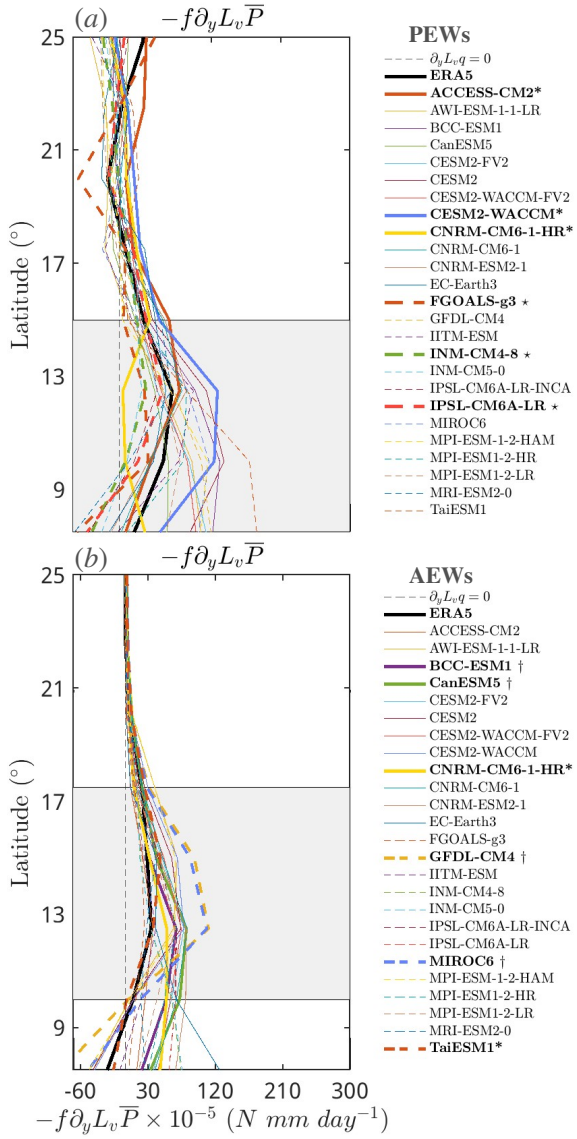


FIGURE 4.10: As in Figure 4.8 but for (a-b) $-f\partial_y Lv\overline{P}$ over the east Pacific Ocean (top row), and west Africa (bottom row). The names of models with realistic PEW representation are shown in bold. Models used in the realistic and unrealistically weak model ensembles in Chapter 3, are marked with asterisks (*) and stars ($\star$) respectively. The $-f\partial_y Lv\overline{P}$ values are determined by zonally averaging over 85°-80°W for the east Pacific, and 5°W-0° for West Africa.

We attain the average gradient strength values by averaging $-f\partial_y L_v\overline{P}$ over the latitudes where most models exhibit positive gradients (gray box in Figure 4.10). The results

shown in Figure 4.11 indicate that over both regions there is a statistically significant relationship between $\sigma_r$ and $-f\partial_y L_v \overline{P}$ ($\rho = 0.49$ for PEWs and $\rho = 0.79$ for AEWs). This result indicates that waves with stronger (weaker) amplitudes exhibit stronger (weaker) $-f\partial_y L_v \overline{P}$. This novel result suggests that, *as oceanic TD-type waves, AEWs grow from MVI.* Values over the east Pacific are considerably lower than over West Africa, a result that seems counterintuitive given the moisture mode nature of PEWs. However, the weaker relationship between the fields over the east Pacific is due to a more complex topography and horizontal distributions in $\overline{P}$, as well as more distinct PEW tracks between models which muddle the results over the region. Another result that merits further discussion is that a stronger relationship is observed between $\sigma_r$ and $-f\partial_y L_v \overline{P}$ than between $\sigma_r$ and $\partial_y L_v \overline{q}_{\text{avg}}$. Given the relationship that exists between both fields (e.g., Bretherton et al., 2004), this might seem like a counterintuitive result. However, in their equation (6), Adames (2017) show that,

$$P' \simeq a \frac{\overline{P}}{\langle q_s \rangle} \langle q' \rangle. \tag{4.3}$$

Via this relationship we see that we that $P'$ does not only depend on $\langle q' \rangle$, but is a function of other factors, as shown in 4.3. The fact that $P$ is a function of various fields could be contributing to the stronger relationship shown between $\sigma_r$ and $-f\partial_y L_v \overline{P}$.

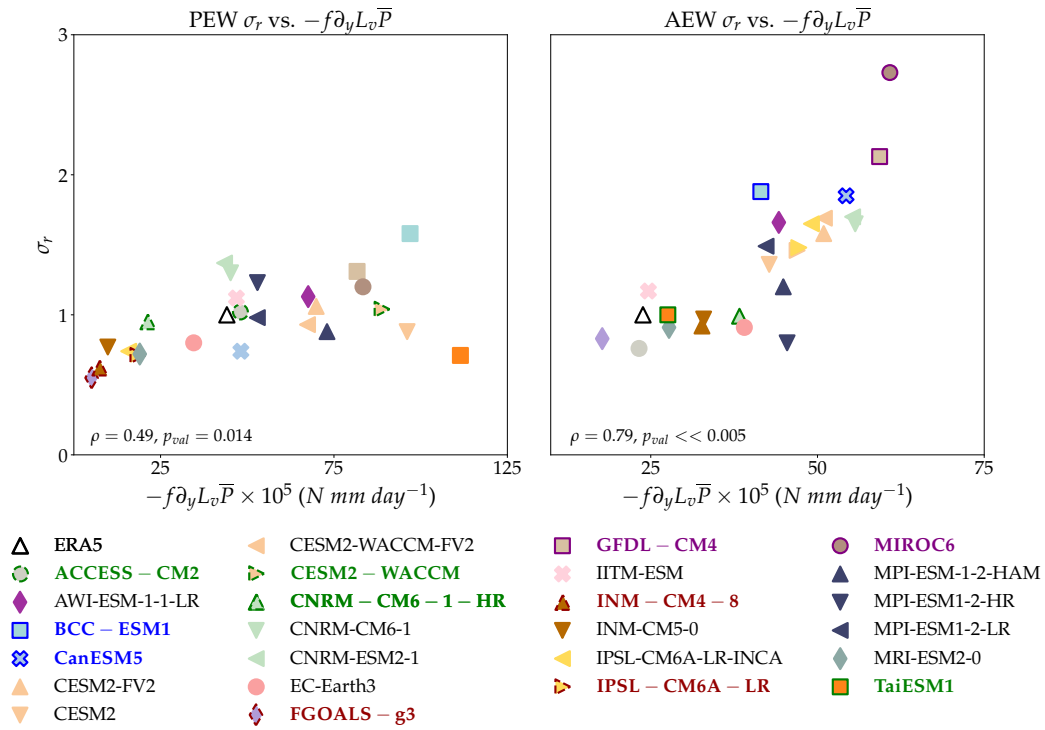


FIGURE 4.11: As in Figure 4.8 but for the relationship between $\sigma_r$ and $-f\partial_y\overline{P}$ over (a) the east Pacific, and (b) west Africa. Models with good, US−SC, and US−WC AEW representation are denoted with green, purple, and blue borders respectively. Models with good, and unrealistically weak PEW representation are denoted by the dashed green, maroon borders respectively.

## 4.5 Summary and Conclusions

In this chapter we examined the representation of AEWs in 25 CMIP6 models by assessing the spatial coherence and amplitude of lag-regressed $P'$ in models vs. reanalysis during boreal summer. As in Chapter 3, we posed two questions at the begining of this study. Q1: Are CMIP6 models able to reproduce AEWs? Q2: What are the differences in the thermodynamics and mean state between models with realistic and un realistically strong waves? The large spread in model representation of AEWs comes from the overestimation of the wave amplitude and spatiotemporal differences in the $P'$ pattern in models when

compared to reanalysis. The thermodynamic analysis and diagnostics reveal five findings that help us answer Q2.

First, our linear regression analysis revealed that US−SC and US−WC models exhibit stronger values in anomalous $P'$, $L_v q'_{\text{avg}}$, $C_p T'_{\text{avg}}$, and $m'_{\text{avg}}$, $z'_{700\text{hPa}}$, and $v'_{700\text{hPa}}$ when compared to good models and reanalysis. With US−WC models exhibiting a partial collocation between the thermodynamic fields and circulation across all longitudes. Future work should be conducted to explore the causes of these differences in more detail.

Our second result related to Q2 is that models that reproduce stronger (weaker) AEWs exhibit shorter (longer) values of $\overline{\tau}_c$. This result is akin to the findings of Vargas Martes et al. (2024), who show a similar relationship between $\sigma_r$ and the convective moisture adjustment timescale ($\tau'_c$; see Chapter 3). This means that in the absence of other processes modulating convection, in stronger (weaker) AEWs convection quickly (slowly) dries up the troposphere (Adames, 2017, Adames and Maloney, 2021).

The third finding related to Q2 is that the models exhibiting stronger AEWs also exhibit values of $\overline{P}$ over land that are larger or close-to the oceanic values. This is in agreement with the results presented in Figure 4.4, which show that US−SC and US−WC produce heavier seasonal rainfall over the African Monsoon region when compared to good models and reanalysis. While the results shown in Figure 4.5 suggest that models exhibit similar sensitivities of $P$ to CSF, the horizontal distribution of $\overline{P}$ exhibits larger variations between datasets.

To gain further insights on Q2, our fourth finding indicates that models with stronger (weaker) AEWs exhibit weaker (stronger) $\partial_y L_v \overline{q}_{\text{avg}}$ and $\partial_y \overline{m}_{\text{avg}}$. No significant relationship was attained between $\sigma_r$ and $\partial_y C_p \overline{T}_{\text{avg}}$. A large latitudinal spread is observed in the maximum values of $\partial_y L_v \overline{q}_{\text{avg}}$, $\partial_y C_p \overline{T}_{\text{avg}}$, and $\partial_y \overline{m}_{\text{avg}}$ between datasets. Because TD-type systems have been found to evolve over regions of strong meridional $\partial_y L_v \overline{q}_{\text{avg}}$ and $\partial_y \overline{m}_{\text{avg}}$ gradients (e.g., Lin et al., 2024a, Mayta and Adames Corraliza, 2024), these meridional shifts in the mean state fields could have significant impacts on AEW representation.

Finally, our fifth finding indicates that stronger (weaker) PEWs and AEWs exhibit stronger (weaker) $-f\partial_y L_v \overline{P}$ values. This novel result suggest that EWs grow from MVI even in the presence of a strong $\partial_y C_p \overline{T}_{\text{avg}}$ as proposed by theory (Adames, 2021). This underscores the important role that TD-type waves play in the weakening of the Hadley Cell, by extracting energy from the background $\partial_y L_v \overline{q}$ (Adames Corraliza and Mayta, 2024, Lin et al., 2024b).

While the results presented in this chapter do not fully explain the majority of the variance on their own (62% at most), they begin to draw a picture of the key processes for the accurate representation of AEWs. Primarily, the results show that the distribution of $\overline{P}$, especially the land-ocean contrasts, and the latitude of the maximum $\partial_y \overline{P}$ values may be of particular importance. Further examination of these relationships should be carried out in future studies. The good models presented in this study may be employed in studies that wish to understand how AEW respond to a warming climate. In addition, further analysis could be employed with the CNRM-CM6-1-HR and EC-Earth3 models to

understand key EW-related processes as they were the only models capable or reproducing both PEWs and AEWs.

# Chapter 5

# Summary and Conclusion

The governing thermodynamic structure of PEWs and AEWs is examined and their representation in CMIP6 models is assessed in this dissertation. The implementation of a novel plume buoyancy framework (Adames et al., 2021, Ahmed et al., 2020, Ahmed and Neelin, 2018), moisture mode theory (Adames, 2022, Adames et al., 2019, Adames Corraliza and Mayta, 2024, Ahmed et al., 2021, Lin et al., 2024b, Mayta et al., 2022), linear- and lag-regression analysis (e.g., Adames and Wallace, 2014, Cheng et al., 2019, Kiladis et al., 2009), and pattern correlations (e.g., Henderson et al., 2017) aided in the understanding of key processes influencing the structure of AEWs and PEWs and how these processes are represented in CMIP6 models. More importantly, the aggregate of the results presented in Chapters 2, 3, and 4 elucidated the importance of moist processes for the growth of waves with evolution over ocean and land. A brief summary and discussion of these key findings as well as some directions for future work are presented in this

chapter.

## 5.1 Chapter 2: The role of water vapor and temperature in the thermodynamics of Tropical Northeast Pacific and African easterly Waves

In this chapter, we investigated the relative contributions of moisture and temperature to the observed PEW- and AEW-related convection, as well as the processes governing the thermodynamic structure of both transients. The key findings of this study can be summarized as follows:

- PEWs are moisture modes, waves whose thermodynamics are driven my anomalous moisture (e.g., Neelin and Yu, 1994, Sobel et al., 2001).
- AEWs are mixed systems, whose thermodynamics are governed comparably by both anomalous moisture and temperature (e.g., (Wolding et al., 2020)).
- The novel plume-buoyancy framework of Ahmed et al. (2020) can be used to understand the contributions of moisture and temperature to the PEW- and AEW-associated convection.
- Both transients evolve over regions of strong meridional moisture and moist static energy gradients.

- The leading principal component structures of PEW- and AEW-associated precipitation obtained from the reanalysis and a plume-buoyancy estimate are capable of reproducing the structure obtained from satellite observations.

The novel approach of decomposing precipitation by the contributions of different thermodynamic fields allowed this work to gain an in-depth understanding of key processes modulating PEW- and AEW-related convection. These results underscore the relevance of moist processes, even in the presence of significant temperature gradients, as suggested by previous work (e.g., Berry and Thorncroft, 2012, Russell and Aiyyer, 2020, Russell et al., 2020). These results also provide a strong argument in favor of moisture mode theory for the understanding of these large scale tropical eddies.

## 5.2 Chapter 3: East Pacific Easterly Wave Representation in CMIP6 models

In this chapter we assessed the representation of PEWs via pattern correlations of lag-regressed precipitation by examining the spatial coherence and wave relative amplitude between reanalysis and CMIP6 models. The key findings of this study can be summarized as follows:

- CMIP6 models exhibit a large spread in skill when representing PEWs. This spread includes models that overestimate and underestimate the wave amplitude, as well as models exhibiting high and low spatial coherence when compared to reanalysis.

- Unrealistically weak models exhibit weak precipitation anomalies relative to good models, even though moisture fluctuations are comparable.

- Models with larger precipitation anomalies have weaker meridional humidity gradients and higher precipitation over the Panama Bight.

The examination of PEW-representation in GCMs, has not been extensively studied to the author's knowledge. Thus, this research provides an important stepping stone to further our understanding, not only of the representation of these circulations, but of the key processes needed for their realistic representation in GCMs. The results presented in this chapter further support the idea that PEWs are moisture modes (Mayta and Adames, 2021, Mayta and Adames Corraliza, 2024, Vargas Martes et al., 2023, Wolding et al., 2020). Thus, models must accurately capture moist processes (i.e., convection sensitivity to column moisture, horizontal distribution of climatological column moisture and precipitation, etc.) in order to reproduce realistic PEWs. These results further underscore the relevance of moisture mode theory in understand oceanic TD-type systems (Adames Corraliza and Mayta, 2024, Mayta and Adames, 2021, Mayta and Adames Corraliza, 2024).

## 5.3 Chapter 4: African Easterly Wave Representation in CMIP6 models

We similarly assessed the representation of AEWs in CMIP6 models in this chapter implementing the same AEW representation metrics (i.e., relative wave amplitude and

spatial coherence between reanalysis and model datasets). We summarize the key findings of this study as follows:

- CMIP6 models exhibit a large spread in skill when representing AEWs. This spread includes models that overestimate the wave amplitude, as well as models exhibiting high and low spatiotemporal coherence between anomalous precipitation patterns when compared to reanalysis.
- Models with unrealistically strong AEWs exhibit strong mean state precipitation over the African Monsoon region, stronger anomalous moisture, temperature and moist static energy, smaller moist convective adjustment timescales, and weaker mean state meridional humidity and moist static energy gradients.
- Easterly Wave growth is more consistent with moisture-vortex instability than baroclinic instability.

These novel findings support the idea that TD-type systems grow from MVI even in the presence of strong meridional moisture gradients as suggested by previous studies (Mayta et al., 2024, Núñez Ocasio and Rios-Berrios, 2023, Russell and Aiyyer, 2020, Russell et al., 2020). The fact that the lower skill of models in representing AEWs came from the overestimation of anomalous precipitation and differing values of spatiotemporal coherence between reanalysis and model datasets supports the idea that models struggle with reproducing moist processes. This may be tied to the fact that AEWs are mixed systems whose thermodynamics are comparably governed by moisture and temperature

anomalies (Vargas Martes et al., 2023, Wolding et al., 2020). Thus, even if models struggle to represent moist processes, a representation of AEWs that is close to that seen in reanalysis may still be achieved, whereas the same is not true over the east Pacific Ocean.

## 5.4 Future Work

The results discussed above paint a clear picture of the role that moisture and moisture-driven processes have in the representation of both PEWs and AEWs. Thus, future work should be guided at further assessing if these relationships hold in the scope of reanalysis, modeling, and observational datasets. Many of the studies that examine TD-type wave growth have a focus over oceanic regions (Adames Corraliza and Mayta, 2024, Mayta and Adames, 2021, Mayta and Adames Corraliza, 2024). Thus, a thorough examination of AEWs under the scope of growth from MVI should be carried out to gain further insight on the role these systems may play in the tropical general circulation (see Adames Corraliza and Mayta, 2024). Models that were identified as being able to reproduce realistic PEWs and AEWs (CNRM-CM6-1-HR and EC-Earth3) should be employed in studies that examine how these systems will respond to a warming climate. Furthermore, the dynamics and thermodynamics of these models should be further examined as they may provide useful insights on key processes for EW representation over both basins.

# Appendix A

# Appendix: $q'$ and $T'$ structure and relationship

Vargas Martes, R.M., Á. F. Adames Corraliza, and V. C. Mayta, 2023: The role of water vapor and temperature in the thermodynamics of Tropical Northeast Pacific and African easterly waves. *J. Atmos. Sci.*, 2305 - 2322, doi: https://doi.org/10.1175/JAS-D-22-0177.1.

© American Meteorological Society. Used with permission.

In the main text we showed how moisture and temperature contribute to $P_{est}$. For completeness, we show here the horizontal structure of $L_v q'_L$ and $C_p T'_L$ for PC1 and PC2 of EW activity ( Figs. A.1 and A.2, respectively). In PEWS $q'$ extends away from the $z'$ centers, exhibiting a SW-NE tilt over both regions as observed by Rydbeck and Maloney (2015). A comparison of the left panels in Figs. A.1 and A.2 reveals that $C_p T'$ is smaller than $L_v q'$ over both regions. However, AEWs exhibit larger $C_p T'$ values than PEWs. Over WAEA, high (low) values of $T'$ occur under the regions of high (low) $z'$. The similarity of the horizontal structure of $T'$ and $q'$ suggests that adiabatic motions are likely taking place and influencing wave development over this region, as suggested by Wolding et al. (2020).

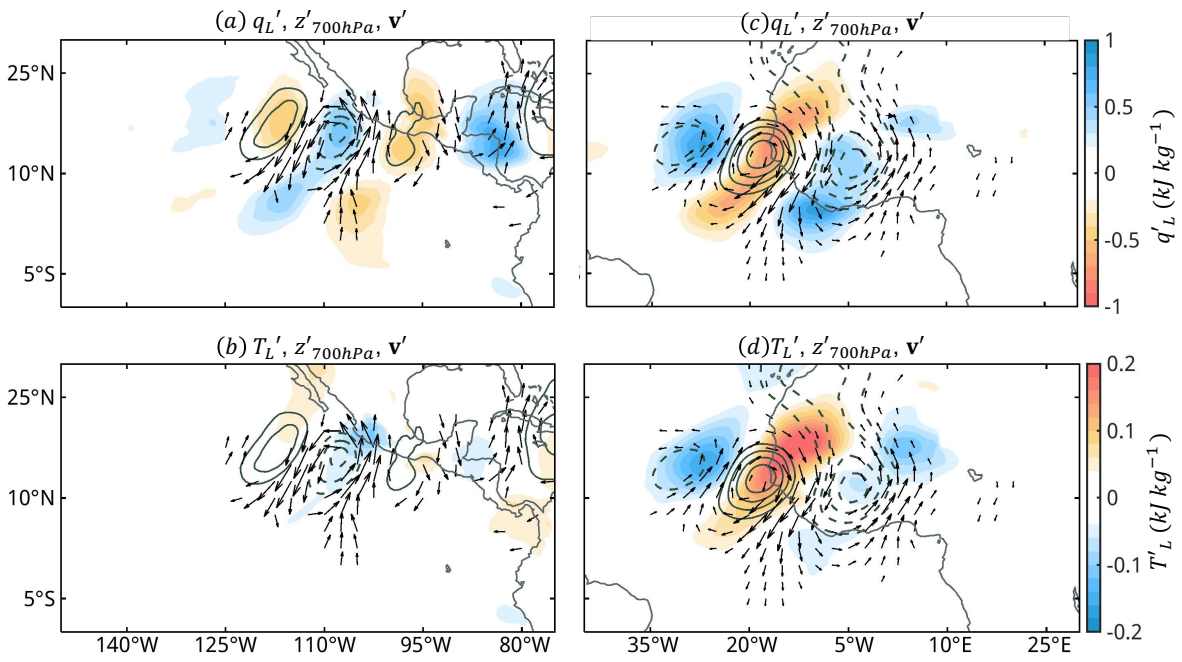


FIGURE A.1: As in Fig. 2.4, but showing latent energy ($L_v q'_L$) and temperature energy ($C_p T'$) as the shaded fields.

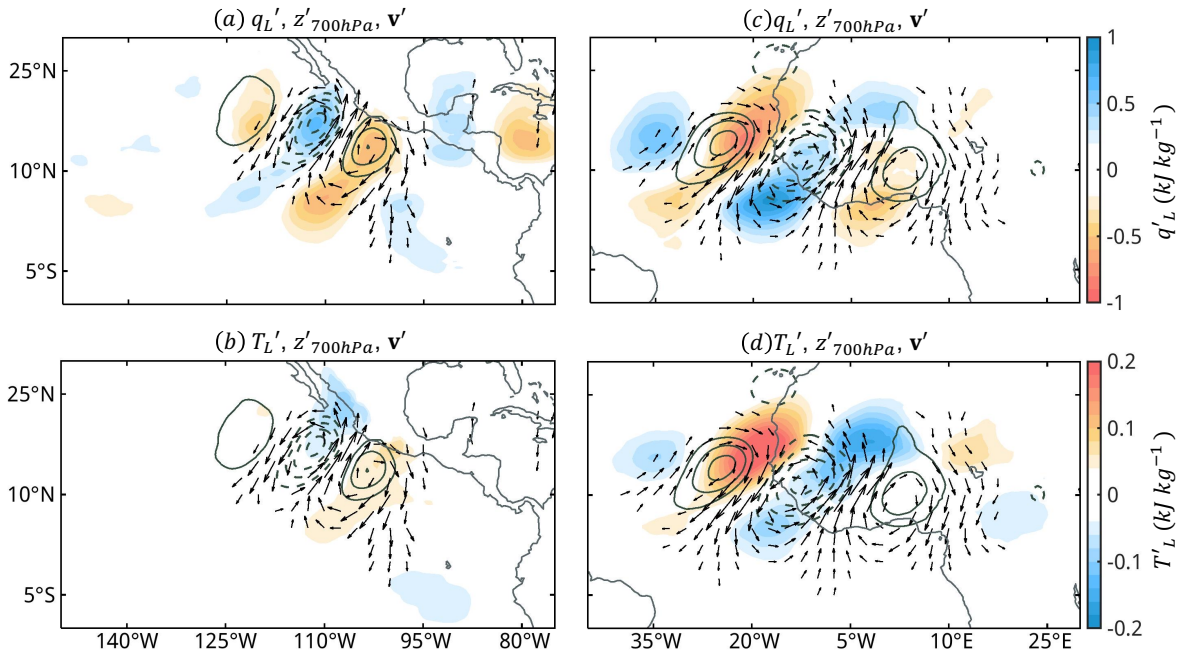


FIGURE A.2: As in Fig. 2.4, but showing latent energy ($L_v q'_L$) and temperature energy ($C_p T'$) as the shaded fields for PC2.

# Appendix B

# Appendix: Plume buoyancy-based precipitation estimate and TRMM precipitation

Vargas Martes, R.M., Á. F. Adames Corraliza, and V. C. Mayta, 2023: The role of water vapor and temperature in the thermodynamics of Tropical Northeast Pacific and African easterly waves. *J. Atmos. Sci.*, 2305 - 2322, doi: https://doi.org/10.1175/JAS-D-22-0177.1.

© American Meteorological Society. Used with permission.

In the preceding sections it was shown that $P'_{est}$ captures the horizontal distribution and magnitude of $P'$. However, given known limitations in reanalysis-based rainfall rates (Adames, 2017, Kiranmayi and Maloney, 2011, Mapes and Bacmeister, 2012, Ren et al., 2021, Rushley et al., 2022) it is instructive to compare $P'_{est}$ with TRMM (Huffman et al., 2007), and Global Precipitation Measurement Mission (GPM) precipitation ($P_{TRMM}$). The data used is twice daily with a $2.5° \times 2.5°$ horizontal resolution. For more information on the $P_{TRMM}$ data used, refer to Sakaeda et al. (2020). Fig. B.1 shows $P'$, $P_{est}$, and $P_{TRMM}$ for PEWs and AEWs for the 1998-2016 period. It is evident that over both domains the diagnostic precipitation is able to capture the predominant patterns of both $P'$ and $P'_{TRMM}$, underscoring the robustness of $P'_{est}$.

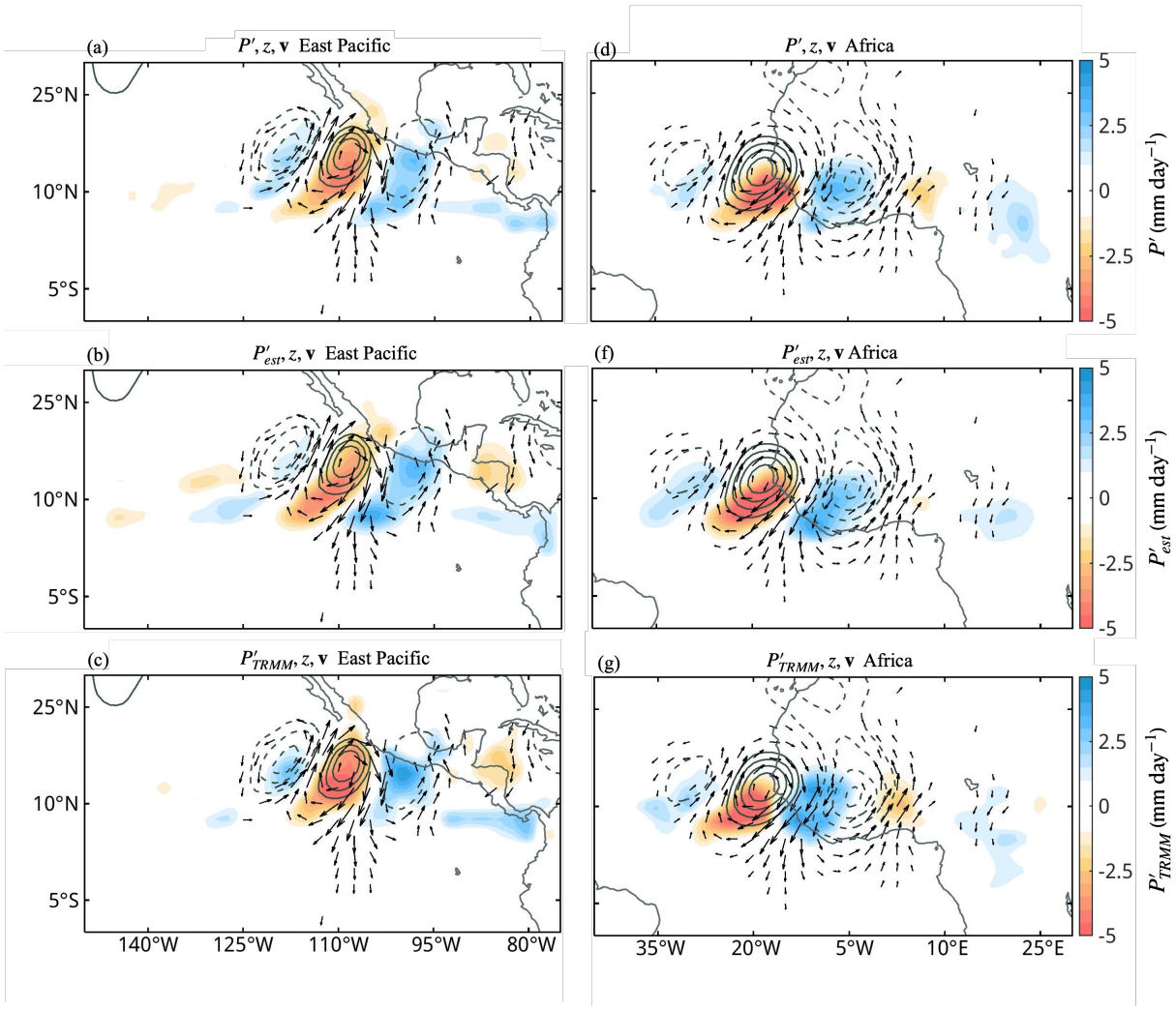


FIGURE B.1: Regression maps of anomalous (top) ERA5 precipitation ($P'$), geopotential height ($z'$), and horizontal winds ($\mathbf{v}'$), (middle) estimated precipitation ($P'_{est}$), $z'$, and $\mathbf{v}'$, and (bottom) TRMM/GPM precipitation ($P'_{TRMM}$), $z'$, and $\mathbf{v}'$, for PC1 for (left) PEWs and (right) AEWs. Contour interval is 0.5 m, starting at 1 m. The longest arrows correspond to a wind anomaly of 1.8 m s$^{-1}$

# Appendix C

# Appendix: Leading omega structure in PEWs and AEWs

Vargas Martes, R.M., Á. F. Adames Corraliza, and V. C. Mayta, 2023: The role of water vapor and temperature in the thermodynamics of Tropical Northeast Pacific and African easterly waves. *J. Atmos. Sci.*, 2305 - 2322, doi: `https://doi.org/10.1175/JAS-D-22-0177.1`.

© American Meteorological Society. Used with permission.

A central component of the calculation of $N_{mode}$ is the calculation of $c$, which is tied to the vertical profile of $\omega$. Here we look at the leading PC of $\omega'$ as obtained from an EOF analysis of the three-dimensional structure of the linear regressions, as in Adames and Wallace (2014). This is attained by performing an EOF analysis on the horizontal linear regressions of $\omega$ (for PC1 and PC2) at each level (1000-100 hPa). While the vertical structure of EWs is more complex than PEWs, both qualitatively exhibit a first baroclinic vertical structure, justifying the use of $c = 50$ m s$^{-1}$.

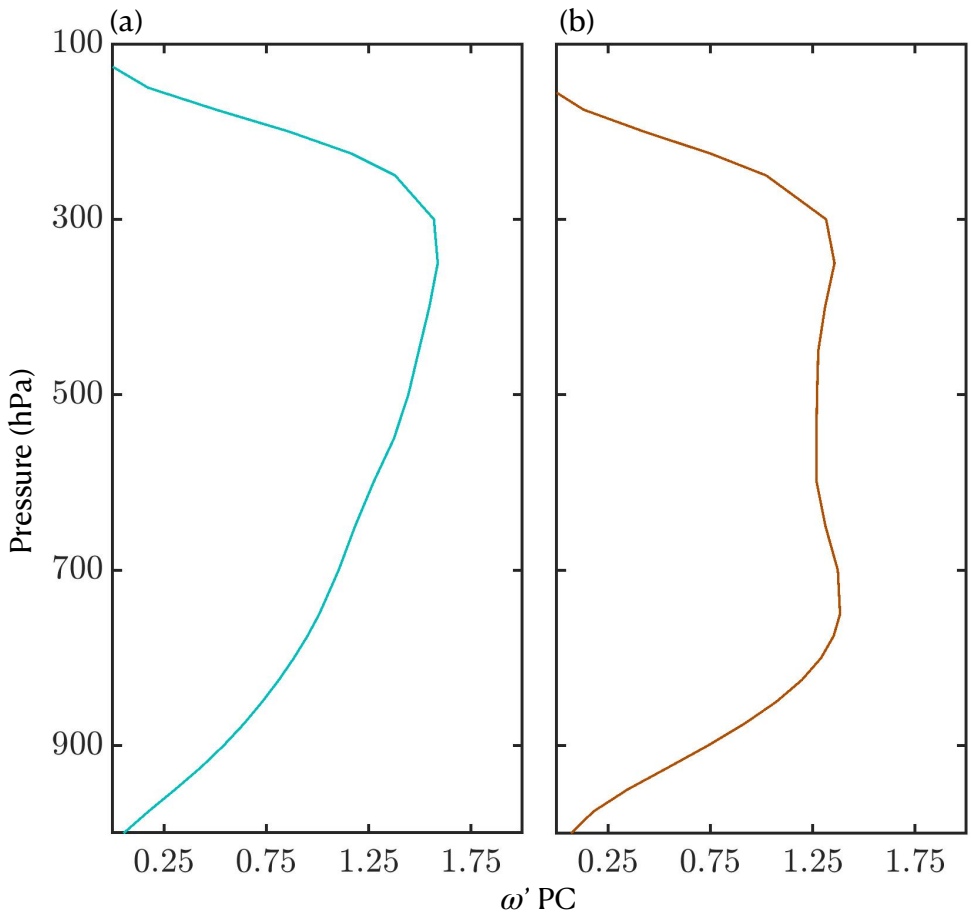


FIGURE C.1: Leading principal component of vertical velocity ($\omega'$) over the EPAC (150°W-75°W and 10°$S$-30°N) (left) and WAEA (45°W-30°E and 10°$S$-30°N) (right).

# Appendix D

# Appendix: Supporting Information for "East Pacific Easterly Wave Representation in CMIP6 Models"

© Copyright by Rosa M. Vargas Martes, Ángel F. Adames Corraliza, Víctor Mayta and Qiao-Jun Lin (2024)

Table D.1: CMIP6 model name, run, and original resolution used in the study Eyring et al. (2016).

| CMIP6 Model | Ensemble member | lat/lon grid (°) |
|---|---|---|
| ACCESS-CM2 | r1i1p1f1 | 1.25 × 1.88 |
| AWI-ESM-1-1-LR | r1i1p1f1 | 1.88 × 1.88 |
| BCC-ESM1 | r1i1p1f1 | 2.81 × 2.81 |
| CanESM5 | r1i1p2f1 | 2.81 × 2.81 |
| CESM2-FV2 | r1i1p1f1 | 1.88 × 2.50 |
| CESM2 | r1i1p1f1 | 0.94 × 1.25 |
| CESM2-WACCM-FV2 | r1i1p1f1 | 1.88 × 2.50 |
| CESM2-WACCM | r1i1p1f1 | 0.94 × 1.25 |
| CNRM-CM6-1-HR | r1i1p1f2 | 0.50 × 0.50 |
| CNRM-CM6-1 | r1i1p1f2 | 1.41 × 1.41 |
| CNRM-ESM2-1 | r1i1p1f2 | 1.41 × 1.41 |
| EC-Earth3 | r3i1p1f1 | 0.70 × 0.70 |
| FGOALS-g3 | r1i1p1f1 | 2.25 × 2.00 |
| GFDL-CM4 | r1i1p1f1 | 1.00 × 1.25 |
| IITM-ESM | r1i1p1f1 | 1.91 × 1.88 |
| INM-CM4-8 | r1i1p1f1 | 1.50 × 2.00 |
| INM-CM5-0 | r1i1p1f1 | 1.50 × 2.00 |
| IPSL-CM6A-LR-INCA | r1i1p1f1 | 1.26 × 2.50 |
| IPSL-CM6A-LR | r1i1p1f1 | 1.26 × 2.50 |
| MIROC6 | r1i1p1f1 | 1.41 × 1.41 |
| MPI-ESM-1-2-HAM | r1i1p1f1 | 1.88 × 1.88 |
| MPI-ESM1-2-HR | r1i1p1f1 | 0.94 × 0.94 |
| MPI-ESM1-2-LR | r1i1p1f1 | 1.88 × 1.88 |
| MRI-ESM2-0 | r1i1p1f1 | 1.13 × 1.13 |
| TaiESM1 | r1i1p1f1 | 0.94 × 1.25 |

# Bibliography

Adames, Á. F., 2017: Precipitation budget of the madden–julian oscillation. *Journal of the Atmospheric Sciences*, **74**, 1799 – 1817, doi:https://doi.org/10.1175/JAS-D-16-0242.1.

— 2021: Interactions between water vapor, potential vorticity, and vertical wind shear in quasi-geostrophic motions: Implications for rotational tropical motion systems. *Journal of the Atmospheric Sciences*, **78**, 903 – 923, doi:10.1175/JAS-D-20-0205.1.

— 2022: The basic equations under weak temperature gradient balance: Formulation, scaling, and types of convectively-coupled motions. *Journal of the Atmospheric Sciences*, doi:10.1175/JAS-D-21-0215.1.

Adames, Á. F. and D. Kim, 2016: The mjo as a dispersive, convectively coupled moisture wave: Theory and observations. *Journal of the Atmospheric Sciences*, **73**, 913 – 941, doi:https://doi.org/10.1175/JAS-D-15-0170.1.

Adames, Á. F., D. Kim, S. K. Clark, Y. Ming, and K. Inoue, 2019: Scale analysis of moist thermodynamics in a simple model and the relationship between moisture

modes and gravity waves. *Journal of the Atmospheric Sciences*, **76**, 3863 – 3881, doi:https://doi.org/10.1175/JAS-D-19-0121.1.

Adames, Á. F. and E. D. Maloney, 2021: Moisture mode theory's contribution to advances in our understanding of the madden-julian oscillation and other tropical disturbances. *Current Climate Change Reports*, **7**, 72–85.

Adames, Á. F. and Y. Ming, 2018: Moisture and moist static energy budgets of south asian monsoon low pressure systems in gfdl am4.0. *Journal of the Atmospheric Sciences*, **75**, 2107 – 2123, doi:10.1175/JAS-D-17-0309.1.

Adames, Á. F., S. W. Powell, F. Ahmed, V. C. Mayta, , and J. D. Neelin, 2021: Tropical precipitation evolution in a buoyancy-budget framework. *Journal of the Atmospheric Sciences*, **78**, 509 – 528, doi:https://doi.org/10.1175/JAS-D-20-0074.1.

Adames, Á. F. and J. M. Wallace, 2014: Three-dimensional structure and evolution of the vertical velocity and divergence fields in the mjo. *Journal of the Atmospheric Sciences*, **71**, 4661 – 4681, doi:https://doi.org/10.1175/JAS-D-14-0091.1.

Adames Corraliza, Á. F. and V. C. Mayta, 2024: The stirring tropics: Theory of moisture mode–hadley cell interactions. *Journal of Climate*, **37**, 1383 – 1401, doi:10.1175/JCLI-D-23-0147.1.

Ahmed, F., Á. F. Adames, and J. D. Neelin, 2020: Deep convective adjustment of temperature and moisture. *Journal of the Atmospheric Sciences*, **77**, 2163 – 2186, doi:https://doi.org/10.1175/JAS-D-19-0227.1.

Ahmed, F. and J. D. Neelin, 2018: Reverse engineering the tropical precipitation–buoyancy relationship. *Journal of the Atmospheric Sciences*, **75**, 1587 – 1608, doi:https://doi.org/10.1175/JAS-D-17-0333.1.

Ahmed, F., J. D. Neelin, and Ángel F. Adames, 2021: Quasi-equilibrium and weak temperature gradient balances in an equatorial beta-plane model. *Journal of the Atmospheric Sciences*, **78**, 209 – 227, doi:10.1175/JAS-D-20-0184.1.

Air Weather Service Scott AFB, I., 1944: Interpretation of weather over the pacific. Technical report, Air Force.
URL `https://apps.dtic.mil/sti/citations/tr/ADA800383`

Avila, L. A. and J. L. Guiney, 2000: Eastern north pacific hurricane season of 1998. *Monthly Weather Review*, **128**, 2990 – 3000, doi:10.1175/1520-0493(2000)128¡2990:ENPHSO¿2.0.CO;2.

Avila, L. A., R. J. Pasch, J. L. Beven, J. L. Franklin, M. B. Lawrence, S. R. Stewart, and J.-G. Jiing, 2003: Eastern north pacific hurricane season of 2001. *Monthly Weather Review*, **131**, 249 – 262, doi:10.1175/1520-0493(2003)131¡0249:ASNPHS¿2.0.CO;2.

Berry, G. J. and C. D. Thorncroft, 2012: African easterly wave dynamics in a mesoscale numerical model: The upscale role of convection. *Journal of the Atmospheric Sciences*, **69**, 1267 – 1283, doi:https://doi.org/10.1175/JAS-D-11-099.1.

Bretherton, C. S., M. E. Peters, and L. E. Back, 2004: Relationships between water vapor path and precipitation over the tropical oceans. *Journal of Climate*, **17**, 1517 – 1528, doi:https://doi.org/10.1175/1520-0442(2004)017¡1517:RBWVPA¿2.0.CO;2.

Camargo, S. J., 2013: Global and regional aspects of tropical cyclone activity in the cmip5 models. *Journal of Climate*, **26**, 9880 – 9902, doi:https://doi.org/10.1175/JCLI-D-12-00549.1.

Chaboureau, J.-P., F. M. Guichard, J.-L. Redelsperger, and J.-P. Lafore, 2004: Role of stability and moisture on the diurnal cycle of convection over land. *Quarterly Journal of the Royal Meteorological Society*, **130**, 3105 – 3117, doi:https://doi.org/10.1256/qj.03.132.

Chen, W. Y., 1982: Fluctuations in northern hemisphere 700 mb height field associated with the southern oscillation. *Monthly Weather Review*, **110**, 808 – 823, doi:https://doi.org/10.1175/1520-0493(1982)110¡0808:FINHMH¿2.0.CO;2.

Cheng, Y.-M., C. D. Thorncroft, and G. N. Kiladis, 2019: Two contrasting african easterly wave behaviors. *Journal of the Atmospheric Sciences*, **76**, 1753 – 1768, doi:https://doi.org/10.1175/JAS-D-18-0300.1.

Chikira, M., 2014: Eastward-propagating intraseasonal oscillation represented by chikira–sugiyama cumulus parameterization. part ii: Understanding moisture variation under weak temperature gradient balance. *Journal of the Atmospheric Sciences*, **71**, 615 – 639, doi:10.1175/JAS-D-13-038.1.

Clark, S. K., Y. Ming, and Ángel F. Adames, 2020: Monsoon low pressure system–like variability in an idealized moist model. *Journal of Climate*, **33**, 2051 – 2074, doi:10.1175/JCLI-D-19-0289.1.

Copin, Y., 2021: Taylor diagram for python/matplotlib.
URL `https://doi.org/10.5281/zenodo.5548061`

Daloz, A. S., F. Chauvin, K. Walsh, S. Lavender, D. Abbs, and F. Roux, 2012: The ability of general circulation models to simulate tropical cyclones and their precursors over the north atlantic main development region. *Climate Dynamics*, **39**, 2666–2684, doi:https://doi.org/10.1007/s00382-012-1290-7.

Diaz, M. and W. R. Boos, 2019: Monsoon depression amplification by moist barotropic instability in a vertically sheared environment. *Quarterly Journal of the Royal Meteorological Society*, **145**, 2666–2684, doi:https://doi.org/10.1002/qj.3585.

— 2021a: Evolution of idealized vortices in monsoon-like shears: Application to monsoon depressions. *Journal of the Atmospheric Sciences*, **78**, 1207 – 1225, doi:10.1175/JAS-D-20-0286.1.

— 2021b: The influence of surface heat fluxes on the growth of idealized monsoon depressions. *Journal of the Atmospheric Sciences*, **78**, 2013 – 2027, doi:10.1175/JAS-D-20-0359.1.

Dominguez, C., J. M. Done, and C. L. Bruyère, 2020: Easterly wave contributions to seasonal rainfall over the tropical americas in observations and a regional climate model. *Climate Dynamics*, **54**, 191 – 209, doi:https://doi.org/10.1007/s00382-019-04996-7.

Duchon, C. E., 1979: Lanczos filtering in one and two dimensions. *Journal of Applied Meteorology and Climatology*, **18**, 1016 – 1022, doi:https://doi.org/10.1175/1520-0450(1979)018¡1016:LFIOAT¿2.0.CO;2.

Dunn, G. E., 1940: Cyclogenesis in the tropical atlantic. *Bulletin of the American Meteorological Society*, **21**, 215 – 229, doi:10.1175/1520-0477-21.6.215.

Duvel, J. P., 1990: Convection over tropical africa and the atlantic ocean during northern summer. part ii: Modulation by easterly waves. *Monthly Weather Review*, **118**, 1855 – 1868, doi:10.1175/1520-0493(1990)118¡1855:COTAAT¿2.0.CO;2.

Erickson, C. O., 1963: An incipient hurricane near the west african coast. *Monthly Weather Review*, **91**, 61 – 68, doi:10.1175/1520-0493(1963)091¡0061:AIHNTW¿2.3.CO;2.

Eyring, V., S. Bony, G. A. Meehl, C. A. Senior, B. Stevens, R. J. Stouffer, and K. E. Taylor, 2016: Overview of the coupled model intercomparison project phase 6 (cmip6) experimental design and organization. *Geosci. Model Dev.*, **9**, 1937–1958, doi:https://doi.org/10.5194/gmd-9-1937-2016.

Fahrin, F., A. O. Gonzalez, B. Chrisler, and J. P. Stachnik, 2024: The relationship between convectively coupled waves and the east pacific itcz. *Journal of Climate*, **37**, 2565 – 2583, doi:10.1175/JCLI-D-23-0398.1.

Feng, T., X.-Q. Yang, J.-Y. Yu, and R. Huang, 2020: Convective coupling in tropical-depression-type waves. part i: Rainfall characteristics and moisture structure. *Journal of the Atmospheric Sciences*, **77**, 3407 – 3422, doi:10.1175/JAS-D-19-0172.1.

Fink, A. H. and A. Reiner, 2003: Spatiotemporal variability of the relation between african easterly waves and west african squall lines in 1998 and 1999. *Journal of Geophysical Research: Atmospheres*, **108**, doi:https://doi.org/10.1029/2002JD002816.

Frank, N. L., 1970: Atlantic tropical systems of 1969. *Monthly Weather Review*, **98**, 307 – 314, doi:10.1175/1520-0493(1970)098¡0307:ATSO¿2.3.CO;2.

Fuchs, . and D. J. Raymond, 2002: Large-scale modes of a nonrotating atmosphere with water vapor and cloud–radiation feedbacks. *Journal of the Atmospheric Sciences*, **59**, 1669 – 1679, doi:https://doi.org/10.1175/1520-0469(2002)059¡1669:LSMOAN¿2.0.CO;2.

Hannah, W. M., 2017: Entrainment versus dilution in tropical deep convection. *Journal of the Atmospheric Sciences*, **74**, 3725 – 3747, doi:10.1175/JAS-D-16-0169.1.

Henderson, S. A., E. D. Maloney, and S.-W. Son, 2017: Madden–julian oscillation pacific teleconnections: The impact of the basic state and mjo representation in general circulation models. *Journal of Climate*, **30**, 4567 – 4587, doi:10.1175/JCLI-D-16-0789.1.

Hersbach, H., B. Bell, P. Berrisford, S. Hirahara, A. Horányi, J. Muñoz-Sabater, J. Nicolas, C. Peubey, R. Radu, D. Schepers, A. Simmons, C. Soci, S. Abdalla, X. Abellan, G. Balsamo, P. Bechtold, G. Biavati, J. Bidlot, M. Bonavita, G. De Chiara, P. Dahlgren, D. Dee, M. Diamantakis, R. Dragani, J. Flemming, R. Forbes, M. Fuentes, A. Geer, L. Haimberger, S. Healy, R. J. Hogan, E. Hólm, M. Janisková, S. Keeley, P. Laloyaux, P. Lopez, C. Lupu, G. Radnoti, P. de Rosnay, I. Rozum, F. Vamborg, S. Villaume, and J.-N. Thépaut, 2020: The era5 global reanalysis. *Quarterly Journal of the Royal Meteorological Society*, **146**, 1999–2049, doi:https://doi.org/10.1002/qj.3803.

Holloway, C. E. and J. D. Neelin, 2009: Moisture vertical structure, column water vapor, and tropical deep convection. *Journal of the Atmospheric Sciences*, **66**, 1665 – 1683, doi:https://doi.org/10.1175/2008JAS2806.1.

Hsieh, J.-S. and K. H. Cook, 2008: On the instability of the african easterly jet and the generation of african waves: Reversals of the potential vorticity gradient. *Journal of the Atmospheric Sciences*, **65**, 2130 – 2151, doi:10.1175/2007JAS2552.1.

Huaman, L., E. D. Maloney, C. Schumacher, and G. N. Kiladis, 2021: Easterly waves in the east pacific during the otrec 2019 field campaign. *Journal of the Atmospheric Sciences*, **78**, 4071 – 4088, doi:10.1175/JAS-D-21-0128.1.

Huffman, G. J., D. T. Bolvin, E. J. Nelkin, D. B. Wolff, R. F. Adler, G. Gu, Y. Hong, K. P. Bowman, and E. F. Stocker, 2007: The trmm multisatellite precipitation analysis (tmpa): Quasi-global, multiyear, combined-sensor precipitation estimates at fine scales. *Journal of Hydrometeorology*, **8**, 38 – 55, doi:10.1175/JHM560.1.

Inoue, K., Ángel F. Adames, and K. Yasunaga, 2020: Vertical velocity profiles in convectively coupled equatorial waves and mjo: New diagnoses of vertical velocity profiles in the wavenumber–frequency domain. *Journal of the Atmospheric Sciences*, **77**, 2139 – 2162, doi:10.1175/JAS-D-19-0209.1.

Janiga, M. A. and C. D. Thorncroft, 2013: Regional differences in the kinematic and thermodynamic structure of african easterly waves. *Royal Meteorological Society*, **139**, 1598 – 1614, doi:https://doi.org/10.1002/qj.2047.

Jensen, M. P. and A. D. D. Genio, 2006: Factors limiting convective cloud-top height at the arm nauru island climate research facility. *Journal of Climate*, **19**, 2105–2117, doi:https://doi.org/10.1175/JCLI3722.1.

Jiang, X., M. Zhao, E. D. Maloney, and D. E. Waliser, 2016: Convective moisture adjustment time scale as a key factor in regulating model amplitude of the madden-julian oscillation. *Geophysical Research Letters*, **43**, 10,412–10,419, doi:https://doi.org/10.1002/2016GL070898.

Kiladis, G. N., C. D. Thorncroft, and N. M. J. Hall, 2006: Three-dimensional structure and dynamics of african easterly waves. part i: Observations. *Journal of the Atmospheric Sciences*, **63**, 2212–2230, doi:https://doi.org/10.1175/JAS3741.1.

Kiladis, G. N., M. C. Wheeler, P. T. Haertel, K. H. Straub, and P. E. Roundy, 2009: Convectively coupled equatorial waves. *Reviews of Geophysics*, **47**, 1–42, doi:https://doi.org/10.1029/2008RG000266.

Kindle, E. C., 1944: An application of kinematic analysis to tropical weather. Technical report, Air Weather Service Scott AFB, IL.
URL https://apps.dtic.mil/sti/citations/ADA800254

Kiranmayi, L. and E. D. Maloney, 2011: Intraseasonal moist static energy budget in reanalysis data. *Journal of Geophysical Research: Atmospheres*, **116**, doi:https://doi.org/10.1029/2011JD016031.

Kuang, Z., 2008: Modeling the interaction between cumulus convection and linear gravity waves using a limited-domain cloud system–resolving model. *Journal of the Atmospheric Sciences*, **65**, 576 – 591, doi:10.1175/2007JAS2399.1.

Kuo, Y.-H., J. D. Neelin, and C. R. Mechoso, 2017: Tropical convective transition statistics and causality in the water vapor–precipitation relation. *Journal of the Atmospheric Sciences*, **74**, 915 – 931, doi:10.1175/JAS-D-16-0182.1.

Landsea, C. W., G. D. Bell, W. M. Gray, and S. B. Goldenberg, 1998: The extremely active 1995 atlantic hurricane season: Environmental conditions and verification of seasonal forecasts. *Monthly Weather Review*, **126**, 1174 – 1193, doi:10.1175/1520-0493(1998)126¡1174:TEAAHS¿2.0.CO;2.

Lau, K.-H. and N.-C. Lau, 1990: Observed structure and propagation characteristics of tropical summertime synoptic scale disturbances. *Monthly Weather Review*, **118**, 1888 – 1913, doi:https://doi.org/10.1175/1520-0493(1990)118¡1888:OSAPCO¿2.0.CO;2.

— 1992: The energetics and propagation of tropical summertime synoptic-scale disturbances. *Monthly Weather Review*, **120**, 2523 – 2539, doi:https://doi.org/10.1175/1520-0493(1992)120¡2523:TEAPDO¿2.0.CO;2.

Lin, Q.-J., V. C. Mayta, and Á. F. Adames Corraliza, 2024a: Assessment of the madden-julian oscillation in cmip6 models based on moisture mode theory. *Geophysical Research Letters*, **51**, e2023GL106693, doi:https://doi.org/10.1029/2023GL106693.

— 2024b: Hadley cell instability as a driver of tropical depression-type waves. *Proceedings of the National Academy of Sciences*, Submitted.

Lucas, C., E. J. Zipser, and M. A. Lemone, 1994: Vertical velocity in oceanic convection off tropical australia. *Journal of Atmospheric Sciences*, **51**, 3183 – 3193, doi:10.1175/1520-0469(1994)051¡3183:VVIOCO¿2.0.CO;2.

Mapes, B. E., 2000: Convective inhibition, subgrid-scale triggering energy, and stratiform instability in a toy tropical wave model. *Journal of the Atmospheric Sciences*, **57**, 1515 – 1535, doi:https://doi.org/10.1175/1520-0469(2000)057¡1515:CISSTE¿2.0.CO;2.

Mapes, B. E. and J. T. Bacmeister, 2012: Diagnosis of tropical biases and the mjo from patterns in the merra analysis tendency fields. *Journal of Climate*, **25**, 6202 – 6214, doi:10.1175/JCLI-D-11-00424.1.

Mapes, B. E., T. T. Warner, and M. Xu, 2003: Diurnal patterns of rainfall in northwestern south america. part iii: Diurnal gravity waves and nocturnal convection offshore. *Monthly Weather Review*, **131**, 830 – 844, doi:https://doi.org/10.1175/1520-0493(2003)131¡0830:DPORIN¿2.0.CO;2.

Mapes, B. E., T. T. Warner, M. Xu, and A. J. Negri, 2003: Diurnal patterns of rainfall in northwestern south america. part i: Observations and context. *Monthly Weather Review*, **131**, 799 – 812, doi:https://doi.org/10.1175/1520-0493(2003)131¡0799:DPORIN¿2.0.CO;2.

Martin, E. R. and C. Thorncroft, 2015: Representation of african easterly waves in cmip5 models. *Journal of Climate*, **28**, 7702 – 7715, doi:https://doi.org/10.1175/JCLI-D-15-0145.1.

Matsuno, T., 1966: Quasi-geostrophic motions in the equatorial area. *Journal of the Meteorological Society of Japan. Ser. II*, **44**, 25 – 43, doi:https://doi.org/10.2151/jmsj1965.44.1$_2$5.

Mayta, V. C. and Á. F. Adames, 2021: Two-day westward-propagating inertio-gravity waves during goamazon. *Journal of the Atmospheric Sciences*, **78**, 3727 – 3743, doi:10.1175/JAS-D-20-0358.1.

— 2023: Moist Thermodynamics of Convectively Coupled Waves over the Western Hemisphere. *Journal of Climate*, **37**, 1–36, doi:10.1175/JCLI-D-22-0435.1.

Mayta, V. C., Á. F. Adames, and F. Ahmed, 2022: Westward-propagating moisture mode over the tropical western hemisphere. *Geophysical Research Letters*, **49**, e2022GL097799, doi:https://doi.org/10.1029/2022GL097799.

Mayta, V. C. and Á. F. Adames Corraliza, 2024: The stirring tropics: The ubiquity of moisture modes and moisture–vortex instability. *Journal of Climate*, **37**, 1981 – 1998, doi:10.1175/JCLI-D-23-0145.1.

Mayta, V. C., Á. F. Adames Corraliza, K. Torres Maldonado, H. Luo, and K. Núñez Ocasio, 2024: Thermodynamic processes governing the evolution of developing and strong non-developing african easterly waves. *Journal of the Atmospheric Sciences*, Submitted.

Mayta, V. C., G. N. Kiladis, J. Dias, P. L. S. Dias, and M. Gehne, 2021: Convectively coupled kelvin waves over tropical south america. *Journal of Climate*, **34**, 6531 – 6547, doi:https://doi.org/10.1175/JCLI-D-20-0662.1.

Myoung, B. and J. W. Nielsen-Gammon, 2010: Sensitivity of monthly convective precipitation to environmental conditions. *Journal of Climate*, **23**, 166 – 188, doi:https://doi.org/10.1175/2009JCLI2792.1.

Neelin, J. D. and J.-Y. Yu, 1994: Modes of tropical variability under convective adjustment and the madden–julian oscillation. part i: Analytical theory. *Journal of Atmospheric Sciences*, **51**, 1876 – 1894, doi:10.1175/1520-0469(1994)051¡1876:MOTVUC¿2.0.CO;2.

North, G., T. Bell, R. Cahalan, and F. Moeng, 1982: Sampling errors in the estimation of empirical orthogonal functions. *Monthly Weather Review*, **110**, 699 – 706, doi:10.1175/1520-0493(1982)110¡0699:SEITEO¿2.0.CO;2.

Núñez Ocasio, K. M. and R. Rios-Berrios, 2023: African easterly wave evolution and tropical cyclogenesis in a pre-helene (2006) hindcast using the model for prediction across scales-atmosphere (mpas-a). *Journal of Advances in Modeling Earth Systems*, **15**, e2022MS003181, doi:https://doi.org/10.1029/2022MS003181.

Pasch, R. J., E. S. Blake, L. A. Avila, J. L. Beven, D. P. Brown, J. L. Franklin, R. D. Knabb, M. M. Mainelli, J. R. Rhome, and S. R. Stewart, 2009: Eastern north pacific hurricane season of 2006. *Monthly Weather Review*, **137**, 3 – 20, doi:10.1175/2008MWR2508.1.

Radon, J., 1917: Über die bestimmung von funktionen durch ihre integralwerte längs gewisser mannigfaltigkeiten. *Akad. Wiss.*, **69**, 262 – 277.

Raymond, D. J., 2000: Thermodynamic control of tropical rainfall. *Quarterly Journal of the Royal Meteorological Society*, **126**, 889 – 898, doi:https://doi.org/10.1002/qj.49712656406.

— 2001: A new model of the madden-julian oscillation. *Journal of the Atmospheric Sciences*, **58**, 2807 – 2819, doi:https://doi.org/10.1175/1520-0469(2001)058¡2807:ANMOTM¿2.0.CO;2.

Raymond, D. J., C. S. Bretherton, and J. Molinari, 2006: Dynamics of the intertropical convergence zone of the east pacific. *Journal of the Atmospheric Sciences*, **63**, 582 – 597, doi:10.1175/JAS3642.1.

Raymond, D. J. and Ž. Fuchs, 2009: Moisture modes and the madden–julian oscillation. *Journal of Climate*, **22**, 3031 – 3046, doi:https://doi.org/10.1175/2008JCLI2739.1.

Redelsperger, J.-L., D. B. Parsons, and F. Guichard, 2002: Recovery processes and factors limiting cloud-top height following the arrival of a dry intrusion observed during toga coare. *Journal of the Atmospheric Sciences*, **59**, 2438 – 2457, doi:https://doi.org/10.1175/1520-0469(2002)059¡2438:RPAFLC¿2.0.CO;2.

Reed, R. J., D. C. Norquist, and E. E. Recker, 1977: The structure and properties of african wave disturbances as observed during phase iii of gate. *Monthly Weather Review*, **105**, 317 – 333, doi:10.1175/1520-0493(1977)105¡0317:TSAPOA¿2.0.CO;2.

Reed, R. J. and E. E. Recker, 1971: Structure and properties of synoptic-scale wave disturbances in the equatorial western pacific. *Journal of Atmospheric Sciences*, **28**, 1117 – 1133, doi:10.1175/1520-0469(1971)028¡1117:SAPOSS¿2.0.CO;2.

Ren, P., D. Kim, M.-S. Ahn, D. Kang, and H.-L. Ren, 2021: Intercomparison of mjo column moist static energy and water vapor budget among six modern reanalysis products. *Journal of Climate*, **34**, 2977 – 3001, doi:10.1175/JCLI-D-20-0653.1.

Riehl, H., 1945: *Waves in the easterlies and the polar front in the tropics*. University of Chicago Press, 79 pp.

— 1948: On the formation of typhoons. *Journal of Atmospheric Sciences*, **5**, 247 – 265, doi:10.1175/1520-0469(1948)005¡0247:OTFOT¿2.0.CO;2.

— 1954: *Tropical Meteorology*. McGraw Hill Book Company, 392 pp.

Rushley, S. S., M. A. Janiga, J. A. Ridout, and C. A. Reynolds, 2022: The impact of mean-state moisture biases on mjo skill in the navy espc. *Monthly Weather Review*, **150**, 1725 – 1745, doi:10.1175/MWR-D-21-0225.1.

Russell, J. O. and A. Aiyyer, 2020: The potential vorticity structure and dynamics of african easterly waves. *Journal of the Atmospheric Sciences*, **77**, 871–890.

Russell, J. O., A. Aiyyer, and J. Dylan White, 2020: African easterly wave dynamics in convection-permitting simulations: Rotational stratiform instability as a conceptual model. *Journal of Advances in Modeling Earth Systems*, **12**, e2019MS001706.

Ruti, P. M. and A. Dell' Aquila, 2010: The twentieth century african easterly waves in reanalysis systems and ipcc simulations, from intra-seasonal to inter-annual variability. *Climate Dynamics*, **35**, 1099–1117, doi:https://doi.org/10.1007/s00382-010-0894-z.

Rydbeck, A. V. and E. D. Maloney, 2014: Energetics of east pacific easterly waves during intraseasonal events. *Journal of Climate*, **27**, 7603 – 7621, doi:10.1175/JCLI-D-14-00211.1.

— 2015: On the convective coupling and moisture organization of east pacific easterly waves. *Journal of the Atmospheric Sciences*, **72**, 3850 – 3870, doi:https://doi.org/10.1175/JAS-D-15-0056.1.

Rydbeck, A. V., E. D. Maloney, and G. J. Alaka, 2017: In situ initiation of east pacific easterly waves in a regional model. *Journal of the Atmospheric Sciences*, **74**, 333 – 351, doi:10.1175/JAS-D-16-0124.1.

Sakaeda, N., G. Kiladis, and J. Dias, 2020: The diurnal cycle of rainfall and the convectively coupled equatorial waves over the maritime continent. *Journal of Climate*, **33**, 3307 – 3331, doi:10.1175/JCLI-D-19-0043.1.

Serra, Y. L., G. N. Kiladis, and M. F. Cronin, 2008: Horizontal and vertical structure of easterly waves in the pacific itcz. *Journal of the Atmospheric Sciences*, **65**, 1266 – 1284, doi:https://doi.org/10.1175/2007JAS2341.1.

Serra, Y. L., G. N. Kiladis, and K. I. Hodges, 2010: Tracking and mean structure of easterly waves over the intra-americas sea. *Journal of Climate*, **23**, 4823 – 4840, doi:https://doi.org/10.1175/2010JCLI3223.1.

Sherwood, S. C., 1999: Convective precursors and predictability in the tropical western pacific. *Monthly Weather Review*, **127**, 2977 – 2991, doi:https://doi.org/10.1175/1520-0493(1999)127¡2977:CPAPIT¿2.0.CO;2.

Sherwood, S. C., P. Minnis, and M. McGill, 2004: Deep convective cloud-top heights and their thermodynamic control during crystal-face. *Journal of Geophysical Research: Atmospheres*, **109**, D20119, doi:https://doi.org/10.1029/2004JD004811.

Skinner, C. B. and N. S. Diffenbaugh, 2013: The contribution of african easterly waves to monsoon precipitation in the cmip3 ensemble. *Journal of Geophysical Research: Atmospheres*, **118**, 3590–3609, doi:https://doi.org/10.1002/jgrd.50363.

— 2014: Projected changes in african easterly wave intensity and track in response to greenhouse forcing. *Proceedings of the National Academy of Sciences*, **111**, 6882–6887, doi:10.1073/pnas.1319597111.

Sobel, A. and E. Maloney, 2013: Moisture modes and the eastward propagation of the mjo. *Journal of the Atmospheric Sciences*, **70**, 187 – 192, doi:https://doi.org/10.1175/JAS-D-12-0189.1.

Sobel, A. H., J. Nilsson, and L. M. Polvani, 2001: The weak temperature gradient approximation and balanced tropical moisture waves. *Journal of the Atmospheric Sciences*, **58**, 3650 – 3665, doi:https://doi.org/10.1175/1520-0469(2001)058¡3650:TWTGAA¿2.0.CO;2.

Taylor, K. E., 2001: Summarizing multiple aspects of model performance in a single diagram. *Journal of Geophysical Research: Atmospheres*, **106**, 7183–7192, doi:https://doi.org/10.1029/2000JD900719.

Thompson, R. M., S. W. Payne, E. E. Recker, and R. J. Reed, 1979: Structure and properties of synoptic-scale wave disturbances in the intertropical convergence zone of the eastern atlantic. *Journal of Atmospheric Sciences*, **36**, 53 – 72, doi:10.1175/1520-0469(1979)036¡0053:SAPOSS¿2.0.CO;2.

Thorncroft, C. and K. Hodges, 2001: African easterly wave variability and its relationship to atlantic tropical cyclone activity. *Journal of Climate*, **14**, 1166 – 1179, doi:10.1175/1520-0442(2001)014¡1166:AEWVAI¿2.0.CO;2.

Thorncroft, C. D., N. M. J. Hall, and G. N. Kiladis, 2008: Three-dimensional structure and dynamics of african easterly waves. part iii: Genesis. *Journal of the Atmospheric Sciences*, **65**, 3596 – 3607, doi:https://doi.org/10.1175/2008JAS2575.1.

Thorncroft, C. D. and B. J. Hoskins, 1994a: An idealized study of african easterly waves. i: A linear view. *Quarterly Journal of the Royal Meteorological Society*, **120**, 953–982, doi:https://doi.org/10.1002/qj.49712051809.

— 1994b: An idealized study of african easterly waves. ii: A nonlinear view. *Quarterly Journal of the Royal Meteorological Society*, **120**, 983–1015, doi:https://doi.org/10.1002/qj.49712051810.

Torres, V. M. and C. D. Thorncroft, 2022: Analysis of the environment that supports easterly waves over the eastern pacific and the intra-americas sea in the boreal summer—a potential vorticity perspective. *Journal of Climate*, **35**, 3961 – 3977, doi:10.1175/JCLI-D-21-0482.1.

Torres, V. M., C. D. Thorncroft, and N. M. J. Hall, 2021: Genesis of easterly waves over the tropical eastern pacific and the intra-americas sea. *Journal of the Atmospheric Sciences*, **78**, 3263 – 3279, doi:https://doi.org/10.1175/JAS-D-20-0389.1.

Tory, K., H. Ye, and G. Brunet, 2020: Tropical cyclone formation regions in cmip5 models: a global performance assessment and projected changes. *Climate Dynamics*, **55**, 3213–3237, doi:https://doi.org/10.1007/s00382-020-05440-x.

Vargas Martes, R. M., Á. F. Adames Corraliza, and V. C. Mayta, 2023: The role of water vapor and temperature in the thermodynamics of tropical northeast pacific and african easterly waves. *Journal of the Atmospheric Sciences*, **80**, 2305 – 2322, doi:https://doi.org/10.1175/JAS-D-22-0177.1.

Vargas Martes, R. M., Á. F. Adames Corraliza, V. C. Mayta, and Q.-J. Lin, 2024: East pacific easterly wave representation in cmip6 models. doi:10.22541/essoar.173046728.84436944/v1.
URL `http://dx.doi.org/10.22541/essoar.173046728.84436944/v1`

Waite, M. L. and B. Khouider, 2010: The deepening of tropical convection by congestus preconditioning. *Journal of the Atmospheric Sciences*, **67**, 2601 – 2615, doi:https://doi.org/10.1175/2010JAS3357.1.

Waliser, D. and coauthors, 2009: Mjo simulation diagnostics. *Journal of Climate*, **22**, 3006 – 3030, doi:https://doi.org/10.1175/2008JCLI2731.1.

Warner, T. T., B. E. Mapes, and M. Xu, 2003: Diurnal patterns of rainfall in northwestern south america. part ii: Model simulations. *Monthly Weather Review*, **131**, 813 – 829, doi:https://doi.org/10.1175/1520-0493(2003)131¡0813:DPORIN¿2.0.CO;2.

Whitaker, J. W. and E. D. Maloney, 2020: Genesis of an east pacific easterly wave from a panama bight mcs: A case study analysis from june 2012. *Journal of the Atmospheric Sciences*, **77**, 3567 – 3584, doi:https://doi.org/10.1175/JAS-D-20-0032.1.

Wolding, B., J. Dias, G. Kiladis, E. Maloney, and M. Branson, 2020: Interactions between moisture and tropical convection. part ii: The convective coupling of equatorial waves. *Journal of the Atmospheric Sciences*, **77**, 1801 – 1819, doi:https://doi.org/10.1175/JAS-D-19-0226.1.

Wolding, B., S. W. Powell, F. Ahmed, J. Dias, M. Gehne, G. Kiladis, and J. D. Neelin, 2022: Tropical thermodynamic-convection coupling in observations and reanalyses. *Journal of the Atmospheric Sciences*, doi:10.1175/JAS-D-21-0256.1.

Yu, J.-Y. and J. D. Neelin, 1994: Modes of tropical variability under convective adjustment and the madden–julian oscillation. part ii: Numerical results. *Journal of Atmospheric Sciences*, **51**, 1895 – 1914, doi:10.1175/1520-0469(1994)051¡1895:MOTVUC¿2.0.CO;2.